THESIS

SEISMIC COLLAPSE RISK ASSESSMENT AND PROBABILISTIC SENSITIVITY ANALYSIS OF BRACED FRAMES UNDER NEAR-FAULT EARTHQUAKES

Submitted by

Jeet Kumar Sonwani

Department of Civil and Environmental Engineering

In partial fulfilment of the requirements

For the Degree of Master of Science

Colorado State University

Fort Collins, Colorado

Spring 2019

Master's Committee:

Advisor: Gaofeng Jia
Co-Advisor: Hussam Mahmoud

Erin Arneson

ABSTRACT

SEISMIC COLLAPSE RISK ASSESSMENT AND PROBABILISTIC SENSITIVITY ANALYSIS OF BRACED FRAMES UNDER NEAR-FAULT EARTHQUAKES

Special concentrically braced frames (SCBFs) are popular structural systems used in regions with high seismicity. For SCBFs located in regions close to earthquake faults, they may be subject to near-fault ground motions, often characterized by forward directivity pulse with long periods. These near-fault pulses could impose additional seismic demands on structures and increase the risk for structural collapse. Currently, there is limited research on the seismic collapse risk of SCBFs under near-fault earthquakes. To accurately assess the seismic collapse risk of structures under near-fault ground motions, the seismic hazards and the near-fault characteristics and the associated uncertainties need to be properly quantified. To this end, this research investigates the seismic collapse risk of SCBFs under near-fault earthquakes focusing on two typical SCBFs (i.e., SCBF with Chevron bracing and SCBF with Cross bracing). To assess the seismic collapse risk, a general simulation-based risk assessment framework is used. To quantify the large variability and uncertainty associated with the seismic hazard, stochastic ground motion (SGM) model is used where the near-fault pulse characteristics are explicitly incorporated. The uncertainties in the SGM model parameters (including the near-fault pulse characteristics) are addressed through appropriate selection of probability distribution functions (PDFs). To accurately predict the occurrence of collapse, numerical models capable of capturing the nonlinear and collapse behavior are established for the two braced frames and used in nonlinear time history analysis subject to the stochastic ground motion excitations. Stochastic

simulation is used to propagate the uncertainties and evaluate the resulting multidimensional risk integral. Probabilistic sensitivity analysis is carried out to investigate the importance of each (or groups of) uncertain model parameters within the SGM including the near-fault pulse characteristics towards the seismic collapse risk of the two braced frames. The results indicate that near-fault ground motions could lead to significant increase in the seismic collapse risk of SCBFs and need to be properly considered when designing such structures.

ACKNOWLEDGEMENTS

I would like to express my gratitude for my advisor Dr. Gaofeng Jia who has been an excellent mentor during my thesis. He has always been extremely patient and humble towards me during the whole thesis experience; his technical guidance has helped me in consistently making progress in finishing my thesis. I personally learned some of the most valuable lessons under him which have not only helped me with my research work but also helped me in reshaping who I am as a human being now. I consider myself extremely fortunate to work under him for my research.

Furthermore, I would also like to thank Dr. Hussam Mahmoud whose teaching ignited a spark in me to pursue research; his honest feedbacks really helped me to stay on the right path. At last I would like to thank my committee member Erin Arneson for helping me out in reviewing my work and providing some great insights that have assisted me in accomplishing my research.

I would also like to acknowledge the help that I have received from my lab mates Mr. Zhenqiang Wang and Ms. Min Li, who helped me understand and resolve some of the computational concepts. I greatly appreciate their constant help during my research.

Finally I would like to thank my parents, my brother and my friends whose constant support, love and encouragement helped me in achieving something that I could not have imagined. Thank you for believing in me.

TABLE OF CONTENTS

LIST OF TABLES

LIST OF FIGURES

CHAPTER 1:INTRODUCTION

1.1 Motivation

One of the most crucial objectives of the building codes is the protection of structures against collapse under seismic events. With the advancement in earthquake engineering, the concept of performance-based earthquake engineering (PBEE) is gaining popularity, which considers the entire range of seismic hazards and structural behaviors, including nonlinear behavior and even collapse. For structures located in regions close to earthquake fault lines, they may be subject to near-fault earthquakes. Near-fault ground motions, often characterized by forward directivity pulse with long periods, can impose additional seismic demands on structures, which could increase the likelihood for unpredictable damages and even collapse.

Currently, there is limited research on the seismic collapse risk of structures under near-fault earthquakes. To assess the seismic collapse performance of structures, usually incremental dynamic analysis (IDA) is used. IDA carries out non-linear time history analysis of the structure under a set of selected recorded ground motions, and these ground motions are scaled up until the structure reaches collapse. Typically, ground motions with near-fault pulse are not explicitly considered due to the scarcity in recorded near-fault ground motions. Also, there is concern on the validity of scaled ground motions, which may not represent actual ground motions (e.g., in terms of frequency contents and other characteristics). To accurately assess the seismic collapse risk of structures under near-fault ground motions, the seismic hazards and the near-fault characteristics and the associated uncertainties need to be properly quantified. These challenges hinder better understanding of seismic collapse performance and risk of structures close to

earthquake faults. A better understanding of such risk can guide continued improvement of the building codes and design philosophies. This is what motivates the research in this thesis.

1.2 Scope of the Research

Special concentrically braced frames (SCBFs) are popular structural systems used in regions with high seismicity. It is critical to understand their collapse performance under near-fault earthquakes. This research investigates the seismic collapse risk of SCBFs under near-fault earthquakes. Two typical SCBFs will be considered, i.e., SCBF with Chevron bracing and SCBF with cross bracing. To assess the seismic collapse risk, a general simulation-based risk assessment framework is used, which facilitates the adoption of complex models that include various sources of uncertainty associated with the structure and the seismic hazards. To quantify the large variability and uncertainty associated with the seismic hazard, stochastic ground motion (SGM) model is used to generate synthetic ground motions. The near-fault pulse characteristics are explicitly incorporated in the SGM model. The uncertainties in the SGM model parameters (including the near-fault pulse characteristics) are addressed through appropriate selection of probability distribution functions (PDFs). To accurately predict the occurrence of collapse, numerical models capable of capturing the nonlinear and collapse behavior are established for the two braced frames and used in nonlinear time history analysis subject to the stochastic ground motion excitations. Stochastic simulation is used to propagate the uncertainties and evaluate the resulting multidimensional risk integral. Probabilistic sensitivity analysis is carried out to investigate the importance of each (or groups of) uncertain model parameters within the SGM including the near-fault pulse characteristics towards the seismic collapse risk of the two braced frames.

1.3 Organization of the Research

This thesis is divided into seven different chapters.

Chapter 1 gives a brief introduction to the investigated problem and the motivation of pursuing this research and presents the scope of this research.

Chapter 2 focuses on literature review and background of the proposed research related to performance-based design, characteristics of SCBFs, near-fault earthquakes, and existing research on seismic collapse risk assessment.

Chapter 3 discusses the simulation-based framework for seismic collapse risk quantification and assessment, and the sample-based approach for probabilistic sensitivity analysis to identify important risk factors.

Chapter 4 provides details on the preliminary design and numerical modelling of the braced frames with chevron and cross bracing.

Chapter 5 presents the adopted stochastic ground motion model and provides the complete steps to simulate near-fault ground motions.

Chapter 6 presents the implementation details, case studies and results for seismic collapse risk assessment and probabilistic sensitivity analysis of braced frames under near-fault earthquakes.

And last but not least Chapter 7 summarizes the research findings with recommendations on future research.

CHAPTER 2: LITERATURE REVIEW AND BACKGROUND

2.1 Performance-based Design

Performance-based design is the procedure that enable the design and construction of buildings such that it will be able to attain desired seismic performance such as potential life-safety impacts, potential loss of occupancy and potential repair costs which is in contrast to traditional prescribed building codes [1] It focuses on obtaining structures that perform better than traditional building codes conforming buildings. The rudimentary steps involved in the process are first a performance objective is selected and then a preliminary design is carried out for the structure. After that, assessment of the performance is checked, and if it matches the desired objective performance, then it is acceptable, otherwise it is designed again until the required performance is attained [2]. Figure 1 provides an illustration of the whole system performance under various design level earthquake. It includes the base shear against different damage level where every seismic event has an associative level of damage to the system. It also showcases the acceptable and unacceptable performance of the system. The performance level of a structure is usually selected based on the importance of the structure. Defining the performance parameter is twofold, first there is a specification of desired earthquake level typically taken as 10% probability of exceedance in 50 years or 2% probability of exceedance in 50 years, and the next part is the desired performance level of the structure that should meet or exceed the performance under the chosen seismic hazard. Standard performance levels put forward by American Technical Councils [3,4] and Federal Emergency Management Agency [5,6] include Operational, Immediate Occupancy, Life Safety, and Collapse Prevention.

Figure 1. Performance-based Design

Operational building performance level is the performance level where components of the structure (including both structural and non-structural components) are expected to undergo minimal or no damage. The full functionality of the structure can be achieved by some slight repairing of the non-structural components after immediate ground shaking. Under rare circumstances the buildings are designed to achieve this performance level. Immediate occupancy performance level is the performance level when the structural components go through minimal damage while the non-structural components have negligible damage. This is the most desirable performance level for buildings; this level is a more practical level of performance to achieve than the previous one.

The primary objective of the seismic provisions is to protect life safety through collapse prevention. Most structures are designed to attain this level of performance against future

excitation, and modern seismic codes are built around this criterion. Life safety performance level is the level where the structure experiences considerable damage to both structural and non-structural components. To regain occupancy, structural repair is required which can be extensive depending on the damages. Collapse prevention performance level is the level where the structure may experience failure of the crucial components and it may impose threat to the occupants in the building. This can also lead to significant economic losses [2,7].

2.2 Braced Frames

In regions with high seismicity, special moment resisting frames (SMRF) were considered to be one of the best lateral resisting systems for buildings. However, earthquake events such as the 1994 Northridge earthquake, 1995 Hyogo-Ken Nanbu earthquake and other recent earthquakes, led to the brittle fractures in the beam and column connections, compromising the integrity of such systems. The unpredicted damages in the connections during these earthquake events raised big concern among structural engineers who anticipated that steel beam and column connections were strong enough to endure high seismic ground motions. After these events, FEMA initiated a six-year program led by SAC Joint Venture which consists of Structural Engineers of Northern California, Applied Technology Council, and California Universities for Research in Earthquake Engineering to investigate the problems and develop guidelines which can be beneficial for SMRF systems. The resulting guidelines introduced more rigorous design protocols with even greater emphasis on quality control to achieve target ductility in the connections. Since the design of these systems are governed by the AISC story drift limits, larger steel sections were utilized to meet those requirements, which resulted in more intricate structural configurations and in turn increased the construction cost of SMRF systems.

This plethora of complexity associated with SMRF resulted in a shift towards adopting a simplistic yet economical lateral resisting systems for the low and mid-rise buildings, and concentrically braced frames (CBFs) are considered to be one of the ideal choice in tackling the above complications and hence became a primary choice for seismic load resisting system [8]

CBFs are one of the most economical lateral load resisting systems for low-rise structures, which utilize truss members connected concentrically at the joint of beam and columns. In addition to providing high stiffness and strength, this system tends to have a low ductility overall and under severe earthquake it becomes challenging to maintain the overall strength of the system. Due to low ductility, the yielding members may experience fatigue and failure under seismic loading. This issue can be resolved by utilizing special class of CBFs called Special Concentrically Braced Frames (SCBFs) where the yielding members are meticulously designed and detailed to achieve higher level of ductility during inelastic deformations [9]. Another advantage of using SCBFs for low-rise buildings is seismic retrofitting, since the components can be effectively retrofitted without causing any detrimental effect on the overall system strength and performance.

In structural design for the braced frames under the seismic loads, it is critical to identify the weak link in the structure, because the earthquake loading is highly nonlinear and due to its high variability, it can impose stresses in the components significantly larger than the design level earthquake, which can led to unexpected failure in the system. Proper design and detailing is required for these components in order to avoid undesirable failure or complete collapse. In braced frames these weak links are ‘braces’. The bracing member are the components that requires proper detailing in order to keep them ductile during yielding and buckling under seismic loading. So in order to accomplish that, all these components are oversized with respect

to the capacity of the brace, which allows them to be protected during non-linear behavior. So the system deforms elastically under seismic action but it will not collapse, the integrity of the structure will remain intact, and it will still carry the gravity loads although it has been subjected to loads larger than its capacity. The behavior of an example braced frame is illustrated in Figure 2 where braces in tension and compression can be clearly seen.

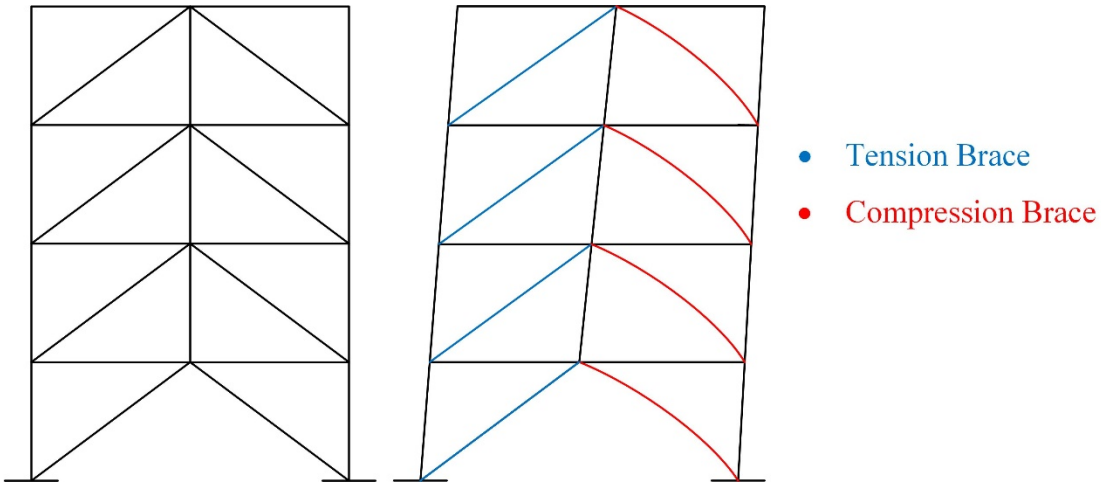

Figure 2 Brace Behavior of Braced Frame

2.2.1 Component Behavior of SCBFs

Early research work done on braced frames has focused mainly on the components such as the braces and the gusset plates under monotonic cyclic loading. The brace is the essential element in SCBFs as it dissipates most of the seismic energy under earthquake loading; if designed properly, then this should be the first member to fracture. So understanding its behavior becomes a priority to maximize performance. Some of the earlier research to understand brace behavior includes.[10–12] The most important takeaway from these studies is the effect of the slenderness ratio (brace slenderness and section slenderness) towards the drift capacity of the

member. The accurate detailing of the braces are essential for achieving ductility; so for brace slenderness, high slenderness ratio leads to severely pinched hysteretic response while low slenderness ratio leads to a reduction in the ductility capacity and ultimately fracture of the component under higher deformations. So the KL/r limit should be more than 70 and less than 200. For the section slenderness of the brace members, high section slenderness leads to localized yielding and premature fracture of the braces. So in order to avoid that b/t and D/t limits needs to be checked as proposed by AISC-05 [13].These experimental studies were beneficial in understanding the behavior of the components, the overall system behavior was not well understood due to lack of accurate boundary conditions.

2.2.2 System Behavior of SCBFs

The study and research done on understanding the overall system behavior of braced frame are much less. Some of the major studies include the experiments carried out at University of California, Berkeley on three one-story, one bay buckling restrained braced frame (BRBFs) and two story, one bay SCBF with buckling HSS braces, which showed that the current design provisions AISC 97 [14] were not performing as intended under cyclic loading. The system suffered brittle beam fracture, which occurred at story drifts expected to see during experiments which were less than story drift limit during severe seismic events [15].

In order to better understand SCBFs system behavior, National Science Foundation (NSF) funded and initiated a research program under Network for Earthquake Engineering Simulation (NEES) called “International Hybrid Simulation of Tomorrows Braced Frame Systems” whose goal was to create a new design procedure to unlock the potential of these systems. The project involved testing 38 braced frames with the emphasis on the gusset plate

connection. This research resulted in improvement to the design and connection detailing which improved the overall performance of the system by further extending the ductility of the SCBFs [16]. Major advancement has been studying the analytical portion of the braced frames by improving the continuum finite element models for the SCBFs and also developing discrete line element models which captures the brace fracture [17]. In addition to this, first 3D SCBF experiment was carried out with realistic boundary conditions to evaluate performance of the system, understand the effects of bi-directional loading on the ductility of the frame, and investigate the effects of gusset plate geometry in the behavior of the system and also an improvement to the balanced design procedure, which is alternative to the capacity design procedure [18]. All the above research and experiments assisted in understanding the complex behavior of the system [18].

2.3 Braced Frame under Near-Fault Earthquakes

2.3.1 Near-Fault Earthquakes

Earthquakes can have significant impacts on structures and can potentially lead structural collapse. If the structure is situated near the fault zone, then its probability to have unexpected failure is increased. Near-fault ground motions are characterized by strong coherent long period pulse and permanent ground displacements, due to which they can be more detrimental to structures than far-field earthquakes. The risk associated with these ground motions on the structures is not adequately comprehended. These ground motions are typically governed by long-period pulses caused by forward rupture directivity effects (large velocity amplitude). After studying the recent earthquakes by seismologists it was observed that the period of pulse is

increased with the earthquake magnitude and this dependence led to increase in the intensity of the forces generated by the ground motion.

There are many characteristics associated with near-fault ground motions. Forward directivity usually happens when the fault rupture propagates to a site, and when the shear wave velocity is close to rupture velocity, large period pulses are originated from the fault. Also from observing various different ground motions that exhibit near fault pulse, the corresponding response spectrum of the fault-normal component was very high when compared with the parallel component. The Fling effect is an aftereffect of the earthquake where the ground experience permanent tectonic deformation for the particular structural site. This is characterized by large amplitude velocity pulse and typically arises in the parallel component of the fault. Near field pulses are typically characterized in terms of their waveforms, which include the pulse duration, amplitude as well as the number and phase of half cycles. In addition to this, the effect of forward directivity decreases as the structure is further away from the fault; the near-fault pulse like ground motion are likely to occur within around 15 km of the fault [19].

Due to the lack of availability of recorded near fault ground motions, the synthetic ground motion for near fault sites can be used in PBEE. It is important to have realistic and consistent ground motions which include pulse characteristics. There are many models developed over the years [20]. Some of the existing models include [21] proposed a method for representing velocity pulse under specific site conditions and the resultant velocity when fitted to the recorded ground motions lack the high frequency content. A hybrid method of stochastic and theoretical green's function can be used to for generating near fault ground motion. This approach considers the complete waveform (far-, intermediate- and near field terms) [22]. This corresponds to a seismological numerical model. A mathematical model [23] of velocity pulse

that can replicate the intermediate to long period features of near fault pulse like ground motion and this model again lack the high frequency content due to which they suggested a stochastic approach based on source model that can describe incoherent high frequency content. This model corresponds to stochastic model based on random process theory which is used in this study.

2.3.2 Braced Frame under Near-Fault Earthquakes

As previously described, near-fault ground motions are characterized by forward directivity pulse and these pulses contain large amount of seismic energy, which imposes higher demands in the structures. This energy needs to be dissipated by the structures, due to which large deformations can occur in the system and the risk for brittle fracture or fatigue of structural components is increased [24]. Pulses generated through ground motion can also lead to highly uneven distribution of the ductility demands in the different story of the building. Experimental results have validated some of the unexpected behaviors of structures when subjected to pulse type ground motions. The results indicated that when the fundamental period of the structure is larger than the period of the pulse, the ductility demands for the roof has already reached towards the maximum ductility limit under low intensity of ground motions. When the ground motion intensity increases, the ductility demand at the bottom of structure will increase rapidly. In addition to this, when the fundamental period of the structure is shorter than pulse period, the maximum story ductility demand originates at the bottom of the structure and it gets intensified with the increase in the ground motion. This indicates that under the pulse type ground motion the standard story shear strength distributions led to huge variations of ductility demands over the height of the structure [25]. The impacts of near-fault earthquakes on braced frames, especially the collapse risk, are still not well understood with limited research.

2.4 Seismic Collapse Risk Assessment

Structural collapse occurs when the load carrying capacity of the structure fails during a seismic event. Collapse can be either vertical or sidesway; and for ductile frame, sidesway collapse is more predominant during earthquakes [26]. There are various quantitative assessment tools to assess the performance of the structure. Over the decades the analysis has shifted from static approach to dynamic approach. Before the introduction of the performance based design, static pushover analysis was used to gather information about the overall behavior of the structure. This analysis estimated the strength, stiffness and its degradations as the deformation in the structure increases. It also included the material non-linearities and the second order effect of the structure. This analysis had some major issues such as no torsional effects, orthogonality effects cannot be integrated, no higher modes effects once local mechanisms was formed, and many more. This led to development of new methods of assessment since accurate prediction was not possible from this analysis. Over time, new methods of analysis were developed which included the non-linear time history analysis where the behavior of the structure is quantified under a specific ground motion and its response is calculated at subsequent time instants. This analysis considers the higher mode effects. Though accurate, this approach is computationally more challenging than the pushover analysis and the results are highly sensitive to the ground motion records used. It is advised by Structural Engineers Association of California to use at least 3 to 7 ground motions to avoid the sensitivity issues. This analysis can be difficult for complex structure.

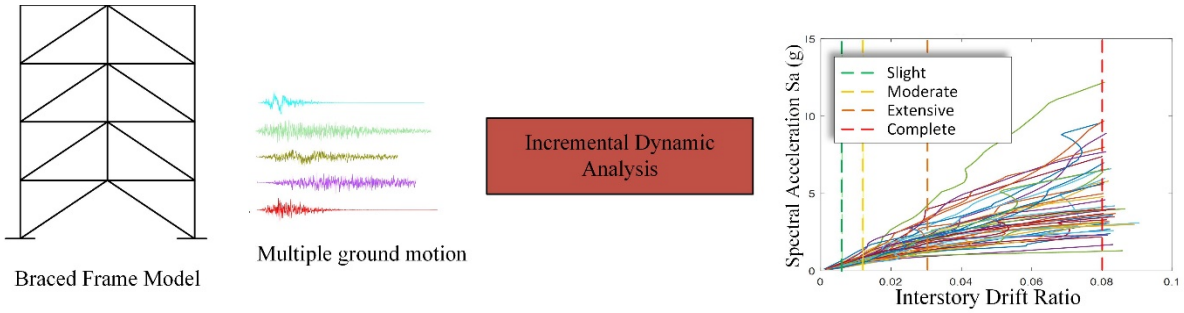

Figure 3 Incremental Dynamic Analysis

To assess the seismic collapse performance of structures, usually incremental dynamic analysis (IDA) is used. It is a computational analysis method for performing a comprehensive assessment of the behavior of structures under seismic loads. It can be considered as the dynamic equivalent of the pushover analysis. This analysis can be used to estimate seismic risk. This method involves selecting an engineering demand parameter and set of ground motions. The procedure includes multiple nonlinear dynamic analysis where the set of ground motion data is selected and each ground motion is scaled to several levels of seismic intensity until the engineering demand parameters (EDPs) go through the entire range of behavior, from elastic to inelastic and finally to global dynamic instability where the structure experiences collapse [27]. Typically, the post processing is represented in terms of scalar intensity measure (IMs). Some of the possible choices for IMs includes peak ground acceleration, peak ground velocity, and 5% damped spectral acceleration is most commonly used while EDPs include the response parameter such as maximum interstory drift, peak floor accelerations and peak story drift. The visual representation of IDA is shown in. Figure 3. It can also be observed from IDA curve (Spectral acceleration vs interstory drift ratio) is plotted where different interstory drift ratio defines the threshold for different damage state and then for each set of earthquake records, the probability of exceedance at each damage state at a particular spectral intensity is calculated. Finally

fragility curves are developed that provides the performance of structure in terms of different damage states [28].

Though helpful in assessing collapse performance, the use of scaled ground motion in IDA raises concerns. More specifically, there is concern on the validity of scaled ground motions, which may not represent actual ground motions (e.g., in terms of frequency contents and other characteristics). In the context of seismic collapse risk assessment under near-fault earthquakes, the variability in the near-fault ground motions may not be properly quantified considering scarcity in recorded near-fault ground motions. Also, how the seismic hazard characteristics and near-fault pulse characteristics impact the seismic collapse risk is still not well understood. Sensitivity analysis that can help identify the key contributing risk factors in the near-fault earthquakes may help achieve this goal.

Overall, to accurately assess the seismic collapse risk of structures under near-fault ground motions, the seismic hazards and the near-fault characteristics and the associated uncertainties need to be properly quantified. These challenges hinder better understanding. A better understanding of seismic collapse performance and risk of structures close to earthquake faults can guide continued improvement of the building codes and design philosophies, which motivates the research in this thesis.

CHAPTER 3: SEISMIC COLLAPSE ASSESSMENT AND SENSITIVITY ANALYSIS

3.1 Simulation-based Framework for Seismic Collapse Risk Quantification

To quantify the seismic collapse risk of braced frames, the simulation-based framework in [29] is used. This framework considers an augmented system model that includes models for the excitation, the system model, and the performance model. The evaluation of the seismic risk requires the combination of these models. It is crucial to properly characterize the uncertainties associated with these models. For our research, the focus will be on the impact of the uncertainties in the ground motion (including near-fault pulse characteristics) and future variabilities related to it [29]. In order to quantify all the uncertainties associated with ground motion and integrate them into the augmented system model, a probability logic approach is adopted where appropriate PDFs are assigned to the uncertain parameters, leading to an efficient seismic risk quantification[30–32].

Let $\boldsymbol{\theta}$ represent all the uncertain model parameters related to the ground motion model where $\boldsymbol{\theta} \in \Theta \subset R^{n_\theta}$ and Θ the entire domain for all the possible values for the uncertain parameters and n_θ the dimension (total number) of uncertain parameters, and $p(\boldsymbol{\theta})$ represent the PDF for the uncertain parameters $\boldsymbol{\theta}$. Now the performance of the system can be characterized as $h(\theta): \mathbb{R}^{n_\theta} \to \mathbb{R}^+$ which is called the performance parameter and can be evaluated based on the structural response. In stochastic setting, the seismic risk H can be described as the expected value of $h(\boldsymbol{\theta})$ over the probability models for $\boldsymbol{\theta}$ in Eq.(3.1).

$$H = E_p[h(\boldsymbol{\theta})] = \int_\Theta h(\boldsymbol{\theta})\, p(\boldsymbol{\theta}) d\boldsymbol{\theta} \tag{3.1}$$

Based on the different definition for performance parameter $h(\boldsymbol{\theta})$, different seismic risk H can be established. In this research, we are interested in the seismic collapse risk or the probability of collapse. In this case, $h(\boldsymbol{\theta})$ corresponds to the indicator function I_F against the failure event F ; and if the structure fails, then its value is 1 otherwise 0, so ultimately H is the failure probability against an event F . So the above equation (3.1) can be modified such that $H \equiv P_F$ and the performance parameter $h(\boldsymbol{\theta}) \equiv I_F(\boldsymbol{\theta})$ in Eq.(3.2). In our study the indicator function I_F is calculated by comparing the maximum interstory drift ratio obtained through structural response and compared with the threshold that defines the acceptable performance. The AISC collapse limit of braced frame is selected where maximum interstory drift is 5%. So when the structure response (interstory drift ratio) is more than the threshold the $I_F = 1$ and hence H corresponds to system's 'failure' and if the structural response is less than threshold then the H corresponds to system's acceptable performance. Figure 4 illustrates the augmented system model for the seismic risk quantification.

$$P_F = \int_{\Theta} I_F(\boldsymbol{\theta})\, p(\boldsymbol{\theta}) d\boldsymbol{\theta} \tag{3.2}$$

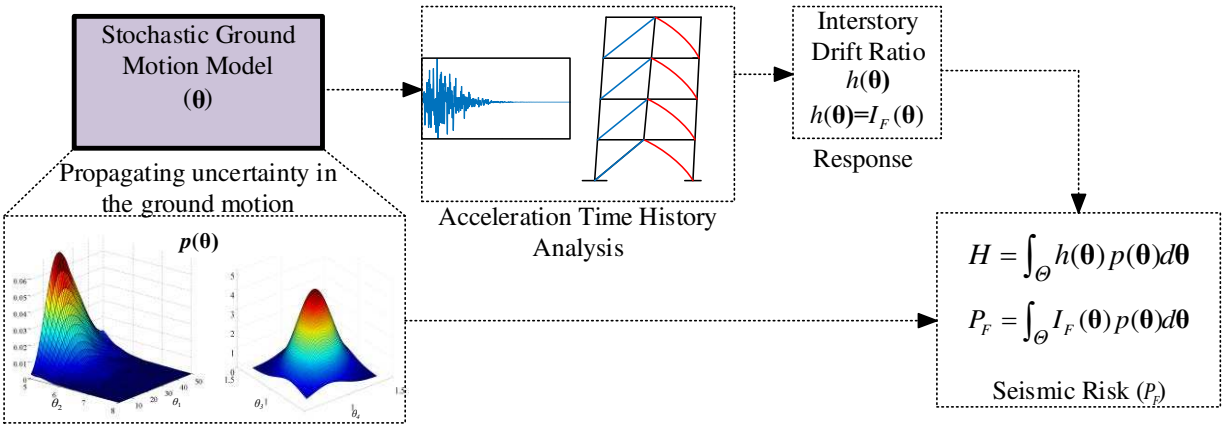

Figure 4 Augmented Model for Seismic Risk Quantification

3.2 Stochastic Simulation for Seismic Collapse Risk Assessment

To evaluate the risk integral, which corresponds to a multidimensional integral over the entire domain Θ, stochastic simulation is used, which is general and can address complex models and high-dimensional uncertainties. More specifically, using N samples from some proposal density $q(\boldsymbol{\theta})$, an approximate estimation of the integral can be achieved by Eq. (3.3) [32].

$$\hat{H} = \frac{1}{N}\sum_{j=1}^{N} h(\boldsymbol{\theta}^j)\frac{p(\boldsymbol{\theta}^j)}{q(\boldsymbol{\theta}^j)} \tag{3.3}$$

where $\boldsymbol{\theta}^j$ represents the sample in the j^{th} simulation. For each $\boldsymbol{\theta}^j$, a corresponding stochastic ground motion can be generated, which will serve as input for the nonlinear time history analysis, and the corresponding structural response and performance $h(\boldsymbol{\theta}^j)$ can be established. So for our study the equation (3.2) can be modified into the equation mentioned below in Eq. (3.4).

$$\hat{P}_F = \frac{1}{N}\sum_{j=1}^{N} I_F(\boldsymbol{\theta}^j)\frac{p(\boldsymbol{\theta}^j)}{q(\boldsymbol{\theta}^j)} \tag{3.4}$$

One of the advantages of the stochastic simulation based approach is the ability to assess the accuracy of the estimation, which can be evaluated through its coefficient of variation δ. Lower values of δ means better accuracy. The mathematical expression for calculating the coefficient of variation can be done using the Eq. (3.5) below [33].

$$\delta \approx \frac{1}{\sqrt{N}} \frac{\sqrt{\frac{1}{N}\sum_{j=1}^{N}\left(I_F(\boldsymbol{\theta}^j)\frac{p(\boldsymbol{\theta}^j)}{q(\boldsymbol{\theta}^j)}\right)^2 - \left(\hat{P}_F\right)^2}}{\hat{P}_F} \tag{3.5}$$

In order to improve the accuracy of the estimation, it is not efficient to simply increase N due to the fact that δ is inversely proportional to $\sqrt{N}$. To efficiently establish estimation with good accuracy, important sampling can be adopted, which corresponds to choosing a better proposal density (i.e., importance sampling density) $q(\boldsymbol{\theta})$ by focusing on the dimensions which can have more impact than the others towards the integrand [32]. When $q(\boldsymbol{\theta}) = p(\boldsymbol{\theta})$, the stochastic simulation corresponds to direct Monte Carlo simulation (MCS).

For the current problem, it is expected that ground motion model parameters such as moment magnitude, rupture distance and amplitude of pulse may have large impacts on the seismic collapse risk, and proposal density will be built with respect to those parameters to improve the estimation accuracy and efficiency.

3.3 Probabilistic Sensitivity Analysis

3.3.1 Relative Entropy

Sensitivity analysis involves the study of how the uncertainty in the output of the numerical model or system can be apportioned to different sources of uncertainty in its inputs. To identify the uncertain model parameters in the ground motion model that have higher

contribution towards the seismic collapse risk of braced frames, we use the probabilistic sensitivity measure called relative entropy proposed in [34]. The foundation of this analysis is the definition of an auxiliary probability density function (PDF) which is proportional to the integrand of the risk integral

$$\pi(\boldsymbol{\theta}) = \frac{h(\boldsymbol{\theta})\,p(\boldsymbol{\theta})}{\int_{\Theta} h(\boldsymbol{\theta})\,p(\boldsymbol{\theta})\,d\boldsymbol{\theta}} = \frac{h(\boldsymbol{\theta})\,p(\boldsymbol{\theta})}{H} \propto h(\boldsymbol{\theta})\,p(\boldsymbol{\theta}) \tag{3.6}$$

where $\propto$ denotes proportionality. The sensitivity analysis can be determined by comparing the auxiliary PDF $\pi(\boldsymbol{\theta})$ with the prior PDF $p(\boldsymbol{\theta})$ based on the definition which provides the information about $h(\boldsymbol{\theta})$ The larger difference between the auxiliary PDF and the prior PDF implies higher the importance of that parameter towards seismic risk [35]. This idea is not limited to a particular single parameter θ_i (or even group $\boldsymbol{\theta} = \{\theta_i, \theta_j, \theta_k\}$) and can be extended towards a set of uncertain parameters by looking at the marginal distribution $\pi(\theta_i)$ [29]

$$\pi(\theta_i) = \int \pi(\boldsymbol{\theta})\,d\boldsymbol{\theta}_{\sim i} = \frac{1}{\int_{\Theta} h(\boldsymbol{\theta})\,p(\boldsymbol{\theta})\,d\boldsymbol{\theta}} \int h(\boldsymbol{\theta})\,p(\boldsymbol{\theta})\,d\boldsymbol{\theta}_{\sim i} \propto p(\theta_i) \int h(\boldsymbol{\theta})\,p(\boldsymbol{\theta}_{\sim i} \mid \theta_i)\,d\boldsymbol{\theta}_{\sim i} \tag{3.7}$$

where $\boldsymbol{\theta}_{\sim i}$ is the rest of the remaining parameters from $\boldsymbol{\theta} = \{\theta_i, \boldsymbol{\theta}_{\sim i}\}$ except θ_i.

To quantify the difference between the two PDFs, relative entropy can be used. For θ_i, the relative entropy can be written as [36,37].

$$D\left(\pi(\theta_i) \,\|\, p(\theta_i)\right) = \int_{\Theta_i} \pi(\theta_i) \ln\left[\frac{\pi(\theta_i)}{p(\theta_i)}\right] d\theta_i \tag{3.8}$$

One of the key challenges in calculating the relative entropy is to evaluate the marginal distribution $\pi(\theta_i)$ for any given value of θ_i. The integration itself can be calculated using

numerical integration when θ_i is a scalar quantity. For groups of parameters, Monte Carlo simulation can be used to evaluate the corresponding relative entropy integral.

3.3.2 Sample-based Estimation of Relative Entropy

To efficiently estimate the relative entropy or more specifically the auxiliary distribution $\pi(\theta_i)$, the sample-based approach in [34] will be used. It relies on generating samples from the joint distribution $\pi(\boldsymbol{\theta})$, then the projection of these samples to spaces representing each uncertain parameter gives samples from the corresponding marginal distribution $\pi(\theta_i)$ [38]. Then based on the marginal samples, an estimate of the marginal PDF can be established using Kernel density estimation (KDE) [39]. KDE is a non-parametric approach in which the estimation of PDF can be done putting kernel over each sample, where σ_{si} defines the standard deviation of the kernel, σ_{li} is the spread of each kernel and n_z is the total number of samples. The sample-based approach is illustrated Figure 5 for an example with two dimensional parameters. The figure shows the samples for $\{\theta_i, i=1,2\}$ and its projection to each dimension as well as the corresponding KDE.

$$\tilde{\pi}(\theta_i) = \frac{1}{n_z \sigma_{li}\sqrt{2\pi}} \sum_{k=1}^{n_z} e^{-\frac{(\theta_i-\theta_i^k)^2}{2\sigma^2_{li}}}, \sigma_{li} = 1.06.n_z^{\frac{-1}{5}}\sigma_{si} \tag{3.9}$$

Similarly, to achieve a better consistency for relative entropy quantification, $p(\theta_i)$ can be also estimated using KDE. In this way the error associated with KDE can be propagated towards both prior distribution $p(\theta_i)$ and the auxiliary distribution $\pi(\theta_i)$. Now the approximation of relative entropy can be established through [38]. In the integral the boundary

corrections can be used for better estimation of PDFs and lb is lower bound and ub is the upper bound [34].

$$D\left(\pi(\theta_i) \,\|\, p(\theta_i)\right) = \int_{-\infty}^{+\infty} \pi(\theta_i) \log\left(\frac{\pi(\theta_i)}{p(\theta_i)}\right) d\theta_i = \int_{-lb}^{+ub} \tilde{\pi}(\theta_i) \log\left(\frac{\tilde{\pi}(\theta_i)}{\tilde{p}(\theta_i)}\right) d\theta_i \tag{3.10}$$

Ultimately this approach leads to an efficient estimation of the relative entropy, which can be performed simultaneously with the seismic risk assessment (e.g., using the same set of simulations and some stochastic sampling algorithm to generate samples from $\pi(\boldsymbol{\theta})$ and hence decreasing the computational burden associated with the methodology. Hence this approach can provide the comparison between the PDFs $p(\theta_i)$ and $\pi(\theta_i)$ eventually defining the contribution of the uncertain model parameter θ_i towards the overall seismic risk [40,41].

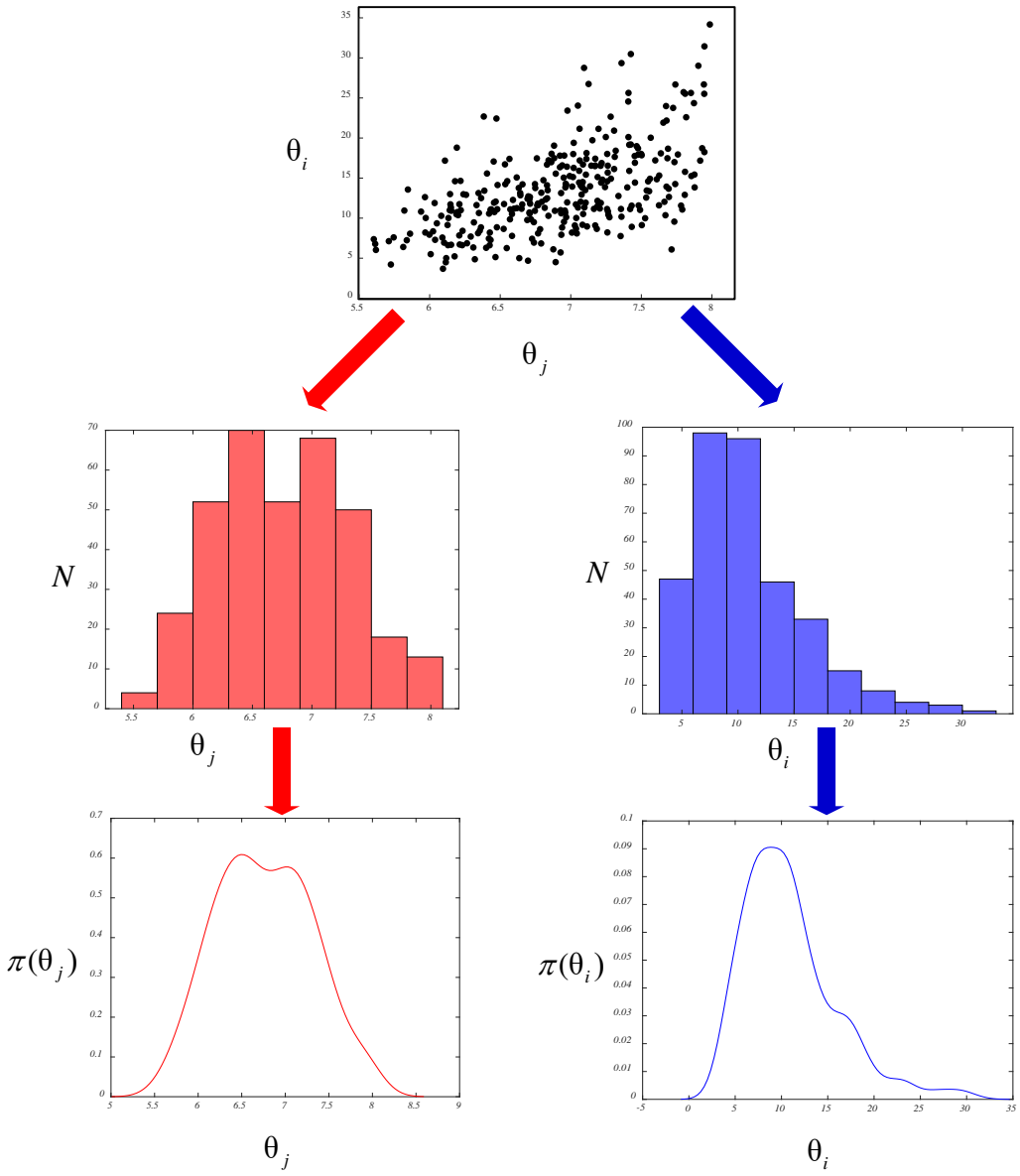

Figure 5 Flow chart for KDE where estimation of individual parameters $\{\boldsymbol{\theta} = \theta_i, \theta_j\}$ from joint PDF $\pi(\boldsymbol{\theta})$

CHAPTER 4: SEISMIC DESIGN AND NUMERICAL MODELLING

4.1 Seismic Design of Braced Frames

4.1.1 Description of the Braced Frames

In this study, to establish the model building, the building from the SAC Joint Venture project, which evaluated the performance of the moment resisting frame under performance-based design, is used. The model building was designed based on local code requirement for three different cities (i.e., Los Angeles (UBC 1994), Seattle (UBC 1994) and Boston (BOCA 1993)) [42]. For this research the 3-story model building is redesigned and modelled as a braced frame Figure 6. Two configurations of the braced frame are considered: the chevron bracing with zipper columns and the cross bracing system [43].

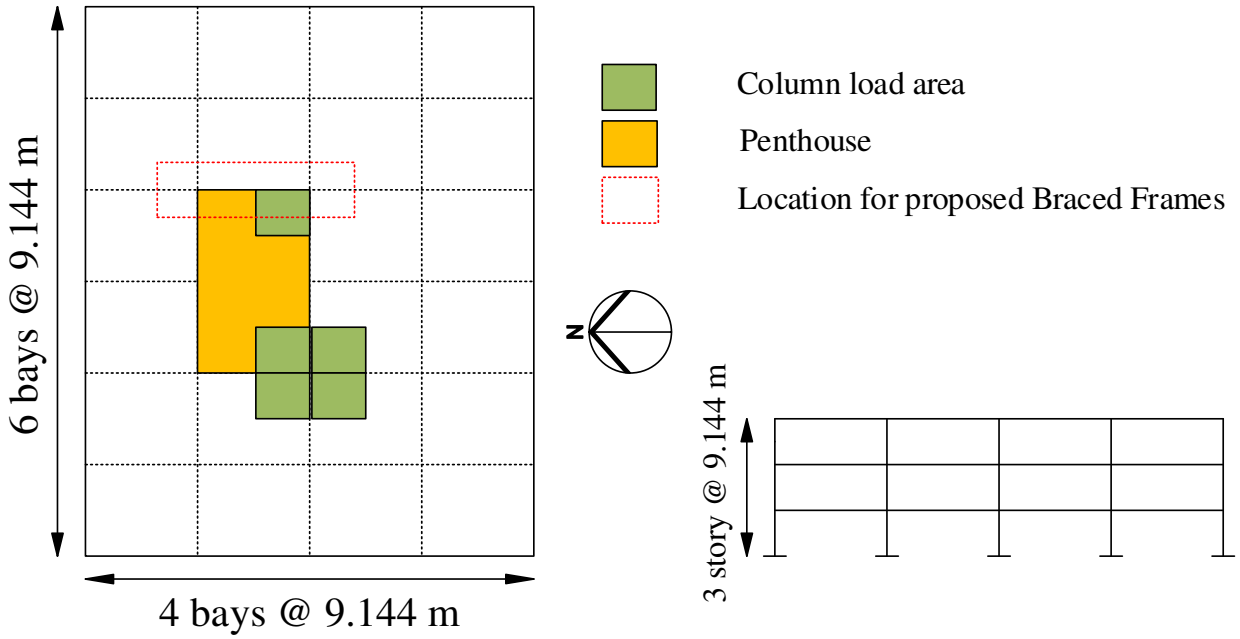

Figure 6 Floor Plan and Elevation from SAC Steel Project

The floor plan and elevation view of the 3-story SAC building are illustrated in Figure 6. The building is to be designed as standard office building. Moment resisting frames are utilized in the periphery of the office building. In this research, the braced frames are designed at perimeter of the penthouse located at the two bays in each direction of the building. The yellow shaded area in the figure indicates the location of the penthouse. This configuration allows the designed lateral load resisting system to be identical. Also, the global torsion is ignored during the design of the braced frames.

4.1.2 Lateral Load Distribution on Structure

All the loads (dead and live load) acting on the different floor and their distribution can be obtained from the report in Appendix B from FEMA 355C [42], which is listed in Table 1. The moment resisting frame was designed based on these loads. The self-weight of the steel here is assumed to be 0.622 kN/m^2 [42].

Table 1 Load distribution on structure

Floor Load Distribution	Load (kN/m^2)
Floor dead load for weight calculations	4.596
Floor dead load for mass calculations	4.117
Roof dead load excluding penthouse	3.974
Penthouse dead load	5.554
Reduced live load per floor and for roof	0.957

The given loading definition is used to estimate the seismic mass of the structure, which is given in Table 2 for all floors.

Table 2 Mass of the structure

Floor	Mass (kN)
Roof	10155.29
Third Floor	9386.19
Second Floor	9386.19

The new FEMA guidelines is used to calculate the lateral load acting on this system. The structure modelled here is assumed to be located in Seattle, and according to USGS Earthquake Hazard Project, the maximum considered earthquake ground motion map 9 and 10 of the provision provides spectral response acceleration at short period $S_s = 1.5g$ and at 1 second period $S_1 = 0.5g$. These values are then changed based on the site class C. The steps mentioned below helps in evaluating the base shear of the structure (earthquake load calculation) The adjusted maximum considered earthquake response acceleration based on the coefficient obtained from the site class C, $F_a = 1.0$ and $F_v = 1.3$ are

$$S_{MS} = F_a S_s = 1.5g \tag{4.1}$$

$$S_{M1} = F_v S_1 = 0.645g \tag{4.2}$$

Then the design spectral response acceleration parameters are calculated as

$$S_{DS} = S_{MS} = 1.0g \tag{4.3}$$

$$S_{D1} = S_{M1} = 0.43g \tag{4.4}$$

The seismic response coefficient is then calculated based on the response modification factor $R = 6$ and the occupancy importance factor $I = 1.5$ (seismic group III),

$$C_s = S_{DS} / R / I = 1.0g / 4 = 0.25g \tag{4.5}$$

The maximum seismic response coefficient is calculated. where $C_t = 0.03$ and $x = 0.75$ and approximate fundamental period of the structure for height of the structure $h_n = 39\,ft$ by ASCE 7 §12.8.2.

$$T_a = C_t h_n^{\,x} = 0.02*(39)^{0.75} = 0.312s \tag{4.6}$$

Now the fundamental period of the structure is determined by

$$T = C_u T_a = 1.4*0.312 = 0.44s \tag{4.7}$$

where $C_u = 1.4$ (coefficient for upper limit of calculated period)

$$C_{s,\,max} = S_{D1}/T(R/I) = 0.43g/0.44\,(6/1.5) = 0.246g \tag{4.8}$$

Similarly for the category E, minimum seismic response coefficient can be obtained by

$$C_{s,\,min} = 0.5S_1/(R/I) = 0.5*0.5g/\,(6/1.5) = 0.0625g \tag{4.9}$$

The C_s value should be in between the maximum and the minimum seismic coefficient which resulted in $C_s = 0.246g$.

The total base shear of the structure is given by

$$V = WC_s = 0.246g*6503 = 7116.25\,kN \tag{4.10}$$

where total seismic mass W of the structure can be calculated from the Table 3

Finally after obtaining the total base shear of the structure, the vertical distribution of the forces in the each story is given by the equation below and the calculated distribution on each floor is represented in the Figure 7 below.

$$F_x = C_{vx}V \tag{4.11}$$

where $C_{vx} = \dfrac{w_x h_x^k}{\sum_{i=1}^{n} w_i h_i^k}$ is the vertical distribution factor with *k*=1.0 (exponent related to the period

of the structure) and w_x is the portion of total gravity load while h_x is the height from base to x level. The Table 3 provides the vertical forces acting at each floor of the structure.

Table 3 Lateral load distribution on the structure on each floor

Floor	h_x(m)	w_x(kN)	$w_x h_x$	C_{vx}	F_x(kN)
Roof	11.88	10155.29	120644.84	0.52	3700.45
Third Floor	7.92	9386.19	74338.62	0.32	2277.20
Second Floor	3.96	9386.19	37169.31	0.16	1138.60
Sum		**28927.67**	**232152.77**	**1.00**	**7116.25**

4.1.3 Gravity Load on the Structure

For the design purpose, the gravity loads acting on the column is evaluated based on the distributed load acting on the structure from the Table 1. Load combination is taken as $1.2D + 1.6L$ where D is the deal load and L is the live load and acting on the structure. Table 4 below lists the gravity load acting on the each column.

Table 4 Loads acting on columns

Floor	Loads on Column (kN)	Total Loads (kN)
Penthouse	171.25	171.25
Roof	526.66	698.37
Third Floor	589.38	9386.19
Second Floor	589.38	1876.70

In addition to this, the maximum bending moment generated in the beams due to gravity loading is calculated as well. The end conditions for the beam we assumed to be pinned which resulted in the maximum moment

$$M_{max} = 1/8 p * l^2 \tag{4.12}$$

Where p is the distributed load per feet and l is the length of the beam. The Table 5 below describes the maximum moments acting on the beam for both 4.57 m and 9.14 m in length [43]. This is calculated to obtain the maximum forces generated on the beams due to gravity load to select the appropriate sections accordingly.

Table 5 Moment load on beams

Floor	UDL p (kN/m)	M_{max} at 4.57m (kN-m)	M_{max} at 9.14m (kN-m)
First floor	64.44	168.12	673.84
Second Floor	64.44	168.12	673.84
Third Floor	57.61	150.49	601.98

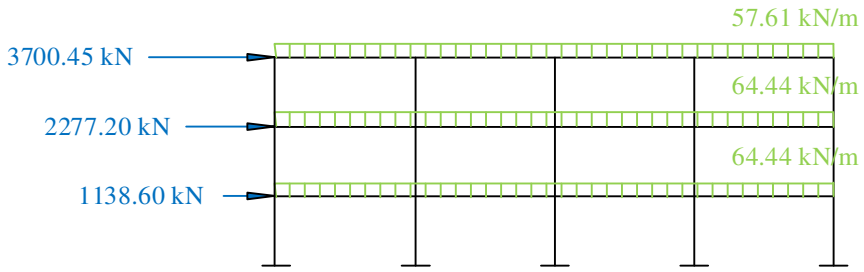

Figure 7 Lateral Load and Gravity Load distribution on each floor of the Structure

4.2 Seismic Load Resisting System

After the quantification of the load acting on the structure including both lateral and gravity loads. A load resisting system is selected to maintain the overall stability and integrity of the structure under high seismic events. As mentioned previously the lateral load resisting system selected in this research are braced frame with chevron configuration and cross bracing configuration Figure 8. Next, the design and some details of these systems are presented. For both braced frames, the structural steel was assumed to be $A992$ with modulus of elasticity $E = 29000ksi$ and yield strength $f_y = 50ksi$.

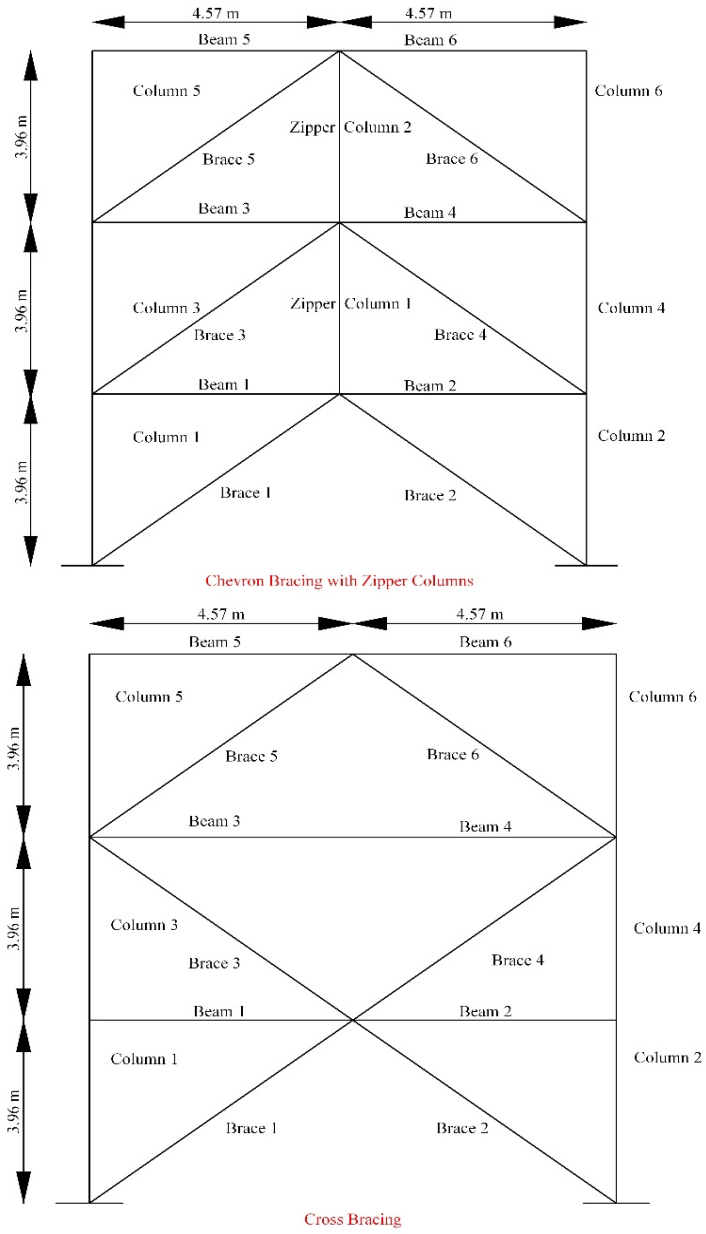

Figure 8 Configuration for Braced Frames

4.2.1 Braced Frame: Chevron Bracing Configuration

The chevron braced frames are one of the type of special concentrically braced systems (SCBFs) in which proper detailing and design can lead to high performance system with good ductility and energy dissipation proficiency [44]. However, these systems can exhibit typical

braced frame problems under high seismicity. Under large lateral displacements the braces in compression buckles prematurely and its axial load carrying capacity is decreased tremendously while the tension in the braces continues to increase without failing. This mechanism creates unbalanced vertical forces on the beam, and thus the overall lateral strength of the system is reduced. In order to counteract this effect, the zipper columns can be added at the intersection of the beam and the braces [45]. Here zipper columns with partial height zipper mechanisms is adopted as it results in better distribution of the loads and energy distribution over the height of the structure and thus maintaining the stability of the structure.

In order to ensure the system behaves in the intended manner, a two-fold design phase is proposed. In the first phase, the frame member sizes are determined to resist the lateral and the gravity loads calculated in the previous sections. This corresponds to the strength design of the system without the utilization of the zipper column [45]. Hollow Steel Sections (HSS) members are used for braces. The brace sizes are calculated using the software SAP2000. The second phase involves the capacity design of the system in which the zipper columns are introduced to resists the vertical unbalanced force generated by the brace at each individual levels [43]. The Table 6 mentioned below lists the selection of the member size obtained after the design analysis Figure 9.

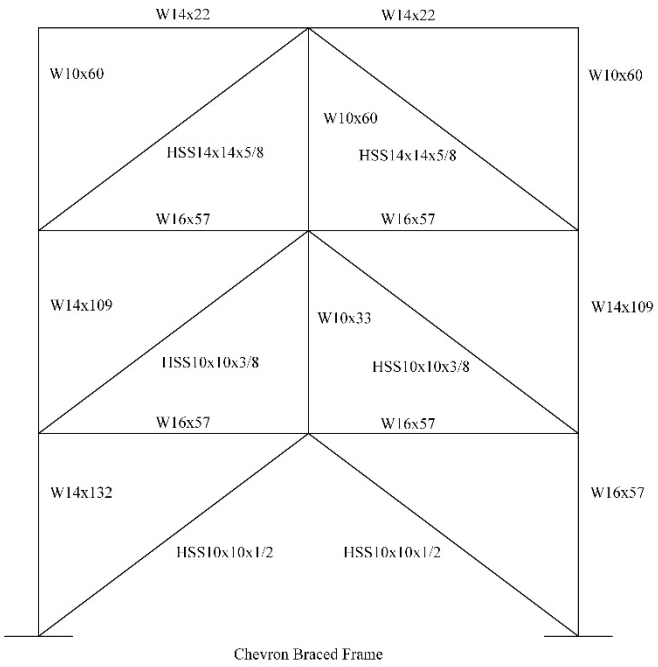

Figure 9 Calculated Sections for Chevron Braced Frame with Zipper Columns

Table 6 List of section for Chevron braced frame

Floor	Beam Sections	Column Sections	Brace Sections	Zipper Column
First floor	W16X57	W14X132	HSS10X10X1/2	
Second Floor	W16X57	W14X109	HSS10X10X3/8	W10X33
Third Floor	W14X22	W10X60	HSS14X14X5/8	W10X60

4.2.2 Braced Frame: Cross Bracing Configuration

The design methodology of this system is straightforward unlike chevron bracing system. This system is designed by first deciding the configuration of the braces in the lateral load resisting system and then subjecting it to lateral loads. SAP2000 is used to calculate the member size for the braces. Hollow Steel Sections (HSS) members are used for braces. Similarly, the columns are designed to withstand the gravity loads and the equivalent lateral loads, W section is

utilized for the column section. The beam section for the system is kept similar to the ones used in the SAC steel project [42]. The Table 7 mentioned below lists the sizes of members used at each floor.[43] Figure 10.

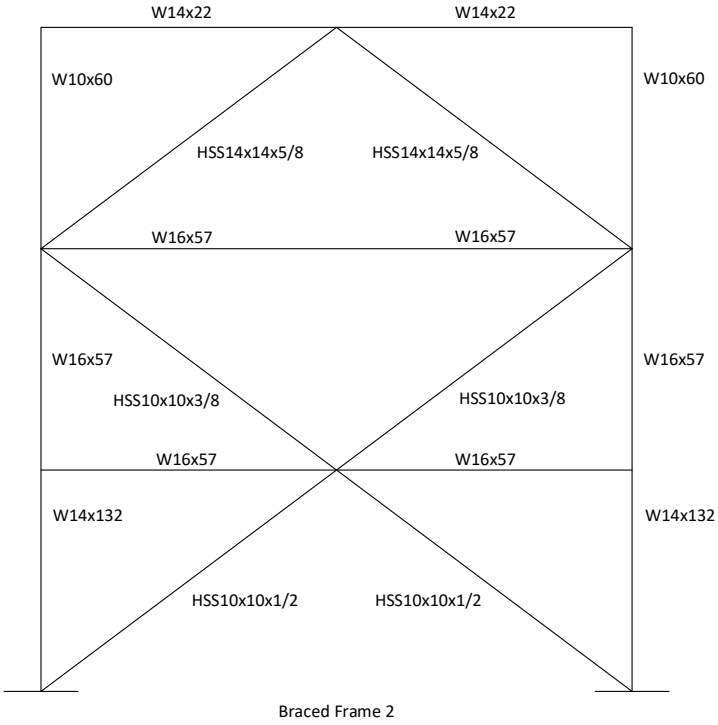

Figure 10 Calculated Sections for Braced Frame with Cross Bracing Configuration

Table 7 List of sections for Cross bracing braced frame

Floor	Beam Sections	Column Sections	Brace Sections
First floor	W16X57	W14X132	HSS10X10X1/2
Second Floor	W16X57	W14X109	HSS10X10X3/8
Third Floor	W14X22	W10X60	HSS14X14X5/8

4.3 Numerical Modeling of Braced Frames

For numerical modeling and analysis of the braced frames, the open source software ZEUS-NL is used. ZEUS-NL is an advancement of the earlier analysis packages ADAPTIC and

INDYAS. This is an analysis and simulation platform developed at MAE (Mid-America Earthquake Center) at University of Illinois at Urbana Champaign. It is a state-of-the-art 3D static and dynamic analysis platform specifically developed for earthquake engineering applications. Its extreme efficiency, accuracy, verification and user-friendly graphical user interface made it appropriate for the current problem. It can carry out inelastic large displacement analysis for complex frames using the fiber approach and it has a suite of commonly used material models and elements [46].

4.3.1 Modeling Details

Beams, Columns and Braces

The beams, columns and the braced elements are modeled as fiber sections where each member is divided into 10 sub-elements. A bilinear elasto-plastic model with kinematic strain hardening material, Figure 11 is utilized for the elements where Young's modulus $E = 29000ksi\ (199.94kN/m^2)$, yield strength $f_y = 50ksi\ (0.344kN/m^2)$ and strain hardening factor $\mu = 0.03$.

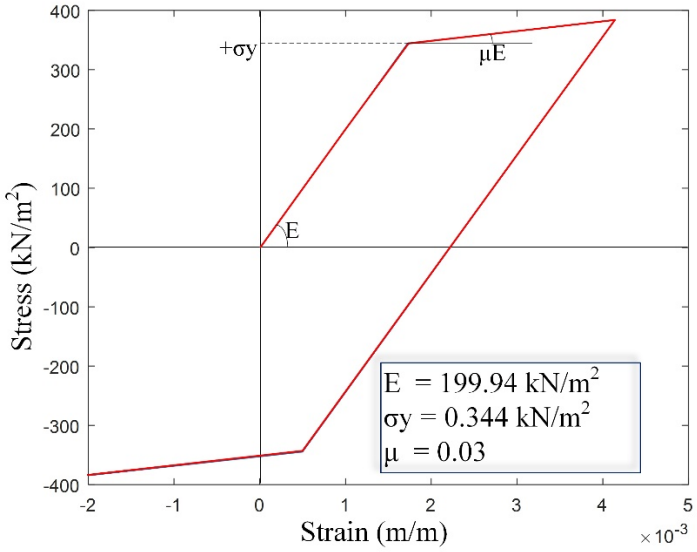

Figure 11 Bilinear Elasto Plastic Material

Joint Element

The end condition of the braced frames in the model is taken as 'pin-connection'. In order to assign this condition in the model, a zero length spring element is assigned to the brace's ends with the initial stiffness of the spring $K_0 = 1x10^{-21} kN/m^2$. More detail on the interaction with the elements can be helpful from the Figure 12 mention below. In addition to this, the initial imperfections in the braced are assumed to be in-plane with 0.2% length of the braces in the model ($L_{eff}/500$, where L_{eff} is the effective length of the brace). Shear tab connection is also assigned between columns and beams when there is no brace connected to them.

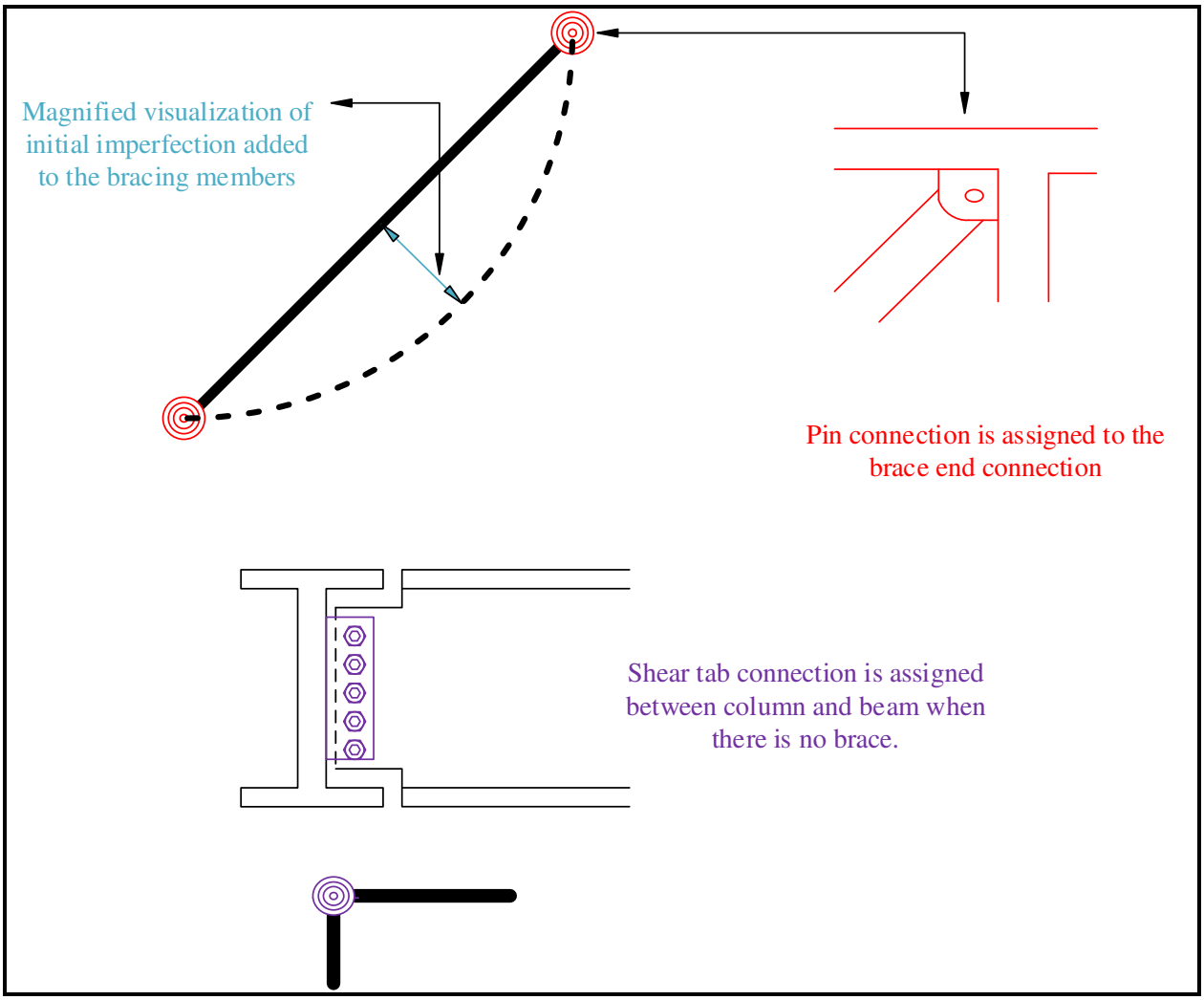

Figure 12 Visualization of joint element and imperfection in braces

Damping

Structural damping can be defined as the phenomenon that makes any vibrating body or structures to decay the amplitude of motion gradually by means of energy dissipation through various different mechanism. For dynamic analysis, it is crucial to appropriately model damping mechanisms in the structural model in order to accurately predict the structural responses. The equation of motion for dynamic systems can be written as

$$[M]\left(\frac{d^2x}{dt^2}\right)+[C]\left(\frac{dx}{dt}\right)+[K]\left(x(t)\right)=F_{stat}+F_{dyn} \tag{4.13}$$

where [C] is the damping matrix, [M] is the mass of structure, [K] is the stiffness of the structure. In finite element modeling, the damping is usually defined using Rayleigh damping (due to its convenience)

$$C=\eta_M M+\eta_K K \tag{4.14}$$

where η_M is the mass proportionality constant and η_K is the stiffness proportionality constant. The relationships between the modal equations and orthogonality conditions allow the damping or damping ratio to be rewritten as

$$\xi_i=\frac{1}{2\omega_n}\eta_M+\frac{\omega_n}{2}\eta_K \tag{4.15}$$

where ξ_i is the damping ratio and ω_n is the frequency for the mode *n*.

In order to determine the mass and stiffness proportionality for a given damping ratio (e.g., 5%, which is used for the later examples), eigenvalue analysis of the models need to be done to calculate ω_n first. Typically, we target a certain damping ratio for the fundamental mode, in which case the fundamental frequency is used to calculate the coefficients η_M and η_K .

4.3.2 Validation of the Numerical Model in ZEUS-NL

To validate the above modeling approach and the accuracy of the numerical model in ZEUS-NL, an example braced frame from OPENSEES is analyzed, and the results are validated against published results obtained from analysis by OPENSEES. More specifically, the results from pushover analysis, dynamic analysis (interstory drift ratio) and eigenvalue analysis are compared [47] and the comparisons are shown in Figure 13,Figure 14 and Figure 15. As can be

seen, ZEUS-NL gives very close results to OPENSEES for all the analysis cases. The small discrepancies in the dynamic analysis results could be due to different numerical schemes in solving the equation of motion in these two software.

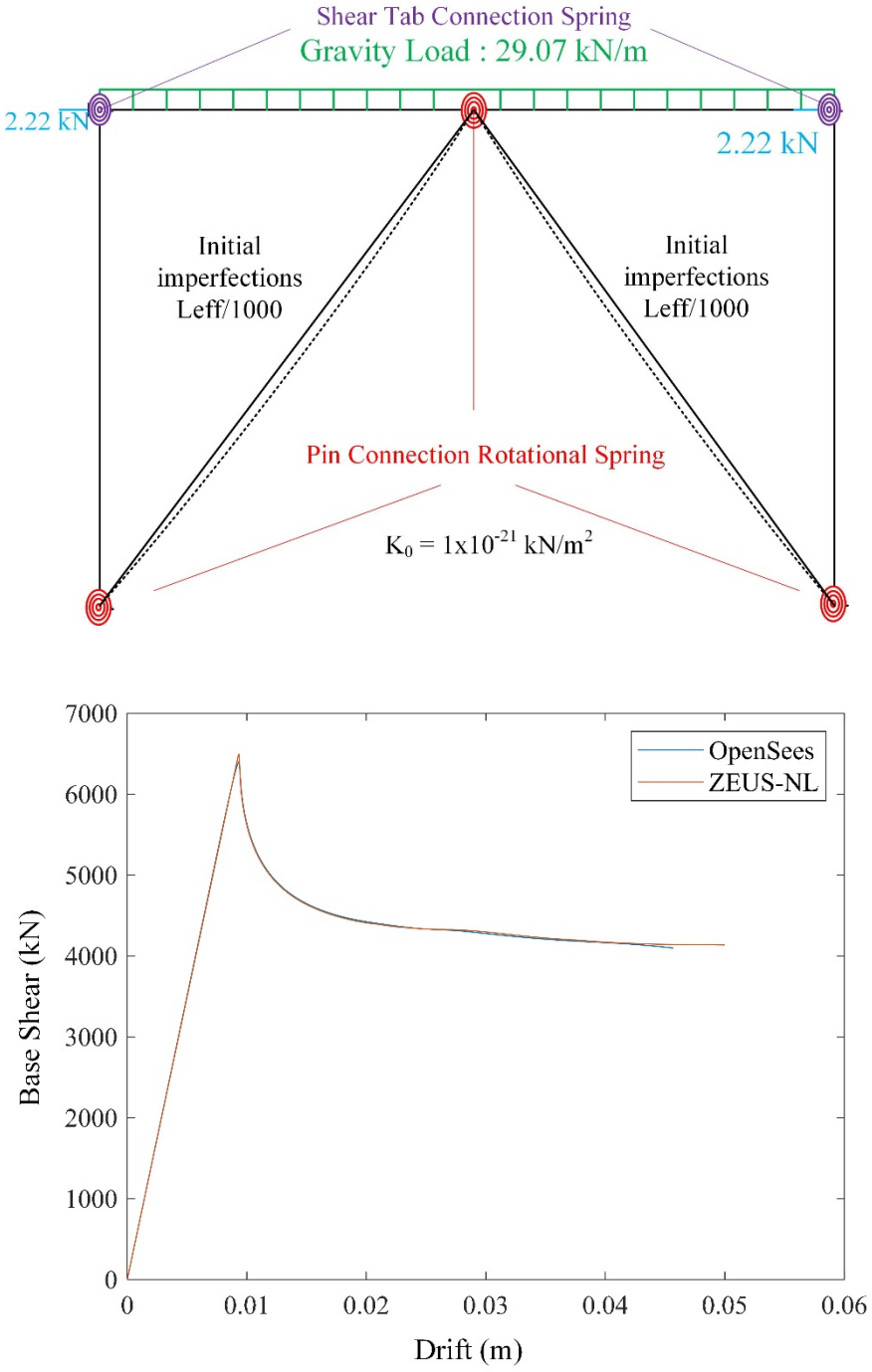

Figure 13 Model Detailing with Pushover Comparison between OPENSEES and Zeus-NL

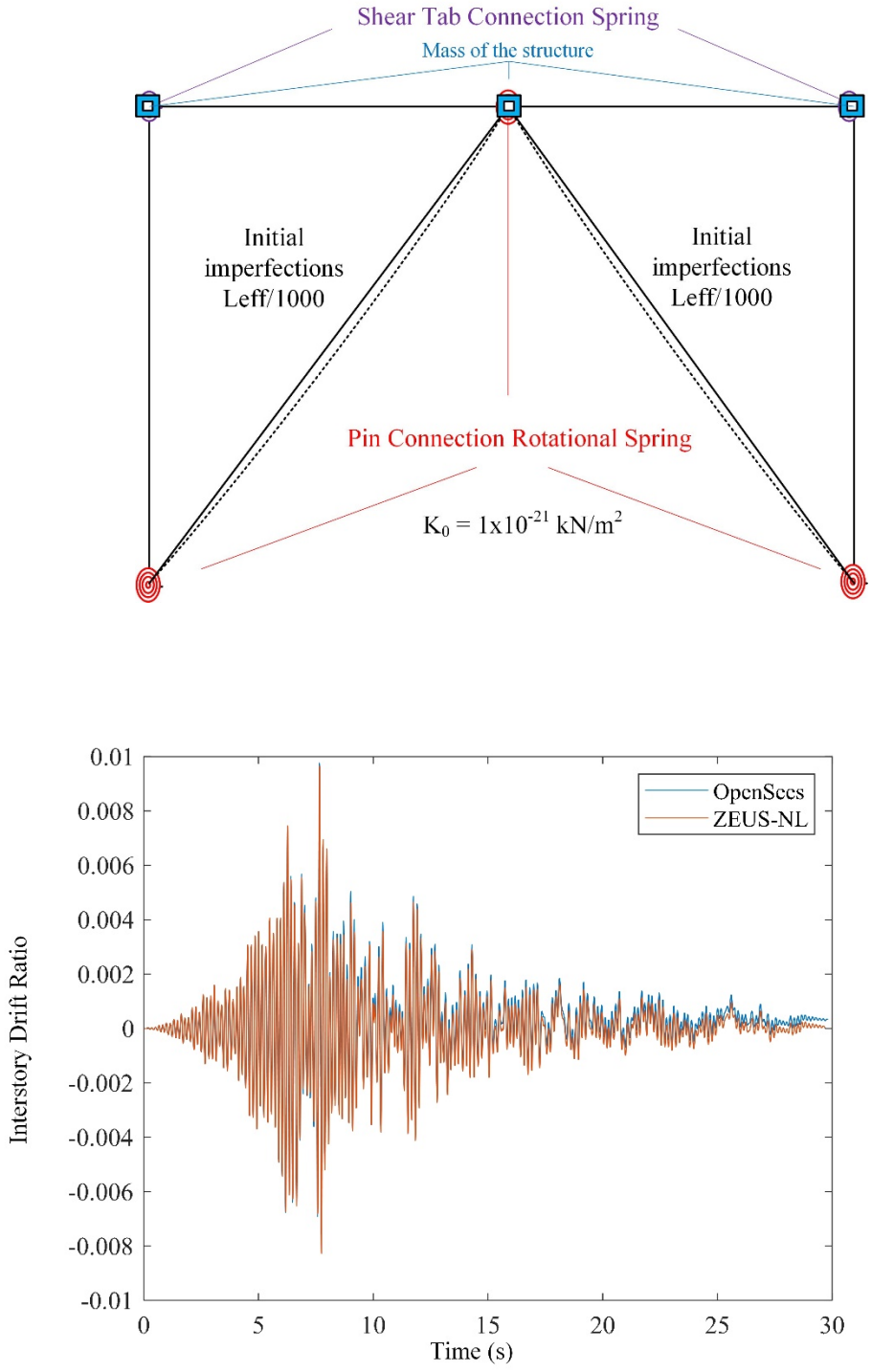

Figure 14 Model detailing and Interstory drift ratio comparison between OPENSEES and Zeus-NL

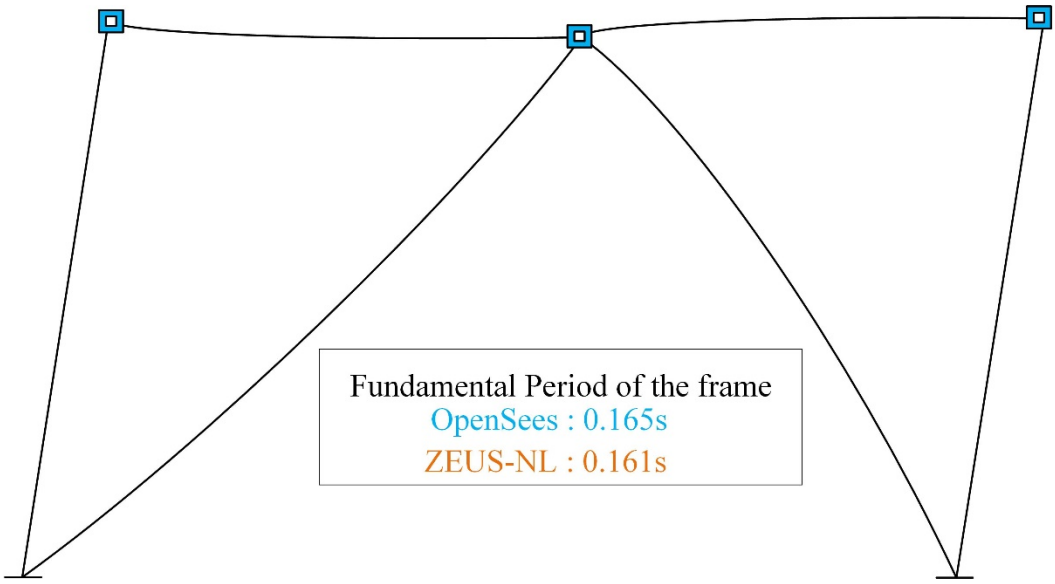

Figure 15 Eigenvalue Analysis comparison between OPENSEES and Zeus-NL

4.3.3 Numerical Models for Braced Frames

After validating the modeling approach in ZEUS-NL, the 3-story braced frames were modeled similarly, e.g., to achieve reasonable accuracy each member was divided into 10 elements and each brace member was given initial imperfection as previously described. The Figure 16 below provides the final braced frame with chevron and cross bracing configuration respectively and also the brace members are magnified to make the imperfections distinctive [43]. Rotational spring is used to model the shear tab connection at the top story beam for both frames and also in the first floor for the cross bracing braced frame.

To gain insights on the dynamic properties and performance of the braced frames, eigenvalue analysis and pushover analysis were carried out using the developed numerical models in ZEUS-NL. Figure 17 shows the mode shapes for the fundamental mode and the chevron braced frame has a period of 0.708s while the cross braced frame has a slightly longer period of 0.72s.

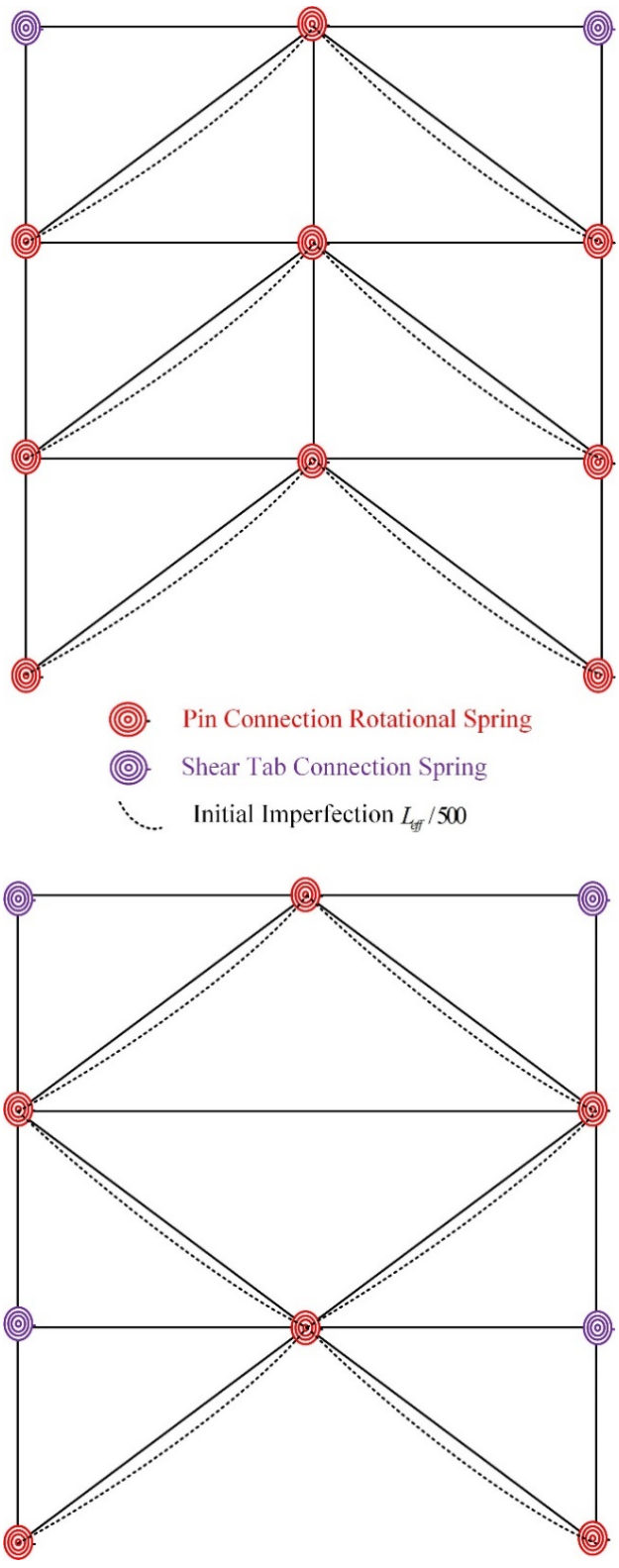

Figure 16 Model details for chevron and cross bracing configurations Braced Frames

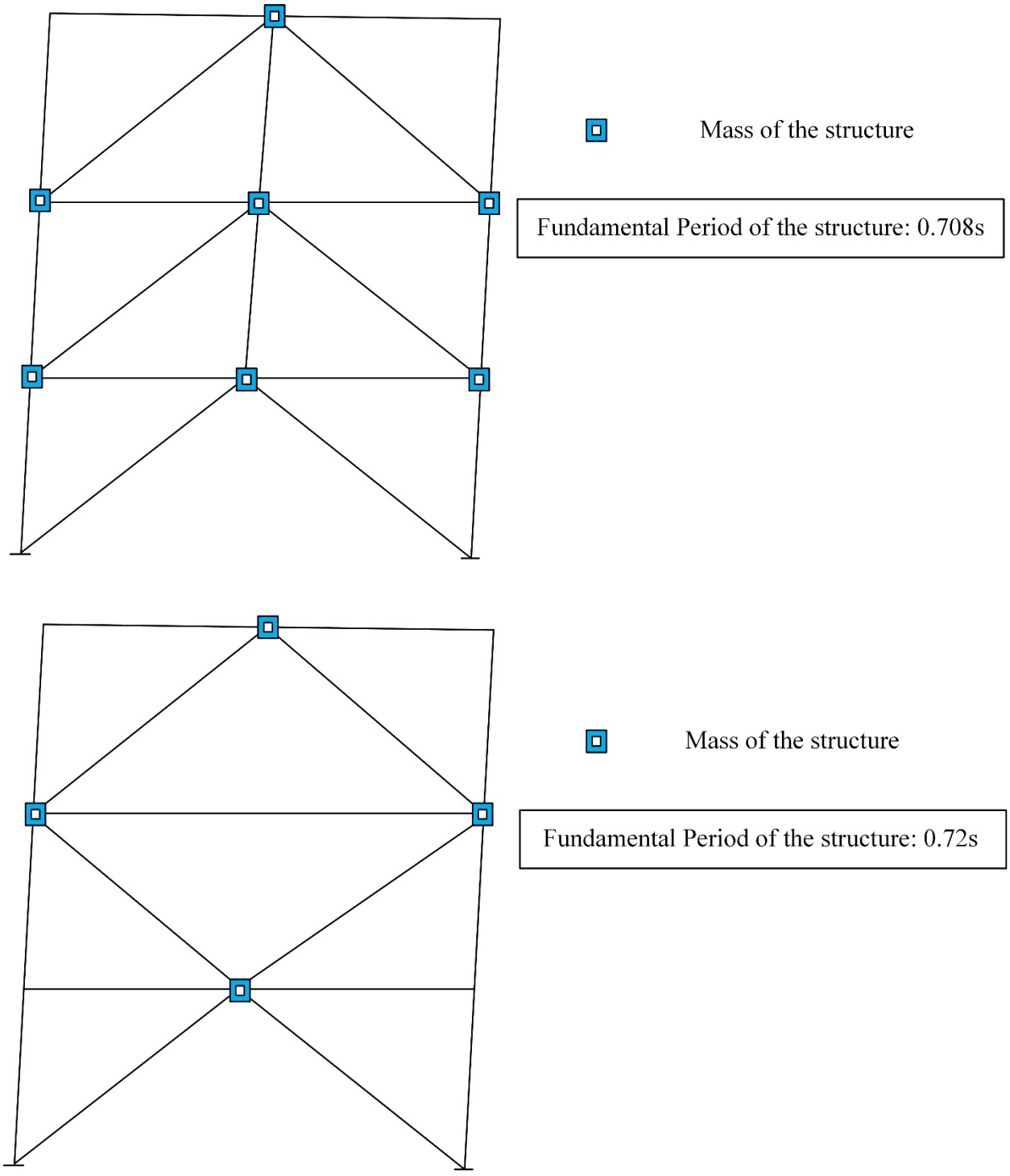

Figure 17 Fundamental period and modal shape for both braced frames

The pushover analysis is a static method of determining the performance and behavior of the structure under monotonically increasing lateral loads acting in each floor. In this study the

lateral loads can be evaluated using SAP2000 and its distribution on each floor can be obtained from the Table 5 and displacement control is adopted during loading phase till it reaches limit state. The Pushover Analysis results are shown in the Figure 18 [48]. It can observed from the pushover analysis is that the Chevron braced frame with zipper column showed a similar trend from the experimental results obtained from the research [49]. It also confirms that the zipper columns can enhanced the performance of the system as there is still some strength left after the brace buckles.

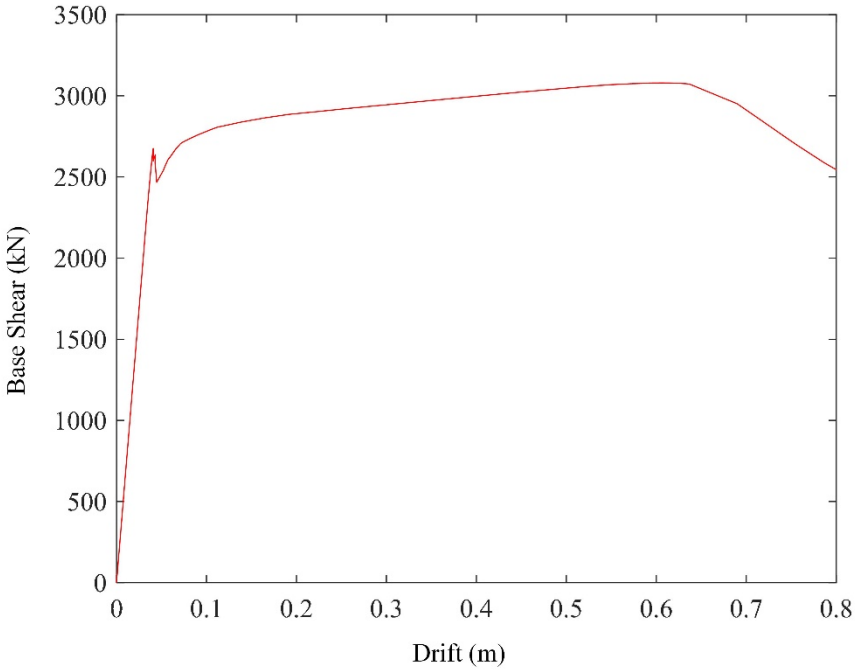

Figure 18 Pushover Curve for Chevron Braced Frame with Zipper Columns

Similarly pushover analysis is carried out for the Cross bracing frame to predict the inelastic response of the structure. It can be observed from the curve that strength and stiffness of the structure after yielding decreased exponentially which confirms the facts that the brace members are the primary component to provide lateral strength and it show the general behavior

of the system confirmed from the previous studies done in 0.The pushover curve for this braced frame is mentioned in Figure 19.

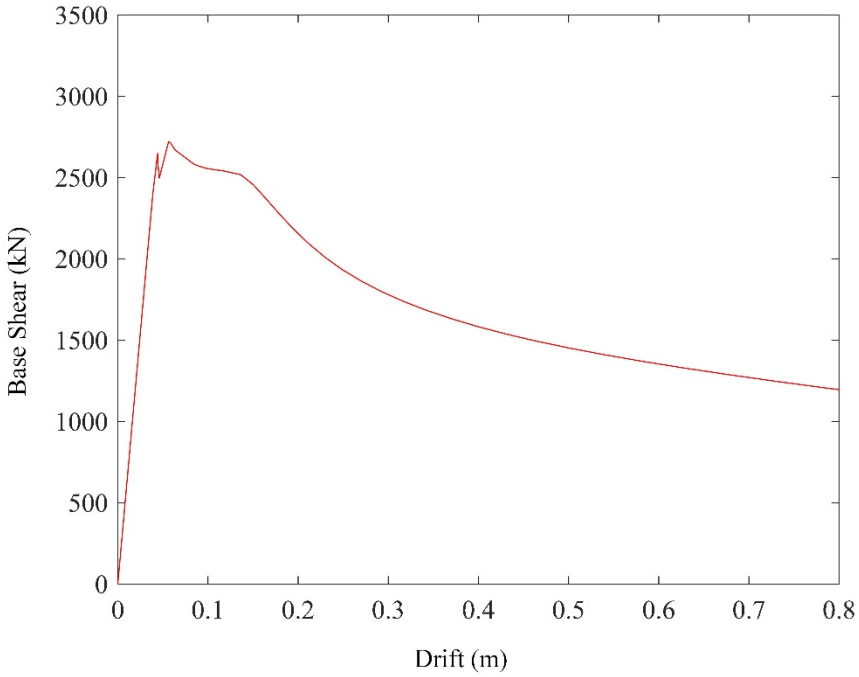

Figure 19 Pushover Curve for Cross Bracing Braced Frame

CHAPTER 5:STOCHASTIC GROUND MOTION MODEL

For dynamic analysis of the braced frames under earthquake excitations, the seismic hazard needs to be properly modeled. In this study, the probabilistic excitation model described in [50] is adopted. The near-fault stochastic ground motion (i.e., the acceleration time history) is established by modeling the near-fault characteristics such as low-frequency (long period) and the high frequency component independently and then combining them to form the final acceleration time history [23]. For completeness, this model is briefly described in the following sections.

5.1 High Frequency Component

In order to model the high frequency (>0.1-0.2Hz) component of the ground motion, a point source stochastic model is selected. This model was developed by utilizing the physics of fault rupture at the source and the propagation of the seismic waves till it reaches the structural site through ground medium [40]. Under this model the ground motion's radiation spectrum $A(f)$ is a function of frequency f whose parameters also depend on the seismicity characteristics such as moment magnitude M and rupture distance r. In addition to this, an envelope function is used to assess the duration of the ground motion, which also depends on the seismicity characteristics [50]. The combination of the frequency and time functions described below defines the high frequency component of the ground motion. For the point-source model, the two corner point source model proposed by [51] is used because of its equivalence in a

spectral sense to the finite-fault model and its capability to generate realistic near fault ground motions [23].

According to the point-source model, the acceleration time history for a specific earthquake event M and the source distance r can be obtained by modulating a white noise sequence $Z_w = [Z_w(i\Delta t): i = 1, 2, \ldots\ldots N_T]$ first by the time envelope function $e(t)$ and then by the radiation spectrum $A(f)$. So the white noise sequence is first multiplied with the envelope function and then the resulted sequence is transformed to the frequency domain. After that the sequence is normalized by the square of the mean square of the amplitude domain and multiplied by radiation spectrum $A(f)$. Finally, the resulted sequence is transformed back to the time domain to obtain the acceleration time history[40]. The uncertain model parameters associated with high frequency component of the earthquake is represented as θ_q , this corresponds to the displacement source spectrum characteristics f_a, f_b , and e where f_a and f_b are the lower and upper frequencies and e is the weighting parameter. In addition, there are parameters related to the local site diminution $\mathbb{k}_o$ and f_{max} and also the parameters associated with temporal envelope function T_w, λ_t, η_t where T_w is the duration of ground motion. A more detailed description is provided in the (APPENDIX A: POINT SOURCE MODEL).

The parameters f_a, f_b, e and T_w corresponds to the seismicity characteristics (M and r) while the remaining parameters are associated with site's tectonic characteristics. Now the probability density function is assigned to these parameters that represents the uncertainties in the ground motion excitation [52]. These uncertainties provide synthetic ground motions with increased variability that is comparable to the variability in real ground motions, and also more

importantly facilitates evaluation of the importance of different uncertain parameters affecting in system's performance [53].

The distribution of each uncertain parameter for θ_q are chosen according to [54]. The parameter $\mathbb{k}_o$ follows uniform distribution within [0.02 0.04], for the rest of the remaining parameters lognormal distribution is assumed with coefficient of variance (c.o.v) $\gamma_f = 20\%$ for the parameters corresponds to the frequency characteristics of the amplitude spectrum while (c.o.v) $\gamma_t = 40\%$ corresponds to the temporal characteristics of the time-domain envelope. Similarly, based on previous research [55] the median values of the parameters f_{max}, λ_t and η_t are assigned as 25 Hz , 0.2 and 0.05 respectively. The median values of f_a, f_b, e and T_w can be calculated through predictive relationships from the equations in Appendix A. The following auxiliary variables are assigned in order to evaluate the influence of the uncertainty in the predictive relationships more precisely [50].

$$\begin{aligned} e_a &= [\ln(f_a / \overline{f}_a)] / \gamma_f,\ e_b = [\ln(f_b / \overline{f}_b)] / \gamma_f \\ e_e &= [\ln(e / \overline{e})] / \gamma_f,\ e_t = [\ln(T_w / \overline{T}_w)] / \gamma_t \end{aligned} \tag{5.1}$$

These auxiliary variables corresponds to the uncertainties in the f_a, f_b, e and T_w. Based on the probability models discussed earlier these variable also follows a standard Gaussian distribution and are utilized to describe the seismic hazard characteristics as it is not dependent on remaining hazard parameters. So the uncertain model parameters related with high frequency component of the near fault ground motions are $\theta_q = \{\mathbb{k}_o, f_{max}, \lambda_t, \eta_t, e_t, e_a, e_b, e_e\}$ [50].

5.2 Long Period Pulse

The long period pulse characteristics of the near fault ground motion can be derived from the mathematical representation of the near fault ground motion developed by Mavroeidis and Papageorgiou, the mathematical expression of the ground motion velocity pulse can be described by the following equation.

$$V = \frac{A_p}{2}[1+\cos(\frac{2\pi f_p}{\gamma_p}(t-t_o))]\cos(2\pi f_p(t-t_o)+\nu_p)$$
$$t \in [t_o - \gamma_p / \left(2f_p\right), t_o + \gamma_p / \left(2f_p\right)]; =0 \text{ otherwise} \tag{5.2}$$

where A_p is the signal amplitude, f_p describes dominating frequency, v_p describes phase angle, γ_p denotes number of half cycles and t_o is the time shift to specify the peak of the envelope. All the different parameters mentioned above have specific physical meanings corresponding to the seismicity characteristics such as moment magnitude M or rupture distance r. Through regression analysis, predictive relationships for the median parameter values had been established and also the uncertainty associated with them [56–58]. The pulse amplitude A_p and period T_p are taken as

$$A_p = I_p 10^{0.9(2.04-0.032r+e_{Ap})} \tag{5.3}$$

$$T_p = 10^{-2.9+0.5M+e_{Tp}} \tag{5.4}$$

where e_{Ap} and e_{Tp} are zero mean Gaussian variables with standard deviations as 0.187 and 0.143 respectively and I_p is the indicator function describing whether the pulse exist or not. The probability density function for γ_p is assigned as Gaussian variables with mean 1.8 and standard deviation 0.3, and v_p is assumed to follow an uniform distribution between $[0,\pi]$ respectively [50].

Since not all near-fault excitations will have a velocity pulse, the probability of its occurrence needs to be integrated in the stochastic model as well. This is established by introducing a random variable ε_p with outcomes as either [yes, no]. The probability of having pulse (i.e., probability of $\varepsilon_p = yes$) can be estimated as a function related to the seismicity characteristics. If the origin of the seismic hazard is assumed to be at strike-slip faults, the probabilistic model proposed in [59] can be used to predict this probability,

$$P(\varepsilon_p = yes \mid r, s) = \frac{1}{1+\exp(0.642+0.167r-0.075s)} \tag{5.5}$$

where r is the rupture distance and s is the distance between epicenter and site projection on the fault plane surface. Quantification of s is taken as ¼ of the total length of rupture L, which can be predicted through [60]

$$\log_{10}(L) = -3.55 + 0.74M + e_L \tag{5.6}$$

where e_L is a variable with zero mean and 0.23 standard deviation. Lastly ε_p is defined using an indicator function I_p meaning if I_p is 1 then there is probability of occurrence of pulse ($\varepsilon_p = yes$) or else 0 [50].

So all the uncertain parameters the represents the long period pulse can be denoted as $\theta_p = \{e_{Ap}, e_{Tp}, \gamma_p, v_p\}$, the parameters are independent from the remaining seismic hazard characteristics. In addition, the uncertain parameters associated with pulse occurrence include e_L and ε_p [50].

5.3 Near-Fault Ground Motion Model

The stochastic model is finally established by combining the two components described above to generate the acceleration time-history. This model captures all the essential components described in the mathematical representation of near fault ground motion [23]. A visual representation of the above details is shown in Figure 20 where each component is modelled individually and then combined to obtain the final ground motion. For prediction of structural performance and for risk assessment purpose in the future, stochastic ground motion model can be used to simulate ground motions, especially for regions where there is not enough recorded ground motion data. Additionally, this model can also accommodate different earthquake faults and different soil conditions based by changing the parameters in the model.

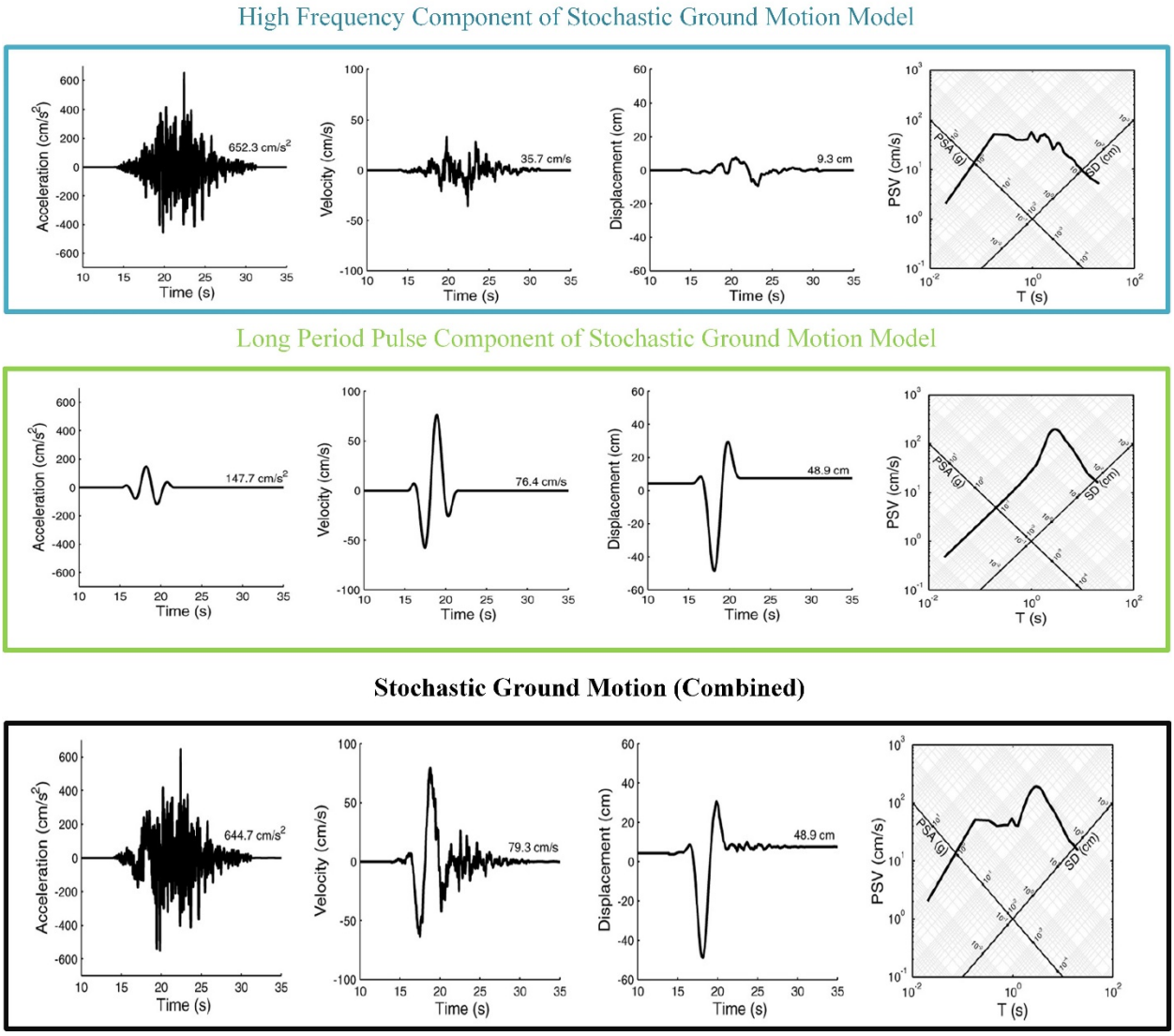

Figure 20 Near-fault ground motion with long period pulse and high frequency component

CHAPTER 6:RESULTS AND DISCUSSIONS

6.1 Implementation Details

6.1.1 Overall Implementation

To evaluate the seismic collapse risk, the stochastic simulation based approach for risk estimation described in Section 3.1 is used. The simulation-based approach requires many evaluations of the response of the structure under simulated ground motions, which corresponds to nonlinear time history analysis and is the most computationally expensive task in the overall seismic risk assessment. To reduce the computational effort, parallel computing was used and ZEUS-NL structure models under multiple ground motions were run simultaneously in "batch mode". These ground motions were generated using the stochastic ground motion model discussed in CHAPTER 5 . For each simulation, the maximum interstory drift ratio of the braced frame under the corresponding ground motion was calculated and structure collapse is defined as the maximum interstory drift ratio exceeding the collapse threshold (i.e., 0.05%). Then using results from all the simulations, the seismic collapse risk is calculated using Eq. (3.2) for both braced frames.

Then information from this set of simulations is used within accept-reject sampling algorithm to generate samples from the failure distribution $p(\boldsymbol{\theta} \mid F)$. These failure samples are used within the sample-based approach discussed in section 3.3.2 to efficiently evaluate the marginal failure distribution $p(\theta_i \mid F)$ via Kernel density estimation (KDE) and further the relative entropy (e.g., using Eq. (3.10) for sensitivity analysis. The relative entropy values are used to identify the importance of different uncertain model parameters in the stochastic ground motion model towards seismic collapse risk.

To investigate the impact of near-fault pulses in the ground motion on the seismic collapse risk, the case when near-fault pulse is not included is also considered. To calculate the corresponding seismic collapse risk, instead of running additional simulations (which are computationally expensive), in this study the Bayes' theorem was used to directly calculate the seismic collapse risk when there is no near-fault pulse using the same set of simulations mentioned above. This led to significant improvement in efficiency. Figure 22 shows the overall implementation flowchart. Details regarding the selection of proposal density for the stochastic simulation and the use of Bayes' theorem are discussed next.

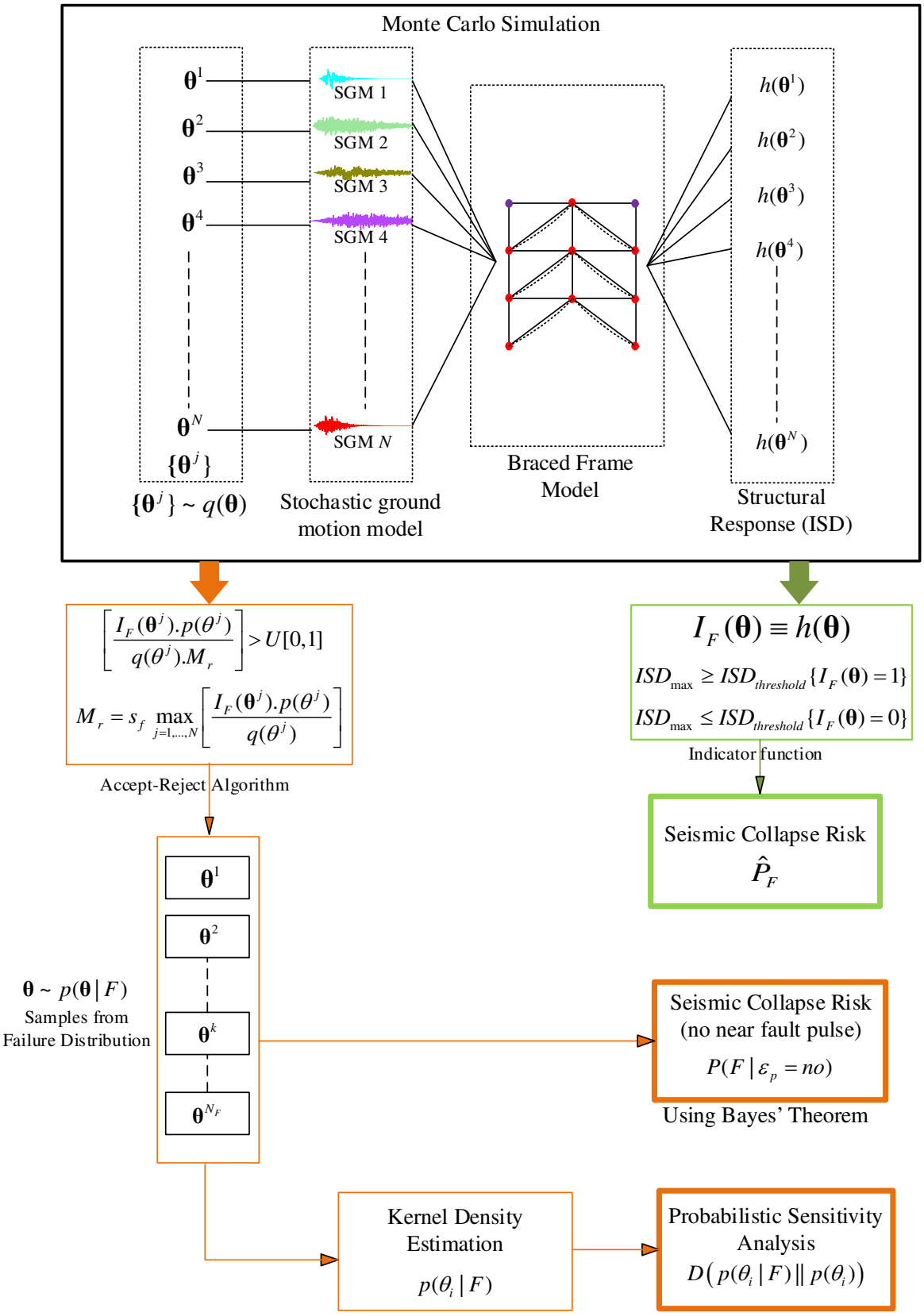

Figure 21 Flowchart for simulation based approach for seismic collapse risk assessment and probabilistic sensitivity analysis

6.1.2 Selection of Proposal Density

To carry out the stochastic simulation, we need to have some proposal density $q(\boldsymbol{\theta})$ to generate realizations for the model parameters $\boldsymbol{\theta}$. The selection of this proposal density will affect the overall efficiency and accuracy of the seismic collapse risk estimation and the efficiency of the accept-reject sampling algorithm.

Since typically collapse corresponds to rare event, if we directly use the prior distribution $p(\boldsymbol{\theta})$ as proposal density, we would need many simulations to generate realizations that will lead to collapse. From the view of importance sampling, we need to have a proposal density that can simulate more samples that lead to collapse. Intuitively, large earthquakes or earthquakes with strong intensity will tend to lead to structural collapse. It makes sense to select a proposal density that generates more samples with large earthquakes. To this end, proposal densities are prescribed for M (moment magnitude), r (rupture distance) and A_p (amplitude of pulse) with the idea that $q(\boldsymbol{\theta})$ should be selected so that there are more samples for large M, small r and large A_p.

For the case studies, the prior distributions for the above uncertain model parameters are as follow. The uncertainty in the moment magnitude for seismic events, M is modeled by Gutenberg-Richter relationship truncated to the interval $\left[M_{min}, M_{max}\right] = \left[5.5,\ 8\right]$ which leads to the following PDF

$$p(M) = \frac{b_M e^{(-b_M M)}}{e^{(-b_M M_{\min})} - e^{(-b_M M_{\max})}} \tag{6.1}$$

where $b_M = 0.9 log_e(10)$. The rupture distance r is assumed to follow a lognormal distribution with median $r_{med} = 18\ km$ and c.o.v of $r_{cov} = 45\%$. The amplitude of pulse A_p has the form of

$$A_p = I_p 10^{0.9(2.04-0.032r+e_{Ap})} \tag{6.2}$$

where r is the rupture distance, I_p is an indicator function describing the existence of pulse or not, e_{Ap} follows normal distribution with mean $\mu_{e_{Ap}} = 0$ and standard deviation $\sigma_{e_{Ap}} = 0.187$.

The following proposal densities are used for the above uncertain parameters. $q(M)$ is selected as a truncated Gaussian distribution between $[a,b] = [5.5,\ 8]$ with mean $\mu_{q(M)} = 7.5$ and standard deviation $\sigma_{q(M)} = 1$. The corresponding PDF is in Eq. (6.3) where the erf is the gauss error function that assists in proving solution to a stochastic differential equation.

$$q(M) = \frac{\sqrt{\frac{2\pi}{\sigma^2}}}{2}(erf(\sqrt{\frac{\sigma^2}{2}}\cdot(a-\mu)) - erf(\sqrt{\frac{\sigma^2}{2}}\cdot(b-\mu))) \tag{6.3}$$

The proposal density for r is selected as lognormal distribution with median $r_{med} = 8\ km$ (i.e., smaller rupture distance) and c.o.v of $r_{cov} = 45\%$ .The proposal density for amplitude of pulse characteristics depends upon the new proposal density for rupture distance and e_{Ap}; the latter is selected as normal distribution with mean $\mu_{q(e_{Ap})} = 0.15$ and standard deviation $\sigma_{q(e_{Ap})} = 0.187$. For the rest of the parameters, the corresponding prior distributions are used.

With the above selection of proposal density, *N*=5000 samples are generated for the stochastic simulation. Then based on the information from these simulations, the accept-reject algorithm is used to generate samples from the failure distribution. With the above selection of proposal density, the accept-reject sampling is carried out as follows while the general steps for accept-reject sampling can be found in APPENDIX B: ACCEPT-REJECT ALGORITHM. In the current case, the target density is $p(\boldsymbol{\theta}|\mathbf{F})$. It can be expressed in the equation below

$$p(\boldsymbol{\theta}|\mathbf{F}) = \frac{I_F(\boldsymbol{\theta}) \cdot p(\boldsymbol{\theta})}{P_F} \tag{6.4}$$

1) Generate u^j (uniform random numbers) from a uniform distribution within [0, 1].

2) For sample $\boldsymbol{\theta}^j$, accept it $\boldsymbol{\theta} = \boldsymbol{\theta}^j$ when the following condition is met; otherwise, reject the sample.

$$\left[\frac{I_F(\boldsymbol{\theta}^j) \cdot p(\theta_M{}^j) \cdot p(\theta_r{}^j) \cdot p(\theta_{A_p}{}^j)}{q(\theta_M{}^j) \cdot q(\theta_r{}^j) \cdot q(\theta_{A_p}{}^j) \cdot M_r} \right] > u^j \tag{6.5}$$

where $M_r = s_f \max_{j=1,\ldots,N} \left[\frac{I_F(\boldsymbol{\theta}^j) \cdot p(\theta_M{}^j) \cdot p(\theta_r{}^j) \cdot p(\theta_{A_p}{}^j)}{q(\theta_M{}^j) \cdot q(\theta_r{}^j) \cdot q(\theta_{A_p}{}^j) \cdot M_r} \right]$ and s_f is a scaling factor ($s_f \geq 1$) to ensure $M_r = \max \left[\frac{I_F(\theta^j) \cdot p(\theta_M{}^j) \cdot p(\theta_r{}^j) \cdot p(\theta_{A_p}{}^j)}{q(\theta_M{}^j) \cdot q(\theta_r{}^j) \cdot q(\theta_{A_p}{}^j) \cdot M_r} \right]$ over the entire domain Θ and not just over the available *N* samples, in general s_f is selected around1.2-1.3 so that efficiency of the sampling is not significantly decreased.

3) Repeat 1) and 2) for all the *N* samples.

Here, $I_F(\boldsymbol{\theta})$ is the indicator function whose value is 1 when ($ISD_{max} \geq ISD_{threshold}$) where ISD = interstory drift ratio. In the end, N_F failure samples are generated from the failure distribution $p(\boldsymbol{\theta}|\mathbf{F})$.

6.1.3 Estimation of Seismic Collapse Risk

Using the *N*=5000 simulations, with the above selection of proposal density, the seismic collapse risk of the braced frame under stochastic near-fault ground motions can be estimated by

$$\hat{P}_F = \frac{1}{N}\sum_{j=1}^{N} I_F(\boldsymbol{\theta}^j)\frac{p(\boldsymbol{\theta}^j)}{q(\boldsymbol{\theta}^j)} = \frac{1}{N}\sum_{j=1}^{N}\left(\frac{I_F(\boldsymbol{\theta}^j)\cdot p(\theta_M{}^j)\cdot p(\theta_r{}^j)\cdot p(\theta_{A_p}{}^j)}{q(\theta_M{}^j)\cdot q(\theta_r{}^j)\cdot q(\theta_{A_p}{}^j)}\right) \tag{6.6}$$

The c.o.v of the estimate, which indicates the accuracy of the estimate, can be calculated by

$$\delta = \frac{1}{\sqrt{N}}\frac{\sqrt{\frac{1}{N}\sum_{j=1}^{N}\left(\frac{I_F(\boldsymbol{\theta}^j)\cdot p(\theta_M{}^j)\cdot p(\theta_r{}^j)\cdot p(\theta_{A_p}{}^j)}{q(\theta_M{}^j)\cdot q(\theta_r{}^j)\cdot q(\theta_{A_p}{}^j)}\right)^2 - \left(\hat{P}_F\right)^2}}{\left(\hat{P}_F\right)} \tag{6.7}$$

For comparison purpose, the seismic collapse risk of the braced frame under stochastic ground motions without near-fault pulse is also calculated. As mentioned earlier, instead of running additional simulations (which are computationally expensive), the Bayes' theorem is used to directly calculate this seismic collapse risk using the same set of simulations. More specifically, the failure probability of the structure when there is no near-fault pulse in the ground motion, $P(F \mid \varepsilon_p = no)$, can be written as follows using the Bayes' theorem

$$P(F \mid \varepsilon_p = no) = \frac{P(\varepsilon_p = no \mid F)\cdot \hat{P}_F}{P(\varepsilon_p = no)} \tag{6.8}$$

where $\hat{P}_F$ is the failure probability calculated in Eq. (6.6) . $P(\varepsilon_p = no \mid F)$ corresponds to the probability of no pulse within the failure samples, and it can be estimated by Eq. (6.8).

$$P(\varepsilon_p = no \mid F) = N_{F,\varepsilon_p = no} / N_F \tag{6.9}$$

where $N_{F,\varepsilon_p = no}$ corresponds to the number failure samples that do not have near-fault pulse and N_F is the total number of failure samples generated using the accept-reject algorithm discussed

earlier. As to $P(\varepsilon_p = no)$, it corresponds to the marginal probability of no pulse under the prior distribution and has the following expression

$$P(\varepsilon_p = no) = \int P(\varepsilon_p = no \mid \boldsymbol{\theta}) p(\boldsymbol{\theta}) d\boldsymbol{\theta} \tag{6.10}$$

Using the same set of simulation discussed above (i.e., with $q(\boldsymbol{\theta})$ as proposal density), $P(\varepsilon_p = no)$ can be estimated through

$$\hat{P}(\varepsilon_p = no) = \frac{1}{N} \sum_{j=1}^{N} \left[\frac{P(\varepsilon_p = no \mid \boldsymbol{\theta}^j) \cdot p(\boldsymbol{\theta}^j)}{q(\boldsymbol{\theta}^j)} \right] \tag{6.11}$$

In the end, an estimate for $P(F \mid \varepsilon_p = no)$ can be established. Considering that N=5000 simulations are used for estimating $\hat{P}_F$ and $P(\varepsilon_p = no)$, if we assume good accuracy for these two estimates, then the main error for estimation of $P(F \mid \varepsilon_p = no)$ using Eq. (6.8) will come from the error in estimating $P(\varepsilon_p = no \mid F)$ using samples. The c.o.v of the estimate for $P(\varepsilon_p = no \mid F)$ using N_F samples is

$$\delta_{P(\varepsilon_p = no|F)} = \sqrt{\frac{1 - P(\varepsilon_p = no \mid F)}{N_F \cdot P(\varepsilon_p = no \mid F)}} \tag{6.12}$$

where $P(\varepsilon_p = no \mid F) = N_{F,\varepsilon_p = no} / N_F$ and $N_{F,\varepsilon_p = no|F}$ is the number of failure samples with no pulse and N_F is total number of failure samples. And the c.o.v for the estimate $P(F \mid \varepsilon_p = no)$ is the same as $\delta_{P(\varepsilon_p = no|F)}$ since $P(F \mid \varepsilon_p = no)$ is $P(\varepsilon_p = no \mid F)$ scaled by constant $\hat{P}_F / P(\varepsilon_p = no)$.

6.1.4 Estimation of Relative Entropy

For probabilistic sensitivity analysis, it is carried out to quantify the importance of uncertain model parameters towards the seismic collapse risk. Using the generated failure samples, the relative entropy values for each parameter can be calculated using the approach

discussed in Section 3.3.2. More specifically, the relative entropy for continuous variable θ_i corresponds to

$$D\left(p(\theta_i \mid F) \,\|\, p(\theta_i)\right) = \int_{\Theta_i} p(\theta_i \mid F) \ln\left[\frac{p(\theta_i \mid F)}{p(\theta_i)}\right] d\theta_i \tag{6.13}$$

Based on the failure samples, KDE is used to estimate $p(\theta_i \mid F)$, and $p(\theta_i)$ is the prior distribution of θ_i. Then the relative entropy $D\left(p(\theta_i \mid F) \,\|\, p(\theta_i)\right)$ is estimated using trapezoidal integration for the one-dimensional integral in Eq. (6.13).

In addition to the continuous model parameters in the stochastic near-fault ground motion model, to explicitly investigate the sensitivity of the seismic collapse risk with respect the existence of near-fault pulses, a pulse existence parameter ε_p is also defined, which is a discrete random variable, and takes values of $\varepsilon_p = yes$ or $\varepsilon_p = no$ where $\varepsilon_p = yes$ means there is near-fault pulse in the ground motion while $\varepsilon_p = no$ means there is no near-fault pulse in the ground motion. The relative entropy for discrete variable can be calculated as well where the integration for continuous variables becomes summation over all the values that the discrete variable can take. More specifically, the relative entropy for ε_p is calculated through

$$D\left(P(\varepsilon_p \mid F) \,\|\, P(\varepsilon_p)\right) = P(\varepsilon_p = yes \mid F) \log\left(\frac{P(\varepsilon_p = yes \mid F)}{P(\varepsilon_p = yes)}\right) + P(\varepsilon_p = no \mid F) \log\left(\frac{P(\varepsilon_p = no \mid F)}{P(\varepsilon_p = no)}\right) \tag{6.14}$$

Both $P(\varepsilon_p = no \mid F)$ and $P(\varepsilon_p = no)$ have been calculated in Eq.(6.9) and Eq.(6.11) when evaluating the seismic collapse risk when there is no near-fault pulse in the ground motion. $P(\varepsilon_p = yes \mid F) = 1 - P(\varepsilon_p = no \mid F)$ and $P(\varepsilon_p = yes) = 1 - P(\varepsilon_p = no)$. Plugging these values into Eq. (6.14) gives the relative entropy for ε_p. The importance of ε_p can be compared with other model parameters by comparing their relative entropy values.

6.2 Seismic Collapse Risk Assessment Results

This section presents the results for the seismic collapse risk of the Chevron Braced Frame and the Cross Bracing Braced Frame.

6.2.1 Chevron Braced Frame

With $N = 5000$ simulations, using Eq. (6.6), the seismic collapse risk or probability of failure of the Chevron braced frame is estimated to be around 8.87%, and the c.o.v of the estimate is 7.48%, which is evaluated using Eq. (6.7). The c.o.v is an indication of the accuracy of the estimate (for the seismic risk), typically c.o.v of 10% or less implies a good estimate. As can be seen the seismic collapse risk is relatively high. This can be attributed to the closeness of the structure site to the earthquake fault and the structure experiences stronger ground motion compared to structures that are situated far away from the earthquake fault (e.g., these structures would only experience far field earthquake ground motion). In addition, the variation of failure probability when different interstory drift ratio thresholds are used is plotted in Figure 22. As expected, the failure probability will decrease when the threshold increases. Also the c.o.v of the corresponding estimates is plotted against the threshold in Figure 23. Overall, the failure probabilities are estimated with relatively good accuracy (e.g., with c.o.v below or around 10%).

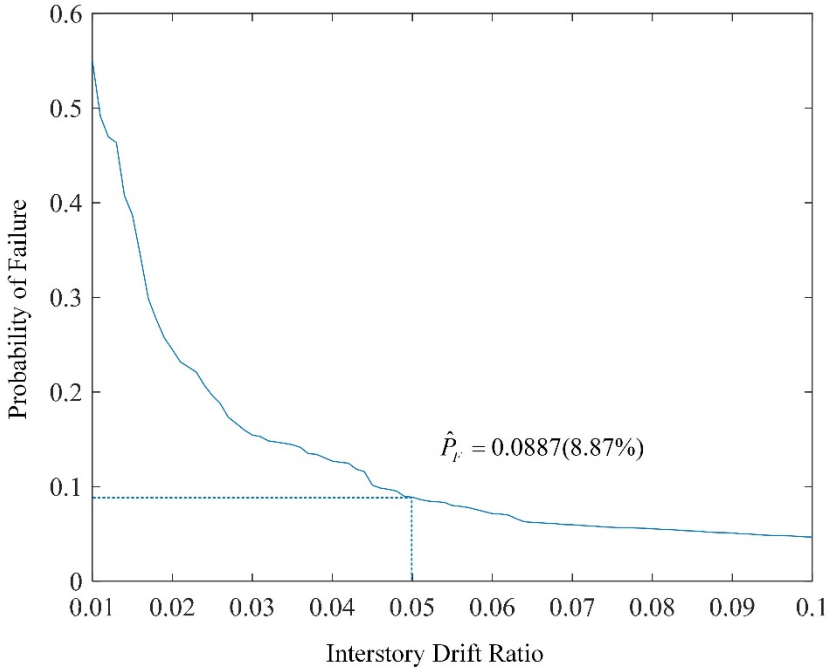

Figure 22 Failure probability against interstory drift ratio thresholds for Chevron Braced Frame

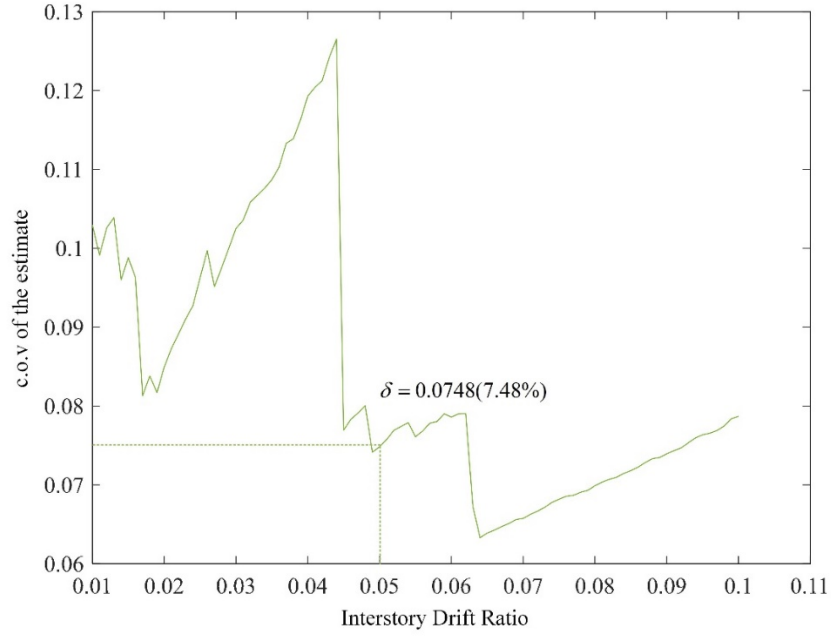

Figure 23 c.o.v of the failure probability estimates for different interstory drift ratio thresholds for Chevron Braced Frame

To investigate the impact of including or not the near-fault pulse in the stochastic ground motion on the seismic collapse risk of the Chevron Braced Frame, the seismic collapse risk when there is no near-fault pulse in the stochastic ground motion (i.e., only the high-frequency components) is also evaluated. As mentioned earlier, this is done using Eq. (6.8) without running additional simulations. More specifically, using Eq. (6.9) $P(\varepsilon_p = no \mid F)$ is estimated to be 68.47% and the c.o.v is 4.55%, which is evaluated using Eq. (6.12) Using Eq.(6.10), $P(\varepsilon_p = no)$ is estimated to be 95.17%. Therefore, the failure probability $P(F \mid \varepsilon_p = no)$ is estimated to be 6.39% with c.o.v of 4.55%. Compared to the failure probability (seismic collapse risk) of 8.87% when considering near-fault pulse in the ground motions, the seismic collapse risk of the Chevron Braced Frame is much smaller (i.e., at 6.39%) when there is no near-fault pulse in the stochastic ground motion. This comparison highlights the significant impacts of near-fault pulses on the seismic collapse risk estimation of the Chevron Braced Frame.

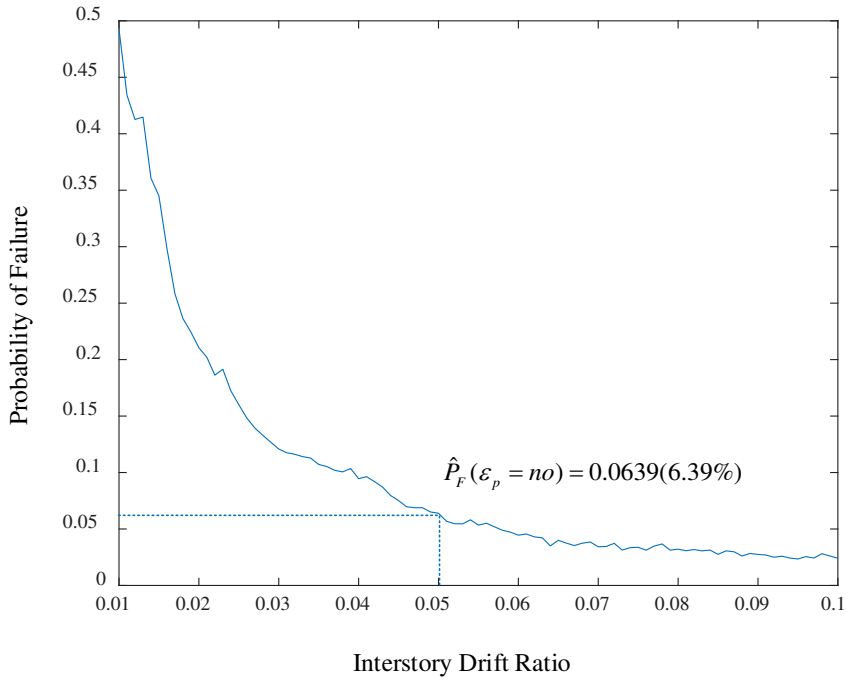

Figure 24 Failure probability for no pulse in ground motion against interstory drift ratio thresholds for Chevron Braced Frame

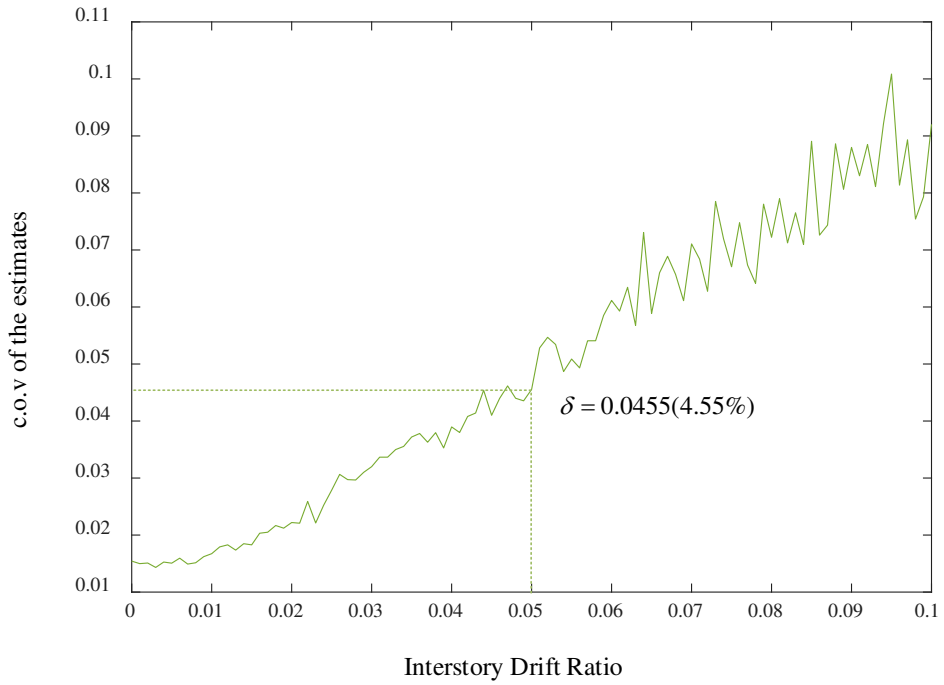

Figure 25 c.o.v of the failure probability for no pulse ground motion against interstory drift ratio thresholds for Chevron Braced Frame

The failure probability when different performance thresholds are used is also plotted and shown in Figure 24 while Figure 25 shows the corresponding c.o.v for the estimates. More specifically, when the performance threshold (maximum interstory drift ratio) is set at different damage state such as 0.004 for 'slight damage', 0.008 for 'moderate damage' and 0.025 for 'extensive damage' the corresponding failure probability is $P(F_{\text{slight}}) = 75.45\%$ with c.o.v of the estimate as 12%, $P(F_{\text{moderate}}) = 64.30\%$ with c.o.v of the estimate as 9.66% and $P(F_{\text{extensive}}) = 20.72\%$ with c.o.v of the estimate as 9.27% respectively. Similarly the failure probability is also evaluated for the case when there is no pulse in the ground motion. The corresponding failure probability is $P(F_{\text{slight}} \mid \varepsilon_p = no) = 68.82\%$ with the c.o.v of the estimate as 1.53%, $P(F_{\text{moderate}} \mid \varepsilon_p = no) = 56.55\%$ with c.o.v of the estimate as 1.51% and

$P(F_{\text{extensive}} \mid \varepsilon_p = no) = 16\%$ with the c.o.v of the estimate as 2.79% respectively. Table 8 below presents the failure probability under probabilistic pulse and no pulse ground motion for different definition of failure (corresponding to different damage state) for Chevron Braced Frame.

Table 8 Failure probability of Chevron Braced Frame at different damage states

(Damage State)	**Failure Probability** $P(F \mid \varepsilon_p = yes, no)$	**Failure Probability** $P(F \mid \varepsilon_p = no)$
'Slight'	75.45%	68.82%
'Moderate'	64.30%	56.55%
'Extensive'	20.72%	16%
'Collapse'	8.87%	6.39%

As can be seen from Table 8, for the case where there is no near-fault pulse in the ground motion, the corresponding failure probabilities for all the different level of damage states are much smaller. This shows the importance of the near-fault pulse and how it can significantly increase the probability of failure in the structure. When no near-fault pulse is considered, apparently the corresponding seismic (collapse) risk will be significantly underestimated. Therefore, for more accurate seismic risk assessment, it is important to accurately and properly characterize the near-fault pulses that might exist in near-fault ground motions. Additionally, due to the small failure probability, the estimates have relatively large c.o.v. This is expected and corresponds to the challenges associated with simulation of rare events where typically large numbers of simulations are needed to get an accurate estimate of the corresponding failure probability.

Comparing the value of $P(\varepsilon_p = no)$=95.17% and value of $P(\varepsilon_p = no \mid F)$=68.47%, or equivalently, $P(\varepsilon_p = yes)$=4.83% and $P(\varepsilon_p = yes \mid F)$=31.53%, we can clearly see that in the samples or ground motions that caused failure, the percentage of ground motions that have near-

fault pulse is 31.53%, which corresponds to significant increase compared to the percentage of ground motions that have near-fault pulse based on the prior distribution (which is only 4.83%). This further highlights that the occurrence of collapse failure in the considered Chevron Braced Frame is highly correlated to the existence of near-fault pulse.

6.2.2 Cross Bracing Braced Frame

Similarly, the failure probability $\hat{P}_F$ for Cross Bracing Braced Frame is calculated, and it turns out to be 13.93% with c.o.v of the estimate as 8.38%. As previously mentioned c.o.v is an indication of the accuracy of the estimate (for the seismic risk), typically c.o.v of 10% or less implies a good estimation. For this case the seismic collapse risk is relatively high. This can be due to the fact the distance between the frame and the earthquake fault is close which resulted in the structure experiencing strong ground motion compared to structures that are situated far away from the earthquake fault. (e.g., these structures would only experience far field earthquake ground motion). In addition, the variation of failure probability when different interstory drift ratio thresholds are used is plotted in Figure 26. As expected, the failure probability decreases as the threshold increases. Also the c.o.v of the corresponding estimates is plotted against the threshold in Figure 27. Overall, the failure probabilities are estimated with relatively good accuracy (e.g., with c.o.v below or around 10%).

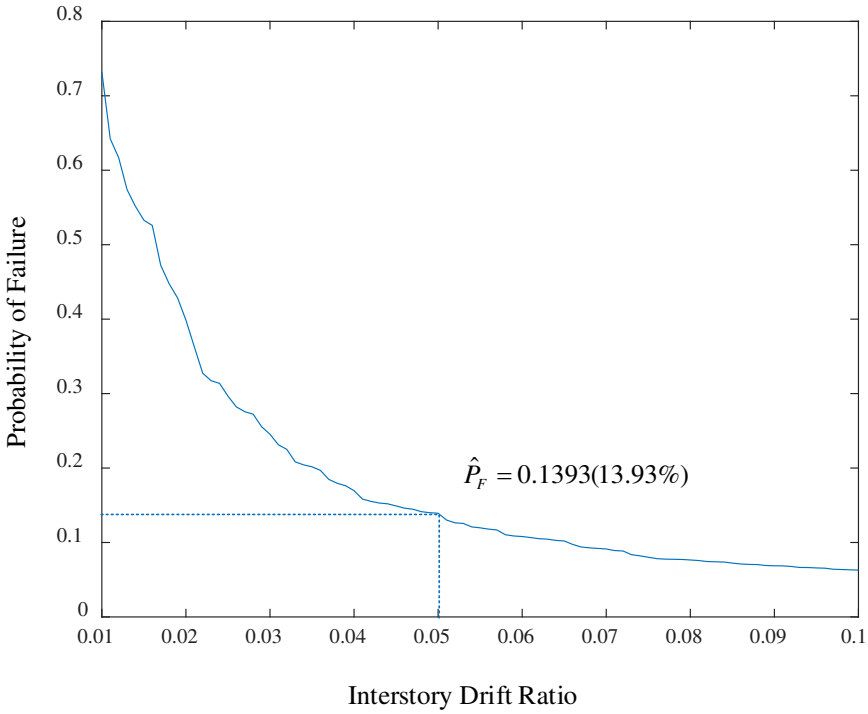

Figure 26 Failure probability against interstory drift ratio thresholds for Cross Bracing Braced Frame

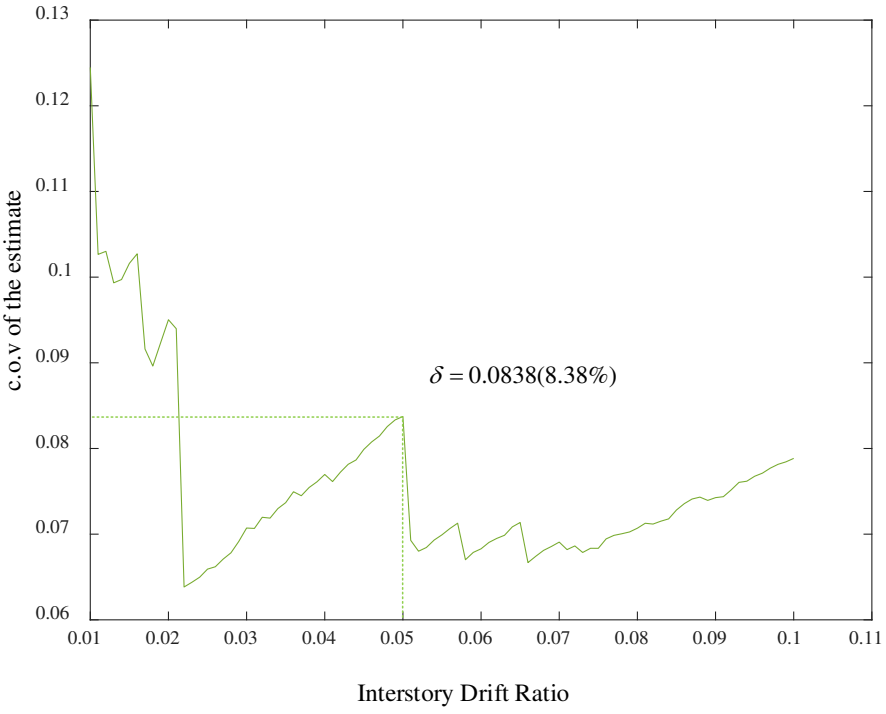

Figure 27 c.o.v of the failure probability estimates against interstory drift ratio thresholds for Cross Bracing Braced Frame

In order to investigate the impact of including or not the near-fault pulse in the stochastic ground motion of the seismic collapse risk of the Cross Bracing Braced Frame, the seismic collapse risk when there is no near-fault pulse in the stochastic ground motion is also evaluated. With the help of Eq.(6.8), it is achieved without the need to run additional simulations. By using Eq. (6.9) $P(\varepsilon_p = no \mid F)$ is estimated to be 75.3% with c.o.v of the estimate as 3.16% which is evaluated using Eq.(6.12). Now using Eq. (6.10), $P(\varepsilon_p = no)$ is estimated to be 95.17%. Therefore, the failure probability of frame at no pulse $P(F \mid \varepsilon_p = no)$ is estimated to be 11.06% with the c.o.v of the estimate as 3.16%. Now comparing this with the failure probability of the frame when there is near-fault pulse in the ground motion is 13.93% and the seismic collapse risk of the Cross Bracing Braced Frame is much smaller (i.e. at 11.06%) when there is no near-fault pulse in the stochastic ground motion. This analysis highlights the significance of the near-fault pulse on the seismic collapse risk estimation of the Cross Bracing Braced Frame.

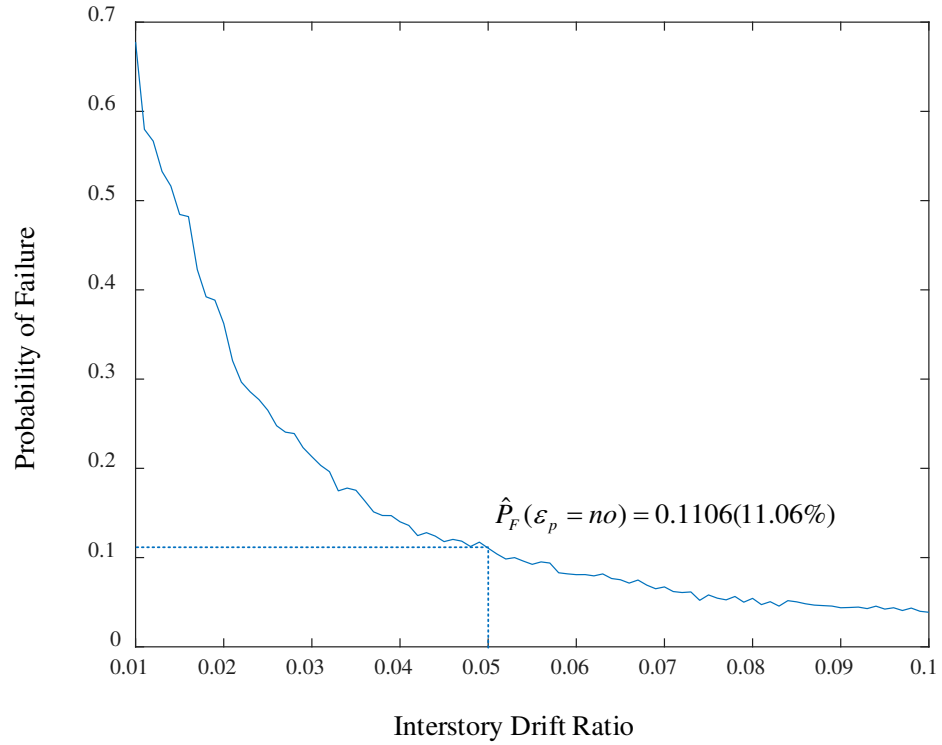

Figure 28 Failure probability for no pulse ground motion against interstory drift ratio thresholds for Cross Bracing Braced Frame

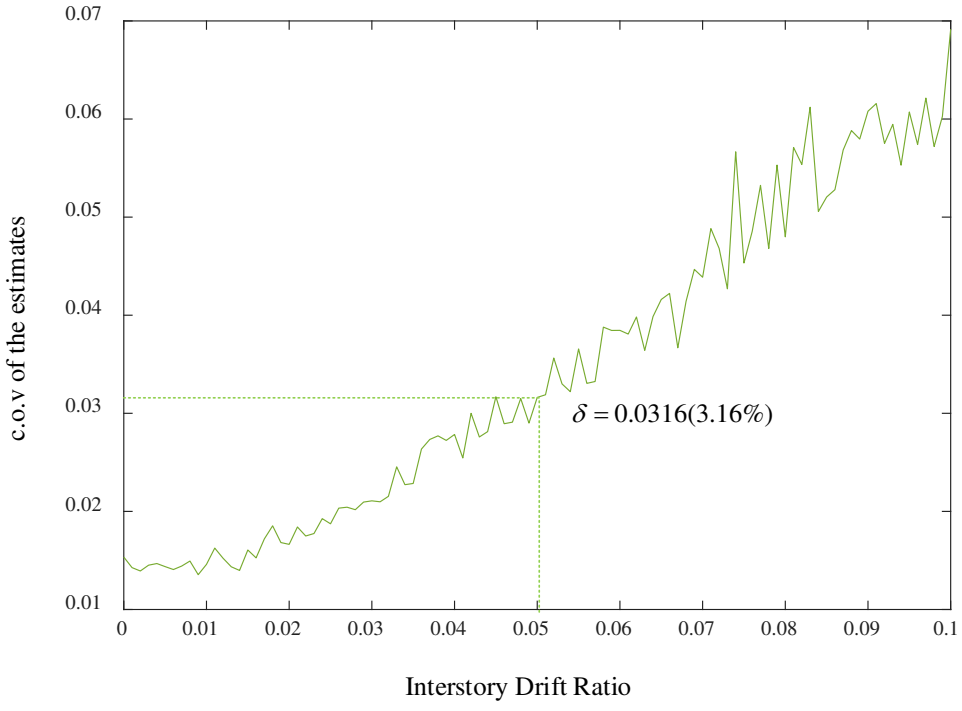

Figure 29 c.o.v of the failure probability estimates for no pulse ground motion against interstory drift ratio thresholds for Cross Bracing Braced Frame

The failure probability when different performance thresholds when there is no near-fault pulse in the ground motions are used is also plotted and shown in Figure 28 while Figure 29 shows the corresponding c.o.v for the estimates. For this braced frame, the failure probability corresponding to different performance thresholds are also calculated. So for slight damage state the corresponding failure probability is $P(F_{\text{slight}}) = 98.95\%$ with c.o.v of the estimate as 39.81%, for moderate damage state the corresponding failure probability is $P(F_{\text{moderate}}) = 78.51\%$ with c.o.v of the estimate as 12.07% and finally for the extensive damage state the failure probability is $P(F_{\text{extensive}}) = 31.37\%$ with c.o.v of the estimate as 6.5%. The failure probability under different threshold is evaluated again for the ground motion with no pulse and for slight damage state, the failure probability is $P(F_{\text{slight}} \mid \varepsilon_p = no) = 92.41\%$ with c.o.v of the estimate as 1.47%, for moderate damage state, the failure probability is $P(F_{\text{moderate}} \mid \varepsilon_p = no) = 70.17\%$ with c.o.v of the estimate as 1.49% and for the extensive damage state, the failure probability is $P(F_{\text{extensive}} \mid \varepsilon_p = no) = 26.51\%$ with c.o.v of the estimate as 1.87%. The lower c.o.v values of the estimates indicate accurate estimates.

Table 9 Failure Probability of Cross Bracing Braced Frame at different damage states

(Damage State)	Failure Probability $P(F \mid \varepsilon_p = yes, no)$	Failure Probability $P(F \mid \varepsilon_p = no)$
'Slight'	98.95%	92.41%
'Moderate'	78.51%	70.17%
'Extensive'	31.37%	26.51%
'Collapse'	13.93%	11.06%

It can be observed from Table 9, for different damage states the failure probability of the structure is higher when the ground motion has near-fault pulse in it while for the same damage states the failure probability is lower when there is no near-fault pulse in the ground motion. This

shows the importance of the near-fault pulse and how it can significantly increase the probability of failure in the structure. Also when there is no near-fault pulse is considered, apparently the corresponding seismic collapse risk will be significantly underestimated. So in order to achieve more accurate seismic risk assessment, it is crucial to accurately characterize the near-fault pulse that might exist in near-fault ground motions. Additionally, due to the small failure probability, the estimates have relatively large c.o.v. This is expected and corresponds to the challenges associated with simulation of rare events where typically large numbers of simulations are needed to get an accurate estimate of the corresponding failure probability.

Comparing the value of $P(\varepsilon_p = no)$=94.85% and value of $P(\varepsilon_p = no \mid F)$=75.30%, or equivalently, $P(\varepsilon_p = yes)$=5.15% and $P(\varepsilon_p = yes \mid F)$=24.7%, we can clearly see that in the samples or ground motions that caused failure, the percentage of ground motions that have near-fault pulse is 24.7%, which corresponds to significant increase compared to the percentage of ground motions that have near-fault pulse based on the prior distribution (which is only 5.15%). This further highlights that the occurrence of collapse failure in the considered Cross Bracing Braced Frame is highly correlated to the existence of near-fault pulse.

6.2.3 Comparison between Two Braced Frames

Comparing the results for the two braced frames, it can be seen that the Cross Bracing Braced Frame has much higher probability of failure for both the case of considering probabilistic near-fault pulse in the ground motions and the case of not considering near-fault pulse in the ground motions. The seismic collapse risk of Chevron Braced Frame is around 8.87%, while the value for Cross Bracing Braced Frame is around 13.93%. The corresponding risks when not considering near-fault pulse are 6.39% and 11.06%, respectively. The higher

seismic collapse risk for the Cross Bracing Braced Frame aligns with our observations in Section 4.3.3 when comparing the pushover analysis results for these two braced frames. For the pushover analysis, it was observed that after the braces buckle/yield for the Cross Bracing Braced Frame, it did not have any ultimate strength; therefore, the overall stiffness of the system decreased with the lateral displacement as opposed to Chevron Braced Frame. This behavior conforms to the general braced frame behavior where braces act as the primary component for resisting the lateral forces generated due to seismic action. For the Chevron Braced Frame the introduction of the zipper columns can also be enhancing the overall stiffness of the system.

6.2.4 Uncertainty in Seismic Collapse Threshold

The above seismic collapse risk assessment uses 5% interstory drift ratio as the collapse threshold. The occurrence of collapse may depend on many factor and the collapse threshold/limit may be different depending on numerous reasons such as type of lateral load resisting system, height of the structure, site location and many more. To investigate how the variability or uncertainty in the collapse threshold/limit on the seismic collapse risk, the seismic collapse risk for both frames considering uncertain collapse threshold is also calculated. For this purpose, the collapse threshold is assumed to follow a lognormal distribution with median of 5% and 30% c.o.v. To calculate the corresponding seismic collapse risk, the same set of simulations is used; the only change is instead of comparing each sample interstory drift ratio with the 5% threshold, each sample interstory drift ratio is compared with a sample for the collapse threshold generated from the lognormal distribution with median of 5% and 30% c.o.v. In the end, the failure probability for Chevron Braced Frame is calculated to be 9.44% with c.o.v of 7.46%; for Cross Bracing Braced Frame, the failure probability is 14.52% with c.o.v of 8.38%. Compared

to the case with deterministic collapse threshold, the seismic collapse risk for both frames slightly increased (e.g., from 8.87% to 9.44% for Chevron Braced Frame, and 13.93% to 14.52% for Cross Bracing Braced Frame).

6.3 Probabilistic Sensitivity Analysis Results

After the calculation for the failure probability for both frames, a probabilistic sensitivity analysis is carried out to quantify the importance of uncertain model parameters in the stochastic near-fault ground motion towards the seismic collapse risk. The calculation details for the relative entropy values for both continuous variables and discrete variable have been discussed in Section 6.1.4. Note that the same set of simulations are used to generate the failure samples from the failure distribution and no additional simulations were used to establish the relative entropy values for all the uncertain model parameters in the stochastic ground motion model. Additionally, the importance of the pulse existence parameter ε_p is also calculated using Eq. (6.14). The relative entropy results for some of the important parameters in the SGM that had a significant impact in seismic collapse risk are presented for both Chevron Braced Frame and Cross Bracing Braced Frame.

6.3.1 Chevron Braced Frame

The relative entropy values are reported in Table 10. Two general cases are considered. The first case corresponds to when there is probabilistic near-fault pulse in the stochastic ground motion (i.e., the existence of pulse has a certain probability, which is calculated based on Eq.(5.5)). This case is denoted as $\varepsilon_p = \{yes, no\}$. The second case corresponds to when there is no near-fault pulse (i.e., only considering the high-frequency components in the stochastic

ground motion). This case is denoted as $\varepsilon_p = \{no\}$. For the second case, essentially the model parameters in the stochastic ground motions will not have any of those parameters that are related to the pulse characteristics. For both cases, only some of the important parameters for the corresponding case are presented. In addition to individual parameters, relative entropy is also evaluated for some groups of parameters to investigate the joint effects of these parameters.

Qualitatively, if there is large discrepancy between the failure distribution $p(\theta_i \mid F)$ and the prior distribution $p(\theta_i)$, it means θ_i has higher importance. Figure 30 shows the histogram or samples from the prior and failure distributions for M, f_a and f_b for the ground motion with probabilistic pulse. As can be seen, for both parameters, there are large difference between the failure distribution and prior distribution, indicating higher sensitivity and higher contribution towards the seismic collapse risk.

In terms of relative entropy values, for the $\varepsilon_p = \{yes, no\}$ case, it is evident that the Moment magnitude M dominates the risk with the rupture distance r having much smaller influence. The group parameter $[M, r]$ had the highest importance in seismic collapse risk. The higher importance of these parameters are expected since they are the primary seismological parameters that affects seismic risk, followed by the upper and lower frequencies of the high frequency components in the ground motion f_a & f_b. Also, the pulse existence parameter ε_p has high sensitivity values, demonstrating the importance of near-fault pulses on the seismic collapse risk. It can also be noted that the primary pulse characteristics (e.g., pulse period T_p , pulse amplitude A_p) had a significant influence on the seismic collapse risk. The higher relative entropy values for T_p is expected considering its direct dependence on the Moment magnitude

M (see Eq. (5.4)). Overall, the pulse characteristics are shown to be crucial in seismic risk assessment and should be included as discussed in Section 2.3.

For the case $\varepsilon_p = \{no\}$, since there is no near-fault pulse, all parameters related to pulse are not considered. For this case, as expected, the moment magnitude and rupture distance are the important parameters. As also seen from Figure 31, when looking at seismic collapse risk it is expected that large moment magnitude earthquakes would more likely to cause failure/collapse, hence the shift of the distribution towards large moment magnitudes, leading to large difference between failure distribution and the prior distribution.

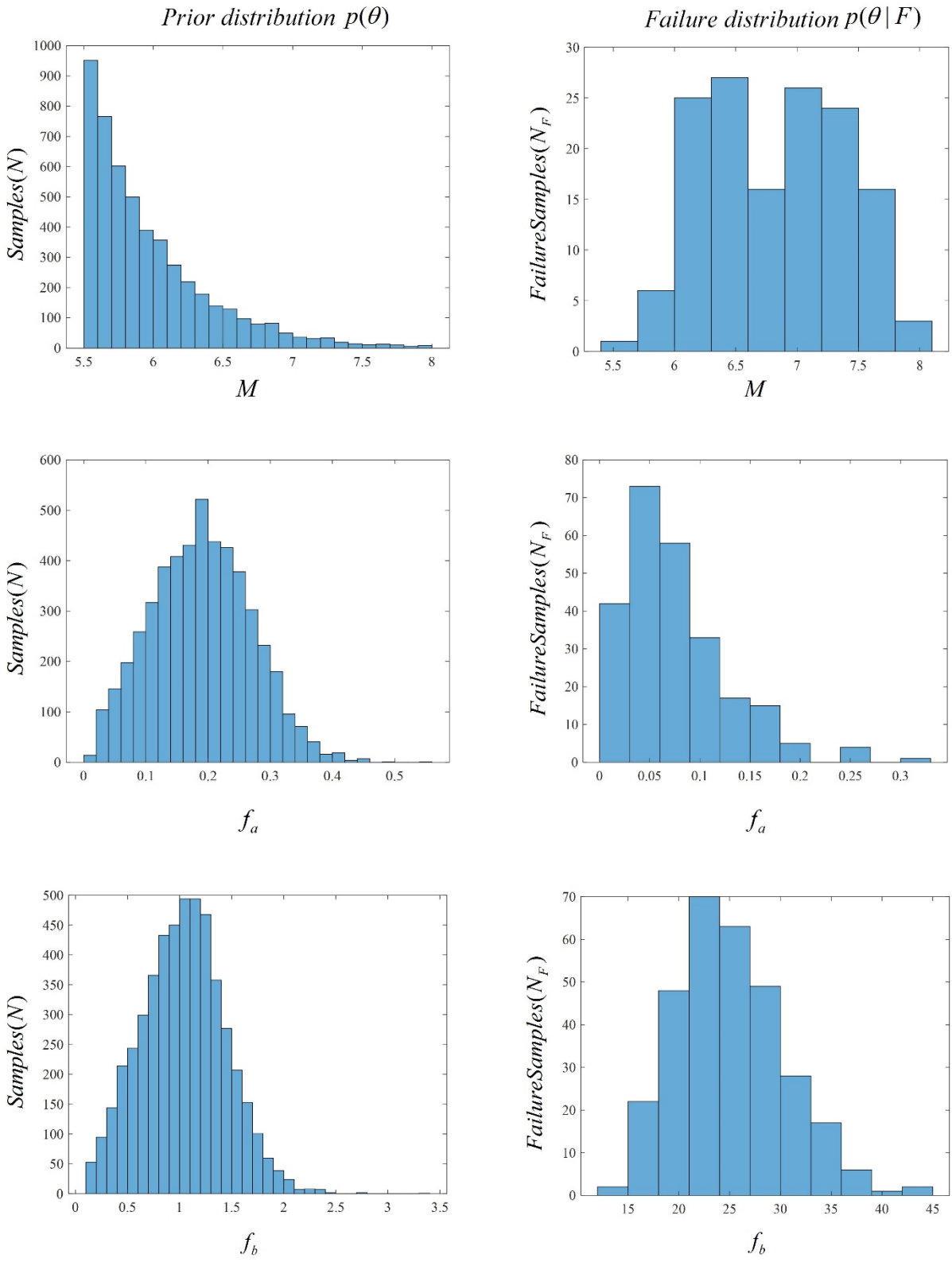

Figure 30 Prior and failure distribution of M, f_a and f_b for Chevron Braced Frame under probabilistic pulse ground motion

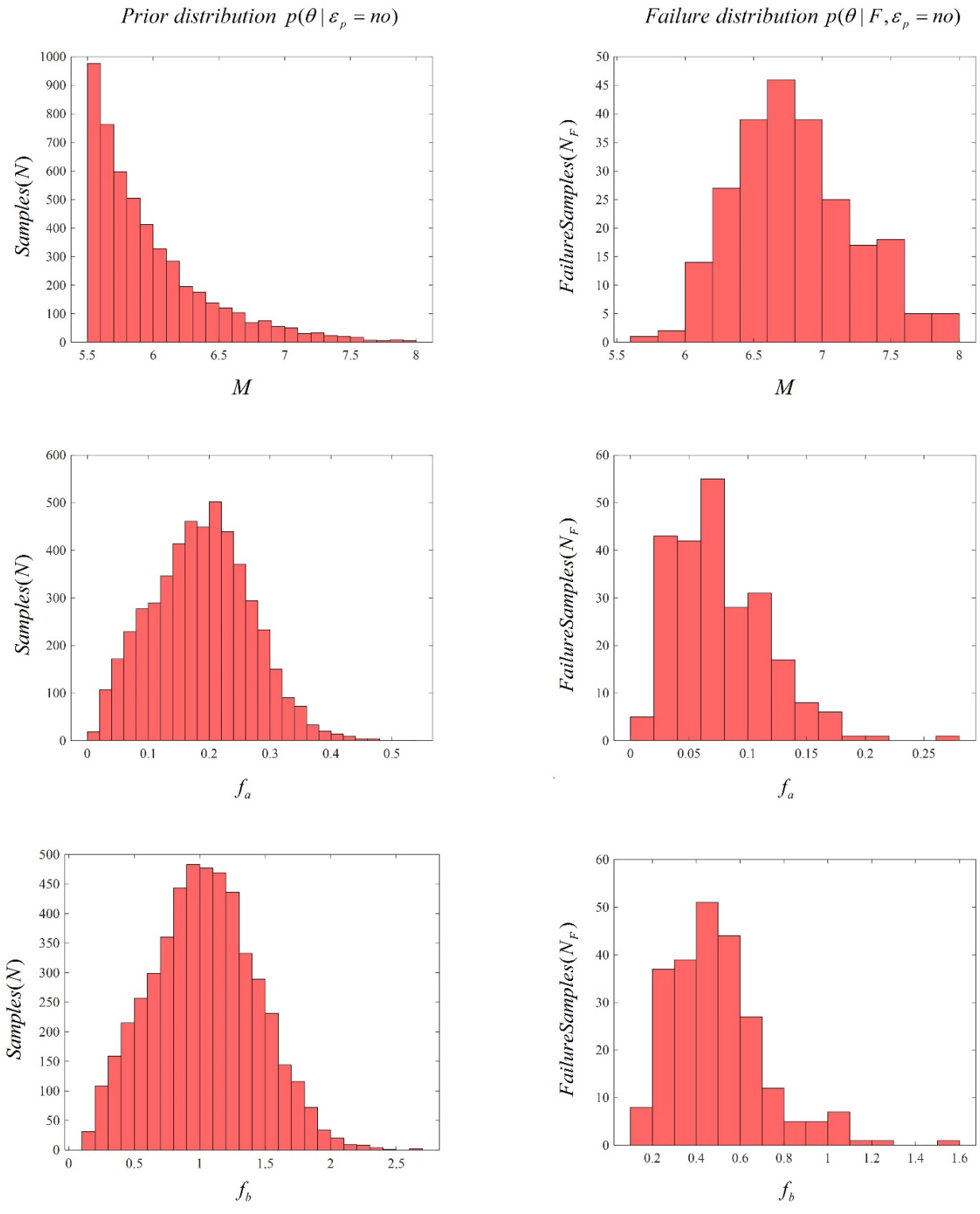

Figure 31 Prior and failure distribution of M, f_a and f_b for Chevron Braced Frame under no pulse ground motion

Table 10 Sensitivity analysis results for ground motion with probabilistic pulse and no pulse for Chevron Braced Frame

Model Parameters	Relative Entropy ($\varepsilon_p = \{yes, no\}$)	Model Parameters	Relative Entropy ($\varepsilon_p = \{no\}$)
ε_p	0.9486		
M	1.3838	M	1.7234
f_a	1.2187	f_a	1.4520
f_b	1.1390	f_b	1.3120
T_p	1.0659	$L_{rupture}$	1.1125
$L_{rupture}$	0.9379	e	1.0948
e	0.9232	e_b	0.0315
A_p	0.6539	$e_{L_{rupture}}$	0.0304
r	0.0441	$f_{\max}$	0.0223
e_b	0.0215	e_e	0.0203
$f_{\max}$	0.0146	λ_t	0.0042
θ_p	0.0140	η_t	0.0029
$e_{L_{rupture}}$	0.0104	κ_o	0.0024
e_e	0.0102	$[M, r]$	1.9665
λ_t	0.0089		
κ_o	0.0079		
e_{A_p}	0.0073		
γ_p	0.0051		
e_{T_p}	0.0046		
η_t	0.0029		
$[M, r]$	1.5508		
$[M, e_{T_p}]$	1.3915		
$[M, T_p]$	1.0926		
$[r, A_p]$	0.6774		
$[r, e_{A_p}]$	0.06		

To facilitate a more in-depth understanding of the sensitivity analysis results, Figure 32 shows the samples for primary seismic hazard characteristics M and r from the joint PDF

$p(M, r \mid F)$. In Figure 31 the $p(M, r \mid F, \varepsilon_p = yes)$, $p(M, r \mid F, \varepsilon_p = no)$, and $p(M, r \mid F)$ provide a great insight on understanding the importance of the seismic characteristics. For $p(M, r \mid F, \varepsilon_p = yes)$ it can be observed that even with low seismic moment magnitude, the existence of pulse can lead to collapse in the structure if the distance between site and fault is low. This again confirms the importance of forward directivity pulse for seismic collapse risk assessment and should not be ignored when designing the structure close to fault regions. On the other hand, for $p(M, r \mid F, \varepsilon_p = no)$, large number of failure samples have high values of Moment magnitude M and these failure occurred even when the rupture distance r is large which implies the importance of Moment magnitude M in affecting the seismic risk, which is expected.

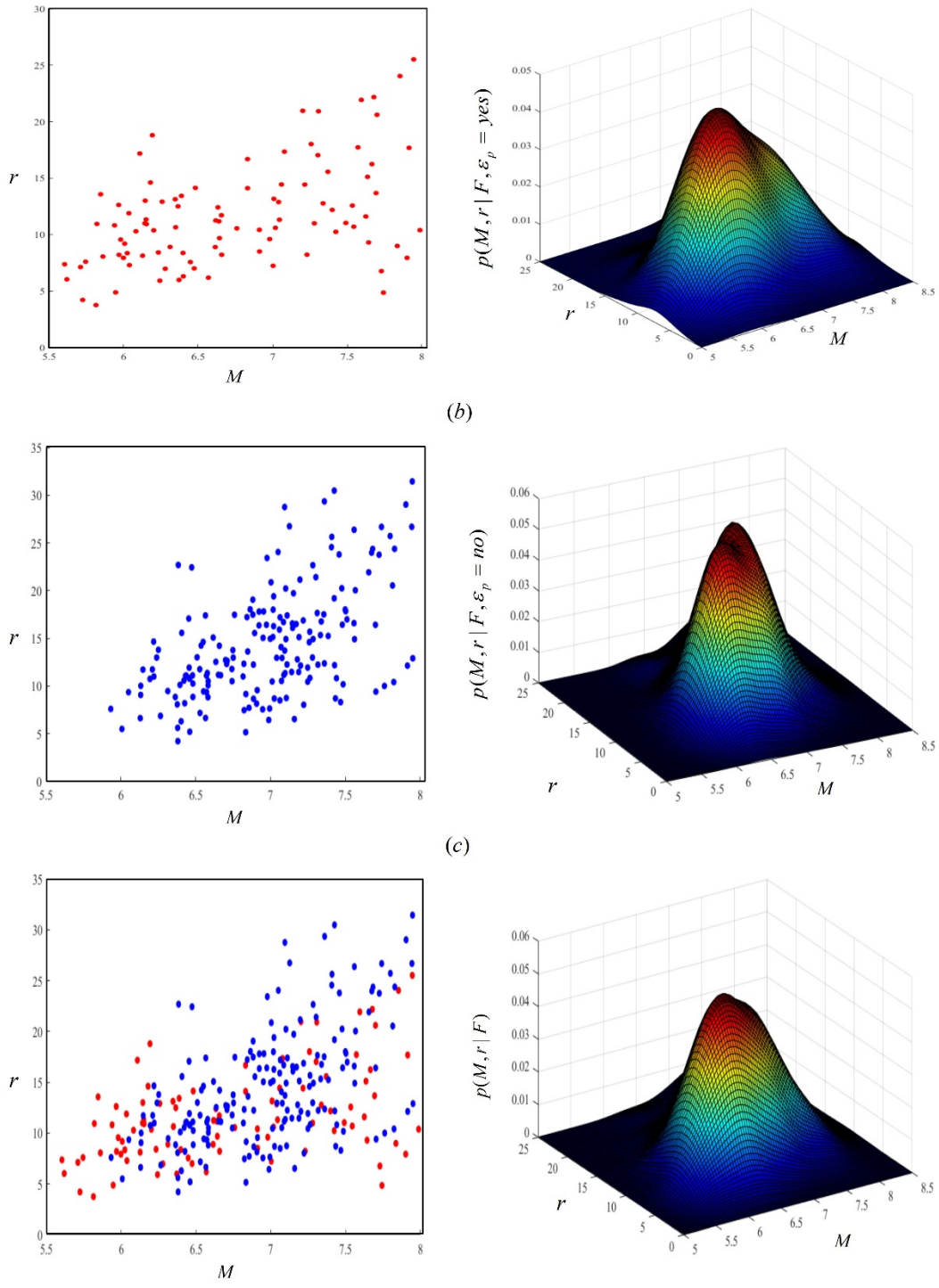

Figure 32 Samples from $p(M, r \mid F)$ (left column) for (a) $\varepsilon_p = yes$ (b) $\varepsilon_p = no$ (c) all failure samples and their probability distribution estimated using KDE (right column) for Chevron Braced Frame

6.3.2 Cross Bracing Braced Frame

Similarly the sensitivity analysis is carried out for the Cross Bracing Braced Frames and the important uncertain parameter are presented in Table 11. For the ground motion with probabilistic pulse $\varepsilon_p = \{yes, no\}$, the sensitivity results are similar to the Chevron Braced Frame. Here, the existence of pulse ε_p has the highest importance in the seismic collapse risk for the Cross Bracing Braced Frame, this demonstrates the importance of near-fault pulses on the seismic collapse risk. Other than this, similar trends are observed to the ones for Chevron Braced Frame. Overall, the pulse characteristics are shown to be crucial in seismic risk assessment.

Similarly, the relative entropy for ground motion with no pulse $\varepsilon_p = \{no\}$ is shown in Table 11. For this case, as expected, the moment magnitude and rupture distance are the important parameters. As also seen from Figure 33 which is similar to the distribution plotted in the previous section 6.3.1, when looking at seismic collapse risk it is expected that large moment magnitude earthquakes would more likely to cause failure/collapse, hence the shift of the distribution towards large moment magnitudes, leading to large difference between failure distribution and the prior distribution.

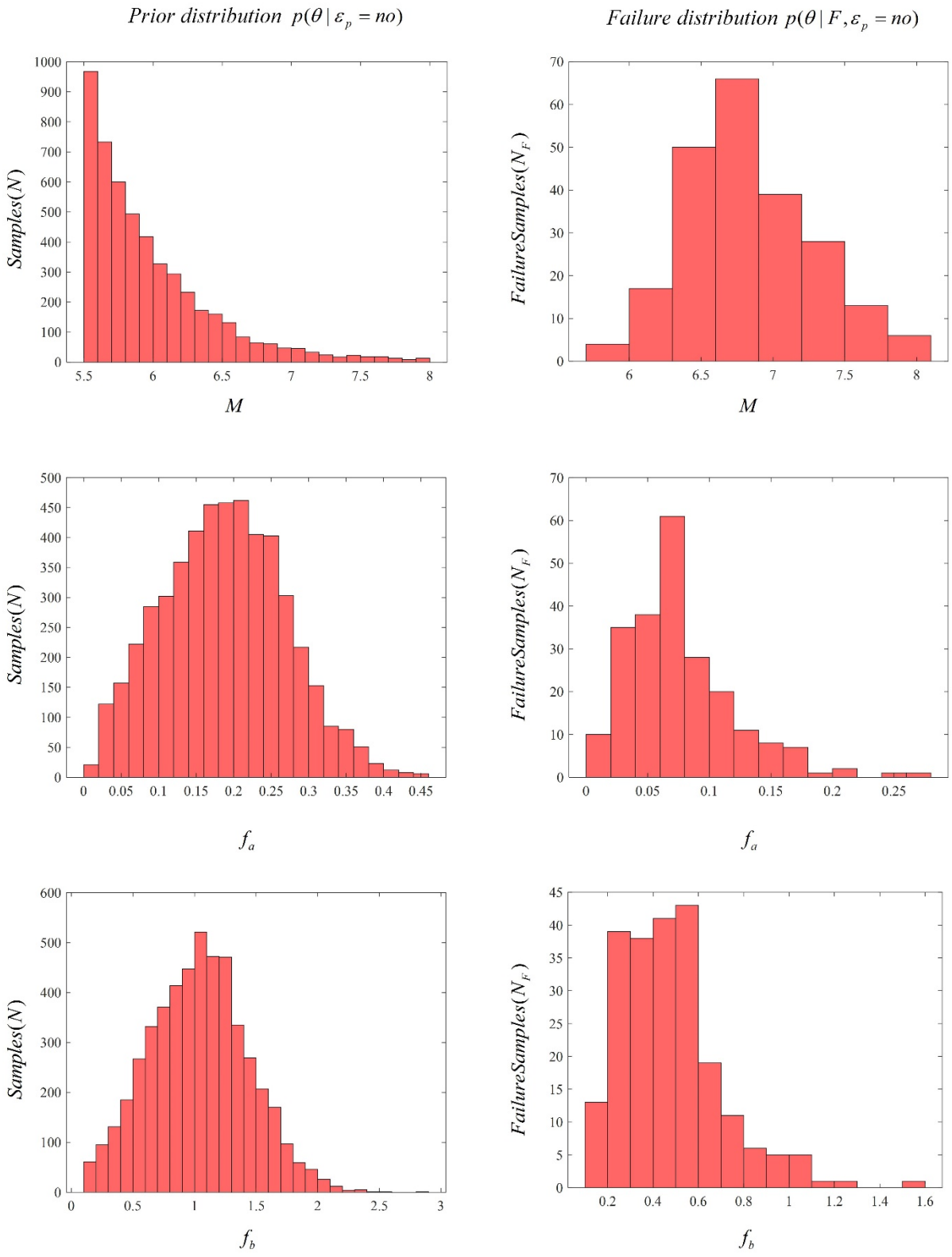

Figure 33 Prior and failure distribution of M, f_a and f_b for Cross Bracing Braced Frame under no pulse ground motion

Table 11 Sensitivity analysis results for ground motion with probabilistic pulse and no pulse for Cross Bracing Braced Frame

Model Parameters	Relative Entropy ($\varepsilon_p = \{yes, no\}$)	Model Parameters	Relative Entropy ($\varepsilon_p = \{no\}$)
ε_p	0.9435		
M	1.1959	M	1.3648
f_b	1.0086	f_a	1.1335
f_a	0.9949	f_b	1.0968
$L_{rupture}$	0.8244	$L_{rupture}$	0.9894
T_p	0.8227	e	0.8841
e	0.8069	e_b	0.0419
A_p	0.5845	r	0.0383
r	0.0346	κ_o	0.0243
e_{A_p}	0.0270	$e_{L_{rupture}}$	0.0207
e_{T_p}	0.0213	γ_p	0.0206
η_t	0.0210	θ_p	0.0172
γ_p	0.0207	λ_t	0.0089
κ_o	0.0187	η_t	0.0049
e_b	0.0161	e_e	0.0047
$f_{\max}$	0.0107	$f_{\max}$	0.0038
θ_p	0.0085	$[M, r]$	1.5300
e_e	0.0054		
$e_{L_{rupture}}$	0.0045		
λ_t	0.0024		
$[M, r]$	1.3650		
$[M, e_{T_p}]$	1.2043		
$[M, T_p]$	0.9299		
$[r, A_p]$	0.6365		
$[r, e_{A_p}]$	0.0817		

To facilitate a more in-depth understanding of the sensitivity analysis results, Figure 34 shows the samples for primary seismic hazard characteristics M and r from the joint PDF

$p(M, r \mid F)$. Similar trends to those for Chevron Braced Frame are observed for the Crossed Bracing Braced Frame. For $p(M, r \mid F, \varepsilon_p = yes)$ it can be observed that even with low seismic moment magnitude, the existence of pulse can lead to collapse in the structure if the distance between site and fault is low. This again confirms the importance of forward directivity pulse for seismic collapse risk assessment and should not be ignored when designing the structure close to fault regions. On the other hand, for $p(M, r \mid F, \varepsilon_p = no)$, large number of failure samples have high values of Moment magnitude M and these failure occurred even when the rupture distance r is large which implies the importance of Moment magnitude M in affecting the seismic risk, which is expected.

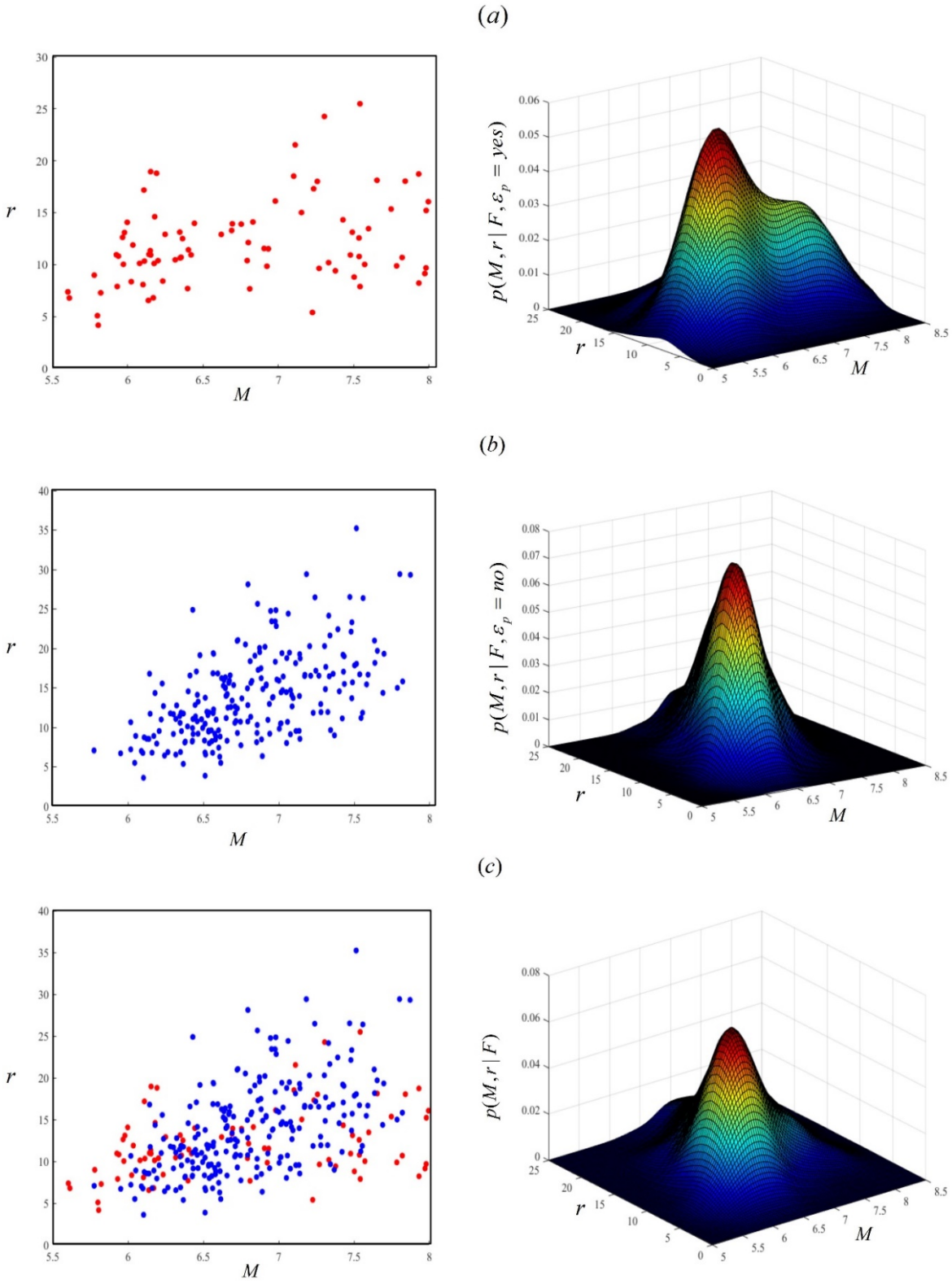

Figure 34 Samples from $p(M,r \mid F)$ (left column) for (a) $\varepsilon_p = yes$ (b) $\varepsilon_p = no$ (c) all failure samples and their probability distribution estimated using KDE (right column) for Cross Bracing Braced Frame

6.4 Deflected Shape of the Braced Frames

In this section the deflected shape of the Chevron Braced Frame and the Cross Bracing Braced frame is plotted to understand the behavior of the braces. For each frame, the responses under ground motions with and without near-fault pulse and the corresponding deflected shapes of the frame at several time instances are plotted.

6.4.1 Chevron Braced Frame

For the ground motion with near-fault pulse, a ground motion with Moment magnitude of 6.55 is selected, and the deflected shape is plotted at 6 different time instances (a) 2.63s, (b) 9.65s, (c) 15.31s, (d) 23.01, (e) 27.03s and (f) 34.95s. Figure 35 plots the time history for the ground motion. As can be seen, there is a large near-fault pulse at around 3s. The interstory drift ratio exceeded the threshold after the structure is exposed to this near-fault pulse, which shows the importance of pulse characteristics in ground motion on the seismic collapse of Chevron Braced Frame. For the ground motion with no near-fault pulse, a ground motion with Moment magnitude of 7.6 is selected. The deflected shape is again plotted at 6 different time instances (a) 7.02s, (b) 10.74s, (c) 13.16s, (d) 20.46s, (e) 26.78s and (f) 34.00s in Figure 36.

One interesting observation can be made for the deflected shape is that, the braces in the 1st and 2nd Floor yielded and buckled the most under ground motion. The interstory drift ratios for these floors were significantly higher as compared to that for the 3rd Floor. Additionally, under both pulse and no pulse ground motions the interstory drift ratio for the 3rd Floor is really small and there is negligible bending of the beams in the 3rd Floor. This can be due to the introduction of zipper column in the braced frame. These zipper columns help in suppressing roof's soft story mechanisms by distrusting the forces to the 2nd and 1st Floor respectively. This

analysis proves the mechanisms of the zipper columns and how they assist in making the Chevron braced frame into a really strong lateral load resisting system.

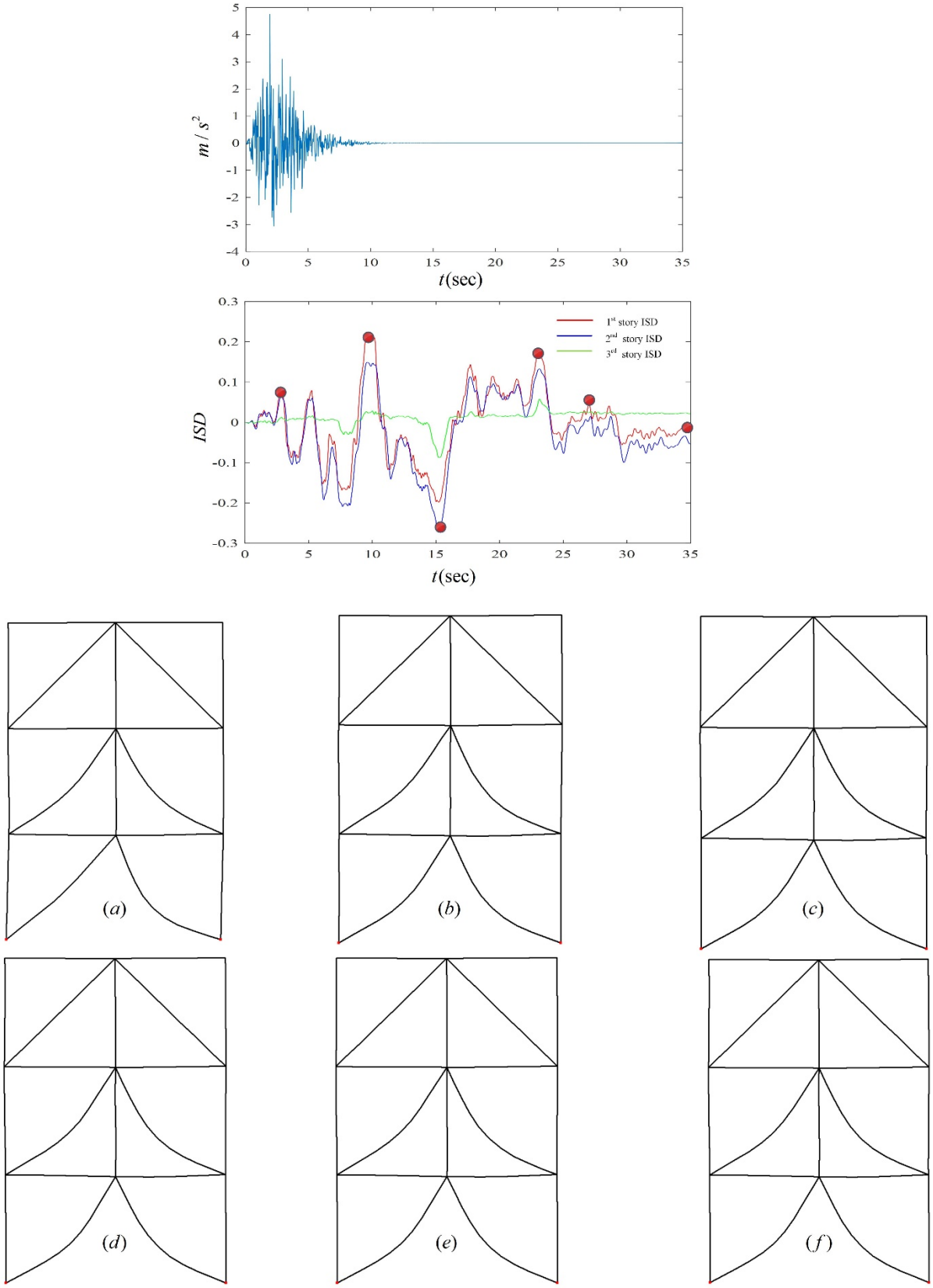

Figure 35 Deflected shape under ground motion with near-fault pulse for Chevron Braced Frame

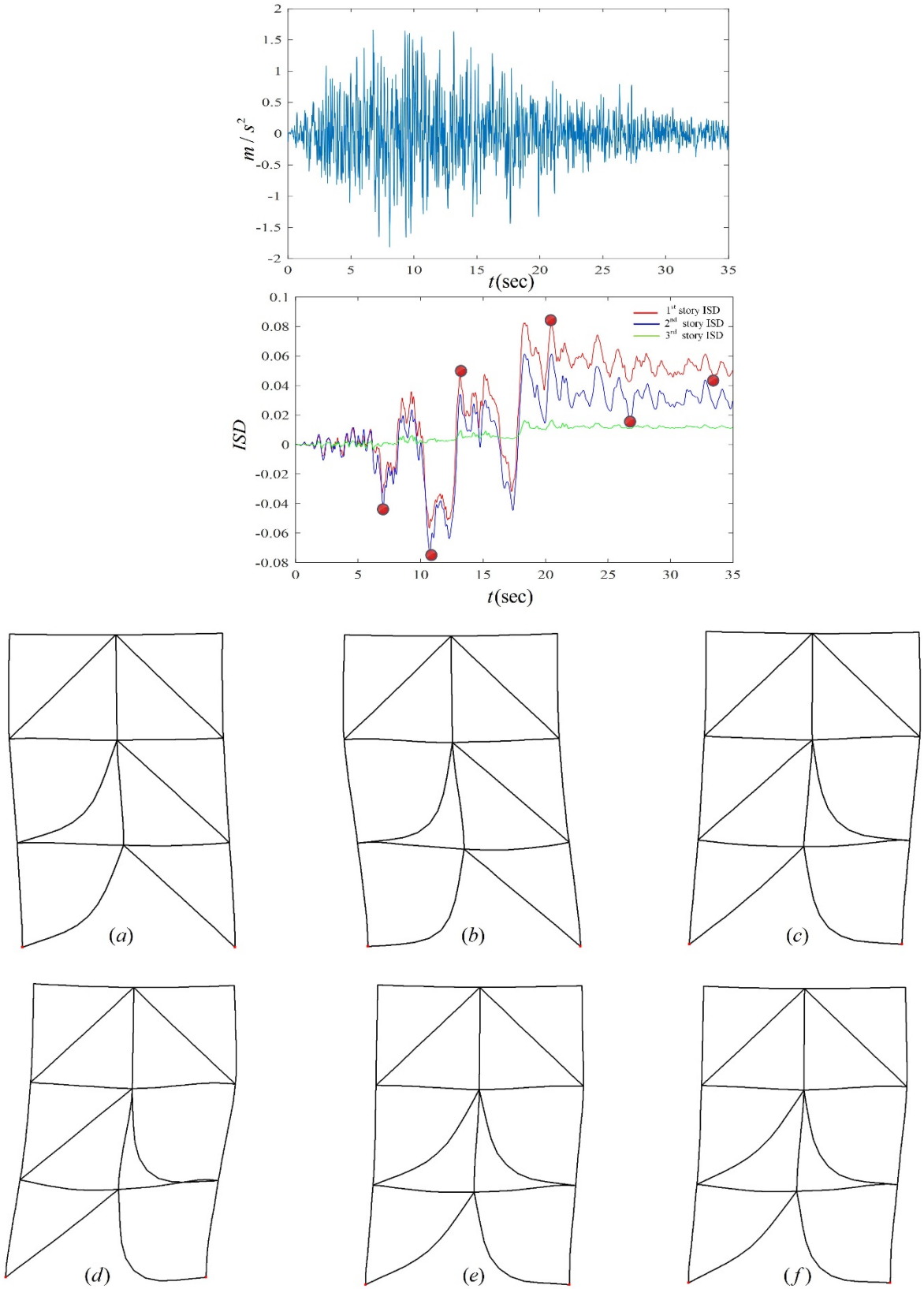

Figure 36 Deflected shape under ground motion with no near-fault pulse for Chevron Braced Frame

6.4.2 Cross Bracing Braced Frame

The deflected shape of Cross bracing braced frame is also plotted here to understand the behavior of the system. Initially the ground motion with the probabilistic pulse is plotted at 6 different time instances (a) 6.42s, (b) 7.89s, (c) 12.34s, (d) 13.5s, (e) 28.8s and (f) 33.34s. The Figure 37 describes the ground motion with interstory drift ratio for each floor with the deflected shape the above time instances. Similarly, deflected shape of this braced frame under no probabilistic pulse is also plotted at time instances (a) 9.99s, (b) 11.3s, (c) 15.79s, (d) 20.46s, (e) 26.35s in Figure 38.

It can be observed from the interstory drift ratio that unlike Chevron braced frame, this frame has similar interstory drift ratios for all the floors. Also, the interstory drift ratio in 3rd Floor is higher as compared to the interstory drift ratio for rest of the floors for both pulse and no pulse ground motions. This led to the prominent brace buckling and yielding on the 3rd Floor.

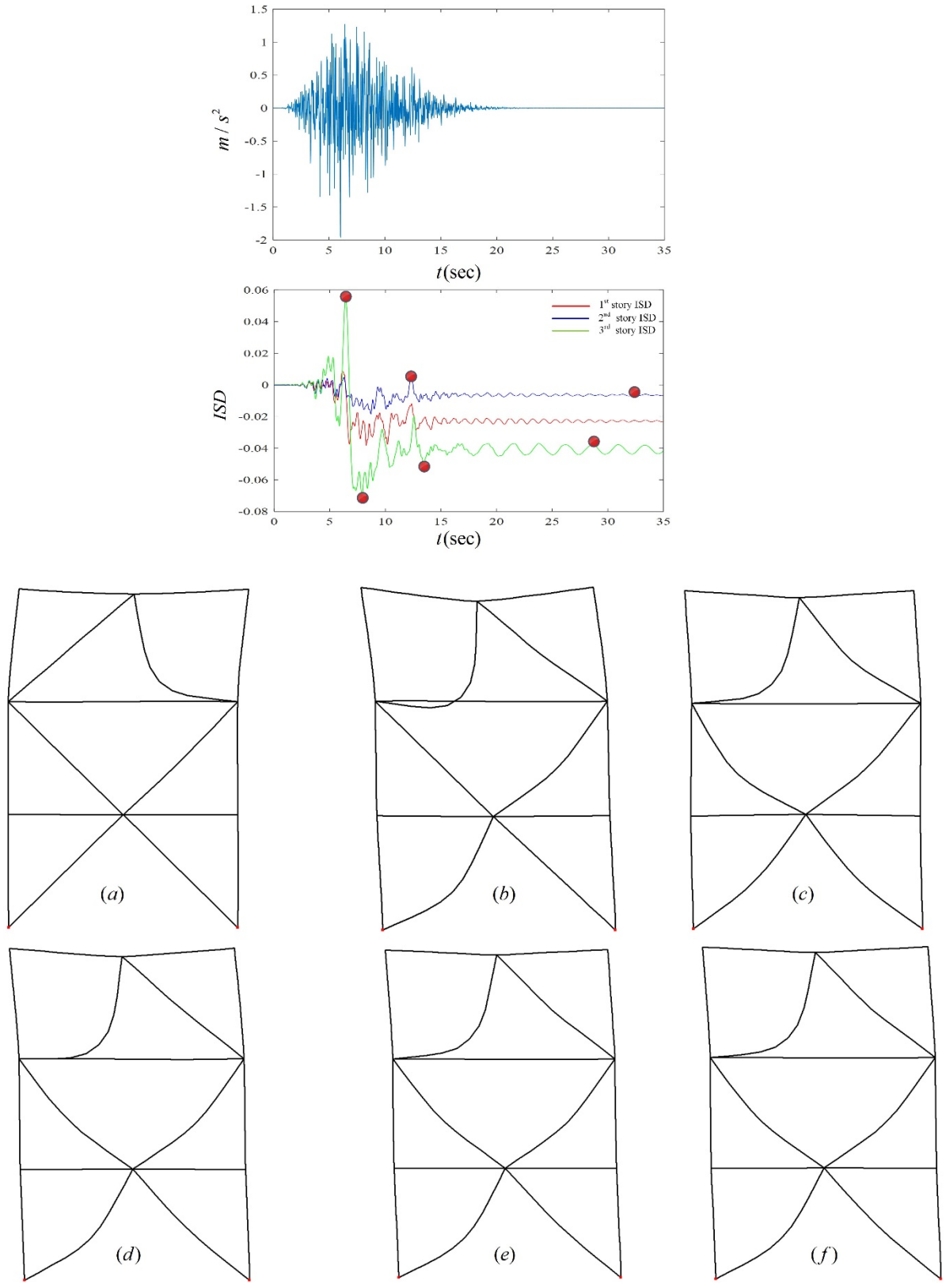

Figure 37 Deflected shape under ground motion with near-fault pulse for Cross Bracing Braced Frame

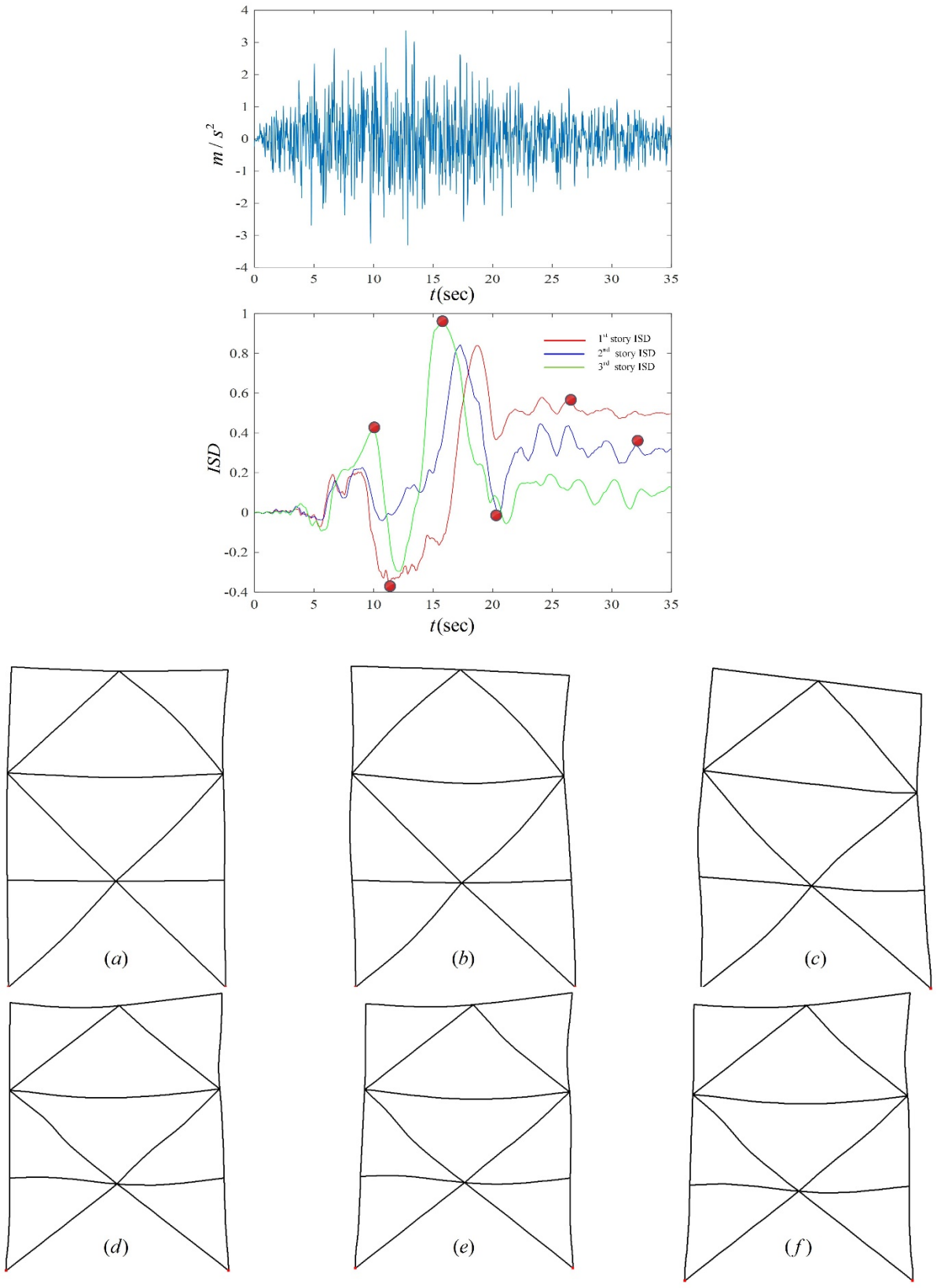

Figure 38 Deflected shape under ground motion with no near-fault pulse for Cross Bracing Braced Frame

CHAPTER 7:CONCLUSION AND FUTURE RECOMMENDATIONS

7.1 Conclusion

The overall study was carried out to understand the significance of the near-fault pulse on the seismic collapse risk of SCBFs close to earthquake faults. The modern seismic codes often ignored the pulse characteristics when assessing the seismic collapse risk of structures in these regions. To properly include the near-fault pulse characteristic in the earthquake excitation, a near-fault stochastic ground motion model was used. The uncertainties associated with ground motion parameters and the pulse characteristics were described by using probability density functions. A simulation based approach was adopted to propagate the uncertainties in the ground motion and estimate the seismic collapse risk (the failure probability) of the SCBFs. Efficient sample-based approach was adopted to estimate the probabilistic sensitivity measure called relative entropy to evaluate the important of the uncertainty in each of the model parameters (including those related to the near-fault pulse characteristics) in contributing towards the seismic collapse risk. Two braced frames, Chevron Braced Frame and Cross Bracing Braced Frame, were investigated. The results showed that for both frames the seismic collapse risks were significantly higher when the near-fault pulse was included in the ground motion compared to the cases when no near-fault pulses were considered. When neglecting the near-fault pulses, the seismic risk will be significantly underestimated. The sensitivity results showed that the moment magnitude and the existence of near-fault pulse as well as the amplitude and period of the near-fault pulses were the most important parameters affecting the overall seismic collapse risks for both frames. Even for some earthquakes with small moment magnitude, the near-fault pulse (with potentially large amplitude) could be present, which could potentially lead to much

higher structural responses. Comparing the results for both frames in this study, it was found that the Chevron Braced Frame had lower seismic collapse risk than the Cross Bracing Braced Frame, and Chevron Braced Frame seemed to be a better choice when trying to reduce the seismic collapse risk. Overall, the results highlighted the importance of incorporating near-fault pulse in the ground motion for accurate estimation of seismic (collapse) risk and also for risk-informed design of structures located close to earthquake faults.

7.2 Limitation

It is important to keep in mind that this study investigates specific frames with adoption of specific models for stochastic ground motion and assumption of prior probability models/distributions for the model parameters (in the seismic hazard and stochastic ground motion model). To generalize the results to other cases, some additional considerations and investigations are needed. More specifically,

1) The results that are presented in this study are based on given selection of prior distributions of the seismicity characteristics and the earthquake fault associated with the site (i.e., strike-slip fault). For different selection of prior distributions, results will change accordingly for the seismic collapse risk as well as the difference between considering near-fault pulse or not.
2) The results are for three story braced frames with fundamental periods around 0.7s. For the failure samples with near-fault pulse, a histogram of these samples are plotted for the ratio of the period of the near-fault pulse and the fundamental period of the structure, which is shown in Figure 39 for both frames. As can be seen, most of the ratios are larger than 1. Therefore, it is expected that for taller frames with higher

fundamental periods, the near-fault pulse might lead to even higher seismic collapse risk and the difference between considering near-fault pulse or not might be even higher.

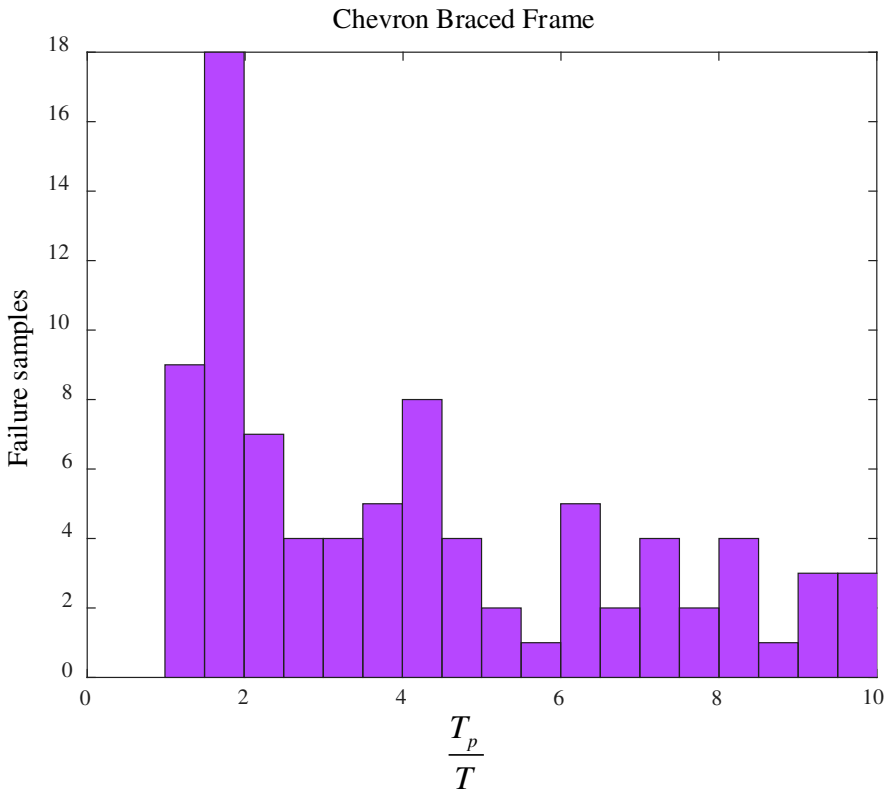

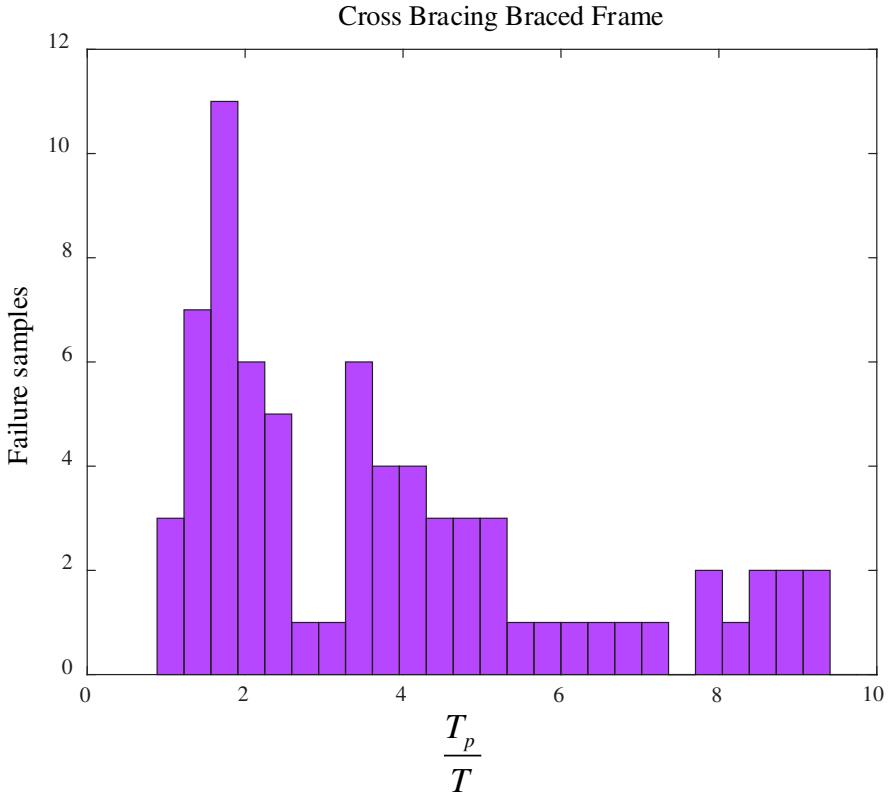

Figure 39 Failure samples for ratio of pulse period and fundamental period of structure

7.3 Future Scope

Some of the key recommendations that can be utilized for future research work is mentioned below.

1) More accurate and physics-based models for near-fault ground motions. In this study, it was found that near-fault pulses in ground motions could have significant impact on the seismic (collapse) risk assessment. Better models (e.g., physics-based models calibrated with recorded near-fault ground motion database) for stochastic near-fault grout motion can help with more accurate prediction of seismic (collapse) risk of braced frames and other structures.
2) Impact of near-fault pulse other structures. In this study, the impact of near-fault pulse on seismic collapse risk of two types of braced frames was investigated. It is expected that the existence of near-fault pulse will also have large impacts on other structures, especially for those with longer periods considering that the near-fault pulse typically has long periods. Also, the ratio of the pulse period and structure period may have important impacts on the structural performances under near-fault ground motions.
3) Study the impact of near-fault ground motion on risk-informed structural design.

REFERENCES

[1] Federal Emergency Management Association (FEMA). NextGeneration Performance-Based Seismic Design Guidelines. 2006.

[2] Arnold C. Design guide for improving school safety in earthquakes, floods, and high winds. Risk Manag Ser 2010:1–16.

[3] ATC-40. Seismic Evaluation and Retrofit of Concrete Buildings. Earthq Spectra 1996;16:241–61.

[4] Reaveley LD, Shapiro D, Moehle J, Atkinson T, Rojahn C, Holmes W. Guidelines and Commentary for the Seismic Rehabilitation of Buildings. 1997.

[5] ASCE- American Society of Civil Engineers. Prestandard and Commentary for the Seismic Rehabilitation of Buildings. 2000.

[6] Applied Technology Council. Improvement of Nonlinear Static Seismic Analysis Procedures. 2009.

[7] FEMA 547. Techniques for the Seismic Rehabilitation of Existing Buildings. Fema 547 2006:571.

[8] Chen C, Mahin S. A Performance-based seismic demand assessment of concentrically braced steel frame buildings 2012.

[9] Sabelli R, Roeder CW, Hajjar JF. Seismic Design of Steel Special Concentrically Braced Frame Systems- A Guide for Practicing Engineers. NEHRP Seism Des Tech Br 2013:1–36.

[10] Liel AB, Haselton CB, Deierlein GG. Seismic Collapse Safety of Reinforced Concrete Buildings. II: Comparative Assessment of Nonductile and Ductile Moment Frames. J

Struct Eng 2011;137:492–502.

[11] Han SW, Foutch D. Behavior of hollow structural section bracing members with different w/t ratios 2005:39–44.

[12] Astaneh-Asl A, Goel SC, R.D. H. Cyclic behavior of double angle bracing members with bolted connections 1990:249-256.

[13] AISC. AISC 360-05 Specifications for Structural Steel Buildings. 2005.

[14] AISC. Seismic provisions for structural steel buildings 1997.

[15] Uriz P, Mahin S a. Toward Earthquake-Resistant Design of Concentrically Braced Steel-Frame Structures. 2008.

[16] Roeder CW, Lumpkin EJ, Lehman DE. A balanced design procedure for special concentrically braced frame connections. J Constr Steel Res 2011;67:1760–72.

[17] Hsiao P. Seismic Performance Evaluation of Concentrically Braced Frames 2012:1–270.

[18] Palmer KD. Seismic Behavior, Performance and Design of Steel Concentrically Braced Frame Systems. University of Washington, 2012.

[19] Iervolino I, Cornell CA. Probability of occurrence of velocity pulses in near-source ground motions. Bull Seismol Soc Am 2008;98:2262–77.

[20] Dabaghi M, Rezaeian S, Der Kiureghian A. Stochastic simulation of near-fault ground motions for specified earthquake and site characteristics. Appl Stat Probab Civ Eng 2011:2498–505.

[21] Menun Charles, Fu Q. An analytical model for near-fault ground motions and the response of SDOF systems 2002.

[22] Wu SL, Bhuddarak C, Junji K. Synthesis of near-fault ground motion using a hybrid method of stochastic and theoretical green's functions 2016.

[23] Mavroeidis G, Papageorgiou A. A mathematical representation of near-fault ground motions. Bull Seismol 2003;93:1099–131.

[24] Vafaei D, Shemshadian ME, Zahrai SM. Seismic behavior of BRB Frames under near fault excitations. 9th US Natl 10th Can Conf Earthq Eng 2010, Incl Pap from 4th Int Tsunami Symp 2010;8:6041–51.

[25] Alavi B, Krawinkler H. Strengthening of moment-resisting frame structures against near-fault ground motion effects. Earthq Eng Struct Dyn 2004;33:707–22.

[26] Ibarra LF, Krawinkler H. Global Collapse of Frame Structures under Seismic Excitations. 2005.

[27] Vamvatsikos D, Cornell CA. The incremental dynamic analysis and its application to performance-based earthquake engineering. Proc 12th Eur Conf Earthq Eng 2002:10.

[28] Admuthe SA. Semi-Rigid Steel Frames Subjected To mainshock-aftershock earthquake sequences. Colorado State University,Fort Collins, 2018.

[29] Taflanidis AA, Jia G. A simulation-based framework for risk assessment and probabilistic sensitivity analysis of base-isolated structures. Earthq Engng Struct Dyn 2011;40:1629–51.

[30] Papageorgiou BYAS, Aki K. A specific barrier model for the quantitative description of inhomogeneous faulting and the prediction of strong ground motion. J Geol 2009;21:288–288.

[31] Au SK, Beck JL. Subset Simulation and its Application to Seismic Risk Based on Dynamic Analysis. J Eng Mech 2003;129:901–17.

[32] Taflanidis AA, Beck JL. Life-cycle cost optimal design of passive dissipative devices. Struct Saf 2009;31:508–22.

[33] Kim H, Robert CP, Casella G. Monte Carlo Statistical Methods. vol. 42. 2006.

[34] Jia G, Taflanidis AA. Sample-based evaluation of global probabilistic sensitivity measures. Comput Struct 2014;144:103–18.

[35] Taflanidis AA, Beck JL. Stochastic Subset Optimization for optimal reliability problems. Probabilistic Eng Mech 2008;23:324–38.

[36] Taflanidis AA, Loukogeorgaki E, Angelides DC. Offshore wind turbine risk quantification/evaluation under extreme environmental conditions. Reliab Eng Syst Saf 2013;115:19–32.

[37] Vetter C, Taflanidis AA. Global sensitivity analysis for stochastic ground motion modeling in seismic-risk assessment. Soil Dyn Earthq Eng 2012;38:128–43.

[38] Beirlant J, Dudewicz EJ, Györfi L, Van Der Meulen EC. Nonparametric entropy estimation: an overview. Int J Math Stat Sci 1997;6:17–39.

[39] Scott DW, Sain SR. Multi-dimensional Density Estimation David. EdAcUk 2017;9983459:1–39.

[40] Taflanidis AA, Jia G. A simulation-based framework for risk assessment and probabilistic sensitivity analysis of base-isolated structures. Earthq Engng Struct Dyn 2011:1629–51.

[41] Taflanidis AA, Beck JL. Stochastic Subset Optimization for reliability optimization and sensitivity analysis in system design. Comput Struct 2009;87:318–31.

[42] Krawlinkler H, SAC Joint Venture SACJ, Venture SACJ, et al. State of the Art Report on Systems Performance of Steel Moment Frames Subject to Eearthquake Ground Shaking n.d.

[43] Rafn Gunnarsson I. Numerical Performance Evaluation of Braced Frame Systems. 2004.

[44] Bruneau Michel, Uang C-M, Sabelli R. Ductile Design of Steel Structures , 2nd edition.

2014.

[45] Leon RT, Yang C-S. Special inverted-v-braced frames with suspended zipper struts. Int Work Steel Concr Compos Constr Taipei Natl Cent Res Earthq 2003:89–96.

[46] Elnashai AS, Papanikolaou V, Lee DH. ZEUS-NL User Manual 2005:147.

[47] Terzic V. PACIFIC EARTHQUAKE ENGINEERING Modeling SCB frames using beam-column elements. OpenSees Webiner 2013.

[48] Kilar V, Fajfar P. Simple push-over analysis of asymmetric buildings. Earthq Eng Struct Dyn 1997;26:233–49.

[49] Sarand NI, Danesh A. Evaluation of Seismic Behavior of Concentrically Braced Frames with Zipper Columns 2015;10:374–80.

[50] Jia G, Gidaris I, Taflanidis AA, Mavroeidis GP. Reliability-based assessment/design of floor isolation systems. Eng Struct 2014;78:41–56.

[51] Atkinson GM, Silva W. Stochastic modeling of California ground motions. Bull Seismol Soc Am 2000;90:255–74.

[52] Atkinson GM. Ground-motion prediction equations for Eastern North America from a referenced empirical approach: Implications for epistemic uncertainty. Bull Seismol Soc Am 2008;98:1304–18.

[53] Vetter C, Taflanidis AA. Comparison of alternative stochastic ground motion models for seismic risk characterization. Soil Dyn Earthq Eng 2014;58:48–65.

[54] Vetter C, Taflanidis AA. Global sensitivity analysis for stochastic ground motion modeling in seismic-risk assessment. Soil Dyn Earthq Eng 2012;38:128–43.

[55] Boore DM. Simulation of Ground Motion Using the Stochastic Method. Pure Appl Geophys 2003;160:635–76.

[56] Bray JD, Rodriguez-Marek A. Characterization of forward-directivity ground motions in the near-fault region. Soil Dyn Earthq Eng 2004;24:815–28.

[57] Halldórsson B, Mavroeidis GP, Papageorgiou AS. Near-Fault and Far-Field Strong Ground-Motion Simulation for Earthquake Engineering Applications Using the Specific Barrier Model. J Struct Eng 2010;137:433–44.

[58] Mihailo DT, Maria IT, Miodrag IM, Variability of the fixed-base and soil-structure system frequencies of a building-The case of Borik-2 building. Struct Control Heal Monit 2008;61:215–23.

[59] Shahi SK, Baker JW. An empirically calibrated framework for including the effects of near-fault directivity in probabilistic seismic hazard analysis. Bull Seismol Soc Am 2011;101:742–55.

[60] Wells DL, Coppersmith KJKJ. Empirical relationships among magnitude, rupture length, rupture width, rupture area and surface displacements. Bull Seismol Soc Am 1994;84:974–1002.

APPENDIX A: POINT SOURCE MODEL

The stochastic ground motion model described in CHAPTER 5: corresponds to the two corner point source model developed by Atkinson and Silva [51] and it is created by taking into account the physics of the fault rupture of the structural location as well as the propagation of the seismic wave from the fault to the site. These models consists of total spectrum $A(f;M,r)$ which depends upon the earthquake magnitude M and the rupture distance r, it is expressed as a function of frequency f and the variation of ground motions is expressed through an envelope function $e(t;M,r)$ which also depends upon the same parameter as the total spectrum. These frequency and time domain completely represents the ground motion characteristics in such a way that it can be easily associated with the seismic hazard [55].

Total Spectrum

The total spectrum $A(f;M,r)$ for the acceleration time history can be expressed as the product of source $E(f)$, path $P(f)$ and the site $G(f)$.

$$A(f;M,r) = (2\pi f)^2 E(f)P(f)G(f) \tag{A.1}$$

These components ultimately depends upon the uncertain model parameters θ_q, here only the functional dependence of frequency f and time envelope $e(t)$ is described here in detail. The source spectrum can be expressed through the following mathematical equation

$$E(f) = CM_w \left[\frac{1-e}{1+\left(f/f_a\right)^2} + \frac{e}{1+\left(f/f_b\right)^2} \right] \tag{A.2}$$

where M_w is the seismic moment (expressed in dyn-cm) related with moment magnitude through a relationship $log_{10}M_w = 1.5(M + 10.7)$, where the constant C is $C = 10^{-20} R_\Phi VF / (4\pi R_o \rho_s \beta_s^3)$, where R_Φ is radiation pattern , $V = 1/(2)^{1/2}$ represents the partition of total shear-wave velocity into the horizontal components, *F*=2 is the free surface amplification $\rho_s = 2.8 g/cm^3$ and $\beta_s = 3.5 km/s$ are the density and shear-wave velocity in the vicinity of the source R_o is a reference distance set at 1km and f_a, f_b were the lower and upper frequencies with e as weighting parameter that follows the equation.

$$\log_{10} f_a = 2.181 - 0.496M \tag{A.3}$$

$$\log_{10} f_b = 2.41 - 0.408M \tag{A.4}$$

$$\log_{10} e = 0.605 - 0.255M \tag{A.5}$$

Now similarly the path effect $P(f)$ can be modelled by multiplying the geometrical spreading and the elastic attenuation [55].

$$P(f) = Z(R_r)\exp\left[-\pi f R_r / (Q(f) c_Q)\right] \tag{A.6}$$

where $Q(f) = 180 f^{0.45}$ is a regional attenuation function, c_Q is the seismic wave velocity to calculate the $Q(f)$, $Z(R_r)$ is the geometrical spreading function and $R_r = \left[h_d^{\,2} + r^2\right]^{1/2}$ is the radial distance from the earthquake source to the site, with

$$\log_{10} h_d = 0.15 - 0.05M \tag{A.7}$$

which representing a moment dependent, nominal “pseudo-depth”[51] and *r* corresponds to the closest distance to rupture.

At last the site parameter $G(f)$ is quantified by multiplying the high frequency diminution $D(f)$ and an amplification factor $A_m(f)$, this diminution can be represented through $\mathbb{k}_o$ filter or the f_{max} filter.

$$D(f) = \exp(-\pi\kappa_o f)\left[1+\left(f / f_{max}\right)^8\right]^{-1/2} \tag{A.8}$$

Time Envelope

The temporal characteristics of the earthquake ground motion can be defined using a time domain envelope function from [55] and is expressed as

$$e(t) = a_t \left(t / t_n\right)^{b_t} \exp\left(-c_t (t / t_n)\right) \tag{A.9}$$

where a_t, b_t, c_t are selected such that $e(t)$ has a peak equal to unity when $t = \lambda_t t_n$, and $e(t) = \eta_t$ when $t = t_n$, and these parameters can be quantified using the equation below

$$a_t = [\exp(1) / \lambda_t]^{b_t} \tag{A.10}$$

$$b_t = -\lambda_t \ln(\eta_t) / [1 + (\ln(\lambda_t) - 1)] \tag{A.11}$$

$$c_t = b_t / \lambda_t \tag{A.12}$$

The time duration parameter t_n is defined by $t_n = 2T_w$, where T_w is the duration of strong ground motion expressed as a sum of a path dependent and a source dependent component, it can be expressed mathematically as [55]

$$T_w = \frac{1}{2f_a} + 0.05R_r \tag{A.13}$$

Stochastic Ground Motion Model

The stochastic ground motion can be generated by modulating the white noise sequence $Z = [Z_w(it) : i = 1, 2, 3....., N_t]$ first by the time envelope function $e(t)$ and then by amplitude spectrum $A(f)$. The steps below provide a brief outline how ground motion is generated.

i) The white noise sequence Z is multiplied by the envelope function $e(t)$.

ii) Now this resultant sequence is then transformed to the frequency domain.

iii) It is then again normalized by the square root of the mean square of the total spectrum.

iv) The normalized sequence is multiplied by the total spectrum $A(f)$

v) At last it is transformed back to the time domain to obtain the desired acceleration time history.

Figure 40 below illustrates the whole process of simulating stochastic ground motion acceleration time histories [3][5].

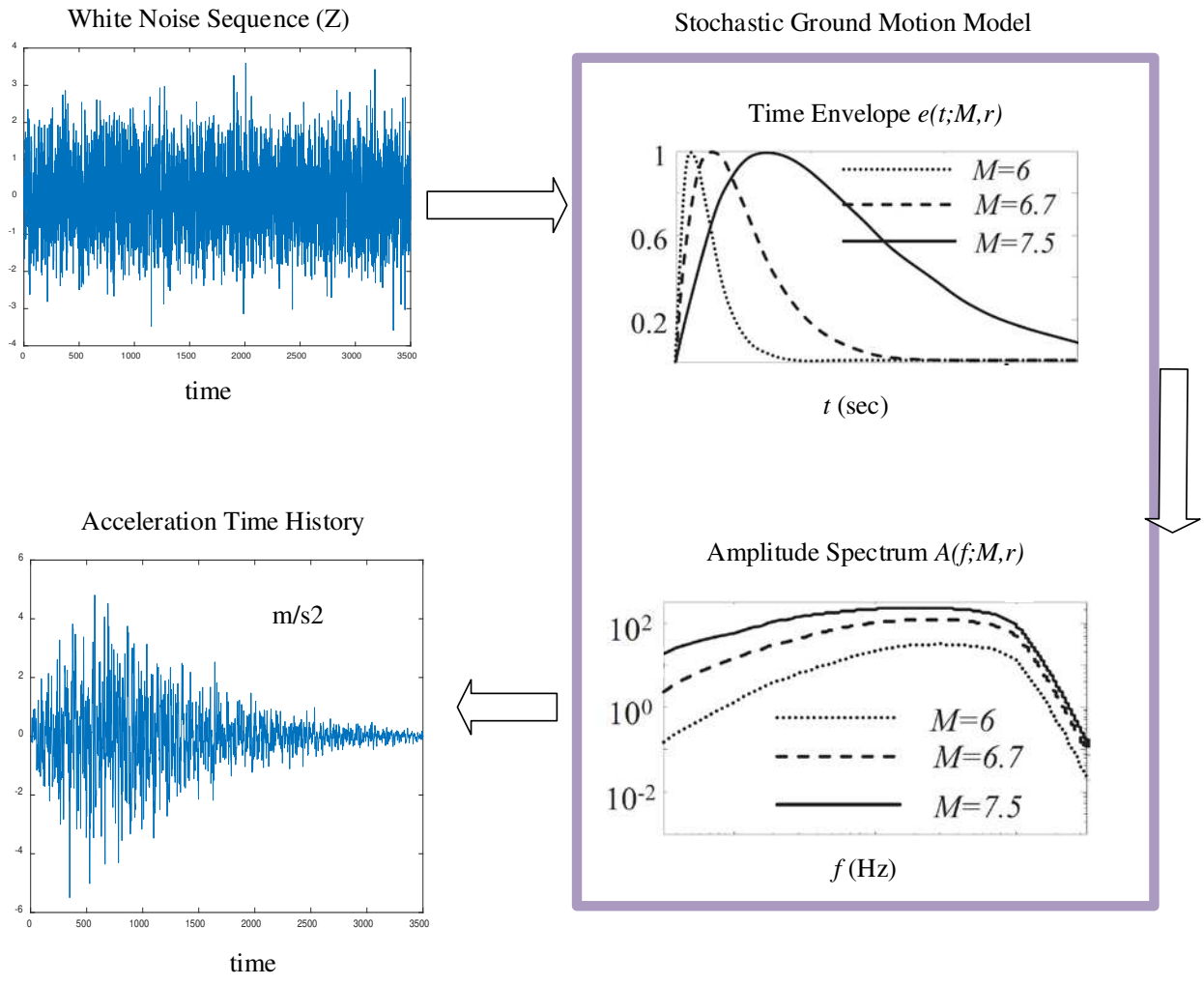

Figure 40 Generation of ground motion using stochastic ground motion model

APPENDIX B: ACCEPT-REJECT ALGORITHM

To generate samples from a target density $\pi(\boldsymbol{\theta})$, the general accept-reject algorithm can be used. It can even be applied to cases when we only know the target density up to some normalization constant. The accept-reject algorithm works as follows. First, choose an appropriate proposal density $q(\boldsymbol{\theta})$ and then follow the following steps.

1. Randomly simulate candidate sample $\boldsymbol{\theta}_c$ from the selected proposal density $q(\boldsymbol{\theta})$ and also simulate uniform random number u from $U(0,1)$.
2. Accept $\{\boldsymbol{\theta}\}_k = \boldsymbol{\theta}_c$ (where $\{\boldsymbol{\theta}_k\}$ is the k^{th} sample) if

$$\frac{\pi(\boldsymbol{\theta}_c)}{M_r \cdot q(\boldsymbol{\theta}_c)} > u \tag{B.1}$$

$$\text{where } M_r > \max_{\Theta}\left[\frac{\pi(\boldsymbol{\theta})}{q(\boldsymbol{\theta})}\right] \tag{B.2}$$

3. Return to 1. Otherwise

Note that $\forall \boldsymbol{\theta} : M_r \cdot q(\boldsymbol{\theta}) \geq \pi(\boldsymbol{\theta})$. The efficiency of this method is defined as the number of trials needed (on the average) to simulate one sample from $\pi(\boldsymbol{\theta})$. On the average, for simulating one sample, the number of trials needed is:

$$\frac{\int_{\Theta} M_r \cdot q(\boldsymbol{\theta}) d\boldsymbol{\theta}}{\int_{\Theta} \pi(\boldsymbol{\theta}) d\boldsymbol{\theta}} = M_r \frac{\int_{\Theta} q(\boldsymbol{\theta}) d\boldsymbol{\theta}}{\int_{\Theta} \pi(\boldsymbol{\theta}) d\boldsymbol{\theta}} \tag{B.3}$$

If both $\pi(\boldsymbol{\theta})$ and $q(\boldsymbol{\theta})$ are normalized densities then this simplifies to:

$$M_r \frac{\int_{\Theta} q(\boldsymbol{\theta}) d\boldsymbol{\theta}}{\int_{\Theta} \pi(\boldsymbol{\theta}) d\boldsymbol{\theta}} = M_r \frac{1}{1} = M_r \tag{B.4}$$

The computational efficiency of the algorithm is generally defined as the quotient of the number of samples/number of trails. Thus smaller values of M_r lead to better sampling efficiency. Since M_r is given by (B.2), this shows that the efficiency depends on selection of the proposal PDF $q(\boldsymbol{\theta})$ and of the scalar M_r . $q(\boldsymbol{\theta})$ should be chosen so that (a) it is easy to sample from (since we need to simulate samples from this density) and (b) it is close to the target density. It is also important to choose M_r so that (c) it is actually close to $\max_{\Theta}\left[\pi(\boldsymbol{\theta})/q(\boldsymbol{\theta})\right]$. Also, an implicit constraint is that the $\sup \pi(\boldsymbol{\theta}) \subset \sup q(\boldsymbol{\theta})$ and that the ratio $\pi(\boldsymbol{\theta})/q(\boldsymbol{\theta})$ remains bounded.